Vibronic effects in the transport characteristics of STM single molecule junctions

Master Thesis

University of Regensburg
Institute of Theoretical Physics
Supervisor PD Dr. Andrea Donarini

Raphael Kozlovsky

May 2015

Abstract

In this thesis, we present a minimal model that describes the effect of a vibrational degree of freedom in the molecule on the transport characteristics of scanning-tunneling microscopy (STM) single-molecule junctions. We consider an STM setup with molecules on ultrathin insulating films, which enables the analysis of unperturbed molecular orbitals of individual molecules [1]. The entire system can be treated as an effective double barrier junction, hence we use the Liouville equation approach to compute its transport properties. Recent spatially resolved vibronic spectroscopy experiments have shown that the number of excited vibrons in a single tunneling event strongly depends on the local symmetry of the molecular wave function [2]. This is in contrast to the Franck-Condon picture [3–5], where the magnitude of vibrational excitations crucially depends on the change of the equilibrium position of the nuclei (which is determined by the global wave function) upon electron attachment. Furthermore, a vibron-assisted tunneling effect has been observed, which facilitates electron transfer between tip and molecule although the tunneling amplitude without the vibrational degree of freedom is vanishing. We develop a theory that confirms these findings and yields selection rules for certain high symmetry configurations. The crucial component of this theory are tunneling amplitudes that depend on the vibronic state and enable vibronic excitations also in absence of any electron-vibron coupling for the isolated molecule. The results for our model show that vibron-assisted tunneling is only possible if the excited modes move the nodal planes of the molecular orbital. Moreover, they suggest that either a mode with a large zero-point fluctuation (comparable to the atomic bond length) or a huge number of highly excited states is needed to bring the present vibron-assisted tunneling effect to a sizable scale.

Contents

1 Introduction

In 1986, G. Binnig and H. Rohrer earned the Nobel Prize in Physics for their invention of the scanning tunneling microscope [6]. To this day, STM has a significant impact especially on atomic-scale and surface science. The reason for this is that it provides manifold and powerful possibilities to study matter on and below the nanometre scale. For example, it is possible to arrange single atoms [7], use STM for spectroscopy [8], or probe almost unperturbed individual molecular orbitals [1].

It was not until 1990, that the atomic resolution of the STM could be explained satisfactory on a theoretical level [9]. This was done by C. J. Chen, who derived his famous "derivative rule" [10], which enables the calculation of the tunneling matrix element between tip and sample in a convenient way.

Although the invention of the STM was over 30 years ago, there are still many challenges which can be addressed, both theoretically and experimentally. This leads us to the topic of this thesis, which is to study theoretically the effect of a vibrational degree of freedom in the probed molecule, on the transport characteristics of the STM.

We restrict ourselves to STM setups with molecules on thin insulating films [1, 11, 12]. Such an insulating film consists of a few atomic layers, which is grown on a metal substrate, and allows to reduce strongly the hybridization between the overlaying molecule and the metallic substrate. Hence, intrinsic molecular properties can be better investigated. Since this technique leads to an additional potential barrier between molecule and substrate,

the entire system can be treated as an effective double-barrier junction. The molecule behaves as an open quantum system which is in contact to macroscopic reservoirs. Thus, the reduced density matrix approach [13–15], which is utilized in this thesis, is suitable to compute the quantum transport through the molecule.

1.1 Motivation

The topic of this thesis has been motivated by experiments that use STM with molecules on thin insulating films for spatially resolved vibronic spectroscopy [2]. These experiments show a novel effect which goes beyond the simple Franck-Condon picture and can be called vibron-assisted tunneling. In particular, the relation between the symmetry of the tip and the local symmetry of the molecular wave function affects the number of excited vibrons during a single tunneling event. This can be an important input for organic or molecular electronics, where the excitation of vibrons should be minimized due to dissipation.

As far as we know, there is no satisfying theory explaining this effect. The aim of this thesis is to find the origin of vibron-assisted tunneling. Moreover, we want to develop a model which describes in general the effect of a vibrational degree of freedom in the probed molecule on the transport characteristics of STM.

1.2 Outline

This thesis is organized as follows. Chapter 2 gives a short introduction on STM and presents the experimental technique that allows to study almost unperturbed molecules. Moreover, the spatially resolved vibronic spectroscopy measurements that motivated this thesis are presented.

Chapter 3 starts with the introduction of the model Hamiltonian we use to describe the entire system. The molecular part of this Hamiltonian is diagonalized exactly and vibronic mode dependent tunneling matrix elements, which are crucial for our theory, are introduced. Subsequently, we derive rate equations which allow to compute the transport through the system within the Liouville equation approach. The vibronic mode dependent tunneling matrix elements influence the transport characteristics via the rate between the tip and the molecule, which is discussed in great detail. In the end, a model with a simplified electronic and vibronic structure, but extended by a relaxation rate, is introduced.

Chapter 4 is dedicated to the results we obtained with a numerical implementation of our model within the Liouville equation approach. We show spatially resolved vibronic

spectroscopy data of the full model, which reveal inter alia vibron-assisted tunneling for a mode which moves the nodal plane of the molecule.

Chapter 5 deals with the numerical implementation of the model which is extended by a relaxation rate. Within this model, a strong enhancement of the vibron-assisted tunneling effect is observed for certain relaxation rates. Moreover, we study the influence of the parameters which determine the form of the orbital wave function, on the vibron-assisted tunneling effect.

2

Spatially Resolved Vibronic Spectroscopy with an STM

In the beginning of this chapter, a brief introduction concerning STM is given. Moreover, an extended STM setup with an additional thin insulating layer between sample and substrate is described (Sec. 2.1). After that, a theory which explains the atomic resolution in STM and gives the tunneling matrix elements between tip and sample is introduced (Sec. 2.2). In the last section of this chapter, an experiment which shows spatially resolved vibronic spectroscopy data is presented (Sec. 2.3).

2.1 STM with molecules on thin insulating films

An STM setup with an additional thin insulating layer is depicted in Fig. 2.1. The usual scanning-tunneling microscope consists of a tip, a substrate and a sample which is adsorbed on the substrate. In this thesis, we are interested in probing molecules.

By applying a bias voltage V_b between substrate and tip, the chemical potentials of the leads μ_{tip} and μ_{sub} change and it is possible to get into resonance with one of the molecular orbitals (e.g. the LUMO in Fig. 2.1). Consequently, current starts to flow through the sample via quantum mechanical tunneling through the vacuum barrier and can be measured as a function of the tip position. Note, that the bias drop is highly

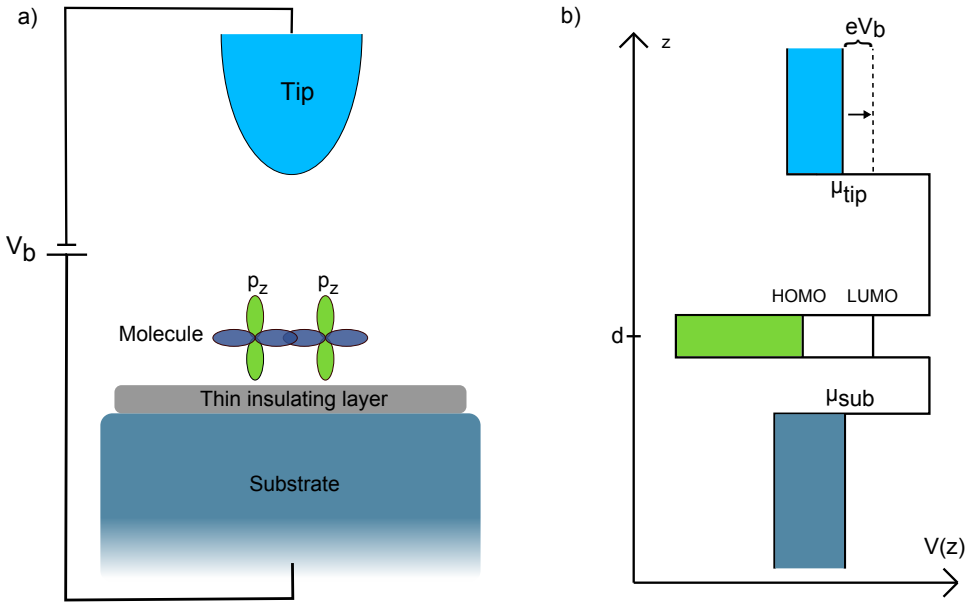

Figure 2.1: a) shows an STM setup with a thin insulation film between the molecule and the substrate. b) depicts the potential landscape of the scanning-tunneling microscope given in (a). The potential well at $z = d$ represents the molecule with its highest occupied molecular orbital (HOMO) and lowest unoccupied molecular orbital (LUMO).

asymmetric. It occurs mainly between tip and molecule, which is indicated by a shift of μ_{tip} about eV_b. If the distance between tip and sample is kept constant ($z_{\text{tip}} = \text{const.}$) and the tip is moved laterally (in the xy-plane) above the sample, one speaks of *constant height imaging*. If the tunneling current is kept constant by adjusting the tip-sample distance, the terminology is *constant current imaging*. Both methods allow to draw conclusions about the spatial form of the molecular orbitals. By measuring the current as a function of the bias voltage for a fixed tip position, it is possible to do spectroscopy. Combining both methods, i.e. measuring the current for different tip positions as a function of the bias, yields spatially resolved spectroscopy. This is discussed in Sec. 2.3.

The additional thin insulating film, depicted in Fig. 2.1, consists only of a few atomic layers and is grown directly onto the substrate. Typical materials are sodium chloride or xenon. With the insulating layer, the hybridization between substrate and molecule is strongly reduced. Thus, it is possible to study inherent electronic and vibrational properties of the latter. The first experiments showing the success of this technique were published in 2005 by J.Repp et al. [1].

2.2 Chen's derivative rule

In 1990, C. J. Chen published a theory which is based on Bardeen's tunneling formalism [16] and explains the atomic resolution of STM [9]. Soon after that he published his famous "derivative rule" [10], which allows to calculate the tunneling matrix element between tip and molecule for a given tip symmetry. For simplicity, we restrict ourselves to a tip wave function which has s-symmetry, which is a good approximation for metal tips [17]. We emphasize that the generalization to higher angular momentum symmetries is straightforward.

According to [9], the tunneling matrix element between an s-symmetric tip and a molecule is given by

$$t_{\mathbf{k},i}^{\mathrm{tip}} = \frac{2\pi\hbar^2 C_s}{m_e \kappa} \Psi_i(\mathbf{r}_{\mathrm{tip}}). \tag{2.1}$$

Here, i labels the molecular orbitals, m_e the electron mass, and C_s a dimensionless mixing coefficient which is important if various tip-symmetries are taken into account. The decay constant is given by $\kappa = \sqrt{\frac{2m_e}{\hbar^2}(\epsilon_F^{\mathrm{tip}} + \Phi_0^{\mathrm{tip}} - \epsilon_{\mathbf{k}})}$, where $\epsilon_F^{\mathrm{tip}}$ is the Fermi energy and Φ_0^{tip} the work function of the tip, respectively.

Chen's derivative rule can also be expressed in a more descriptive way. If the symmetry of the tip and the local symmetry of the molecular wave function at the position of the tip match, tunneling is allowed, otherwise it is forbidden. Examples for local symmetries of the LUMO of a pentacene molecule are depicted in Fig. 2.2.

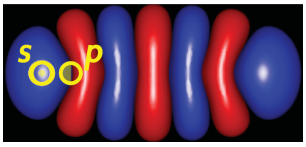

Figure 2.2: Image taken from [2]. It shows the LUMO of pentacene, calculated with density functional theory. Exemplary points with local s- and p-symmetries are marked.

2.3 Symmetry dependence of vibron-assisted tunneling

In this section, the experiments [2] that motivated this thesis are presented. They show that the local symmetry of the molecular wave function at the position of the tip determines the amount of vibronic excitations in the molecule upon electron attachment. This fact goes beyond the Franck-Condon picture, which does not account for the local symmetry of the electronic wave function. There, all that matters is the changed equilibrium position of the nuclei after charging the molecule, which can lead to a relaxation process and thus to vibronic excitations.

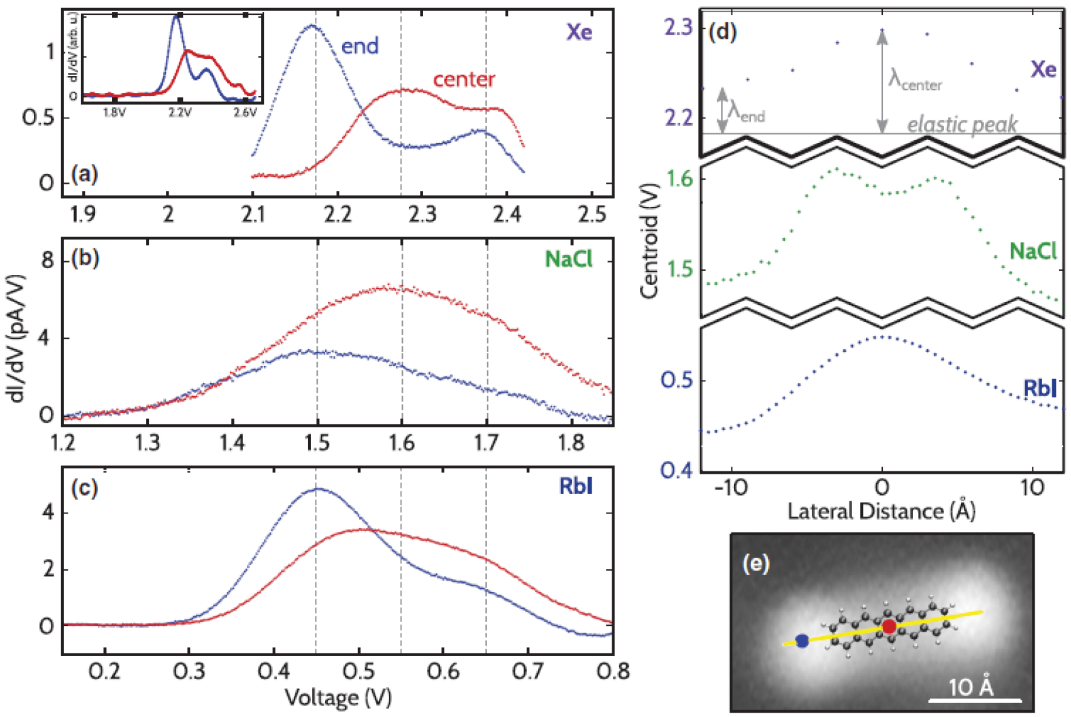

Figure 2.3: Figure taken from [2]. In (a,b,c), dI/dV-curves for tip positions indicated in (e) are shown for different insulating layers. The grey dashed lines point out the position of the elastic and the first two vibronic peaks. (d) shows the centroids of the dI/dV-curves along the long axis of pentacene. This axis is indicated in (e) via the yellow line.

The setup for these experiments is as given in Fig. 2.1 and the adsorbed molecule is pentacene. Three different insulating layers where considered, namely Xe, RbI and NaCl. Figs. 2.3(a,b,c) show the differential conductance dI/dV as a function of the bias voltage V at tip positions indicated in Fig. 2.3(e) for an s-symmetric tip wave function. The bias range chosen here excludes other electronic excitations then the LUMO.

Above the end of pentacene, the LUMO is locally s-symmetric (Fig. 2.2). Therefore, the symmetry with respect to the tip matches, and elastic tunneling is allowed according to Chen's derivative rule.

Above the center, the LUMO has a large nodal plane density, i.e. also p-symmetry. Thus, the symmetries match only partially if the tip is positioned in the central region. According to Chen's derivative rule, elastic tunneling should be reduced, which can be seen in Fig. 2.3(a). There, the elastic contribution, which corresponds to the peak that is lowest in bias, is drastically suppressed. However, there is a strong peak found at larger bias, which can be assigned to an excitation of a vibron.

Summarizing the results in [2], one can say that even though tunneling should be forbidden for tip positions where symmetries do not match, it is allowed but only for large enough bias. The extra amount of energy is used to excite a vibron. Therefore, one can speak of *vibron-assisted tunneling*.

Fig. 2.3(d) shows the centroid of the $\mathrm{d}I/\mathrm{d}V$-curves for different positions of the tip. The centroid is the center of mass of the area under the curve. Due to vibron-assisted tunneling the centroid at the center of the molecule is at larger bias than at the end.

3

Theoretical Methodology and Analytics

This chapter is about the theoretical description of STM with molecules on thin insulating films and a vibrational degree of freedom in the molecule. In the first section, the model Hamiltonian which describes the entire system is introduced (Sec. 3.1). After that, the derivation of the master equation for the populations of the reduced density matrix is presented (Sec. 3.2). Crucial for the transport characteristics are the rates appearing in this master equation. They will be discussed in detail in Sec. 3.3. Finally, a simplified model is introduced in which the molecule is described by only one spinless electronic state and one vibronic mode. This model is extended by a relaxation rate.

3.1 Model Hamiltonian

Our model Hamiltonian, which represents the double barrier junction shown in Fig. 2.1, can be split into five parts

$$\hat{H} = \hat{H}_{\mathrm{mol}} + \hat{H}_{\mathrm{tip}} + \hat{H}_{\mathrm{sub}} + \hat{H}_{\mathrm{mol-tip}} + \hat{H}_{\mathrm{mol-sub}}. \tag{3.1}$$

The molecule is represented by the Hamiltonian $\hat{H}_{\mathrm{mol}}$ which is described in detail in Sec. 3.1.1. $\hat{H}_{\mathrm{tip}}$ and $\hat{H}_{\mathrm{sub}}$ are the Hamiltonians for the tip and the substrate, which we assume

to be reservoirs of noninteracting electrons. Hence, we have

$$\hat{H}_\eta = \sum_{\mathbf{k}\sigma} \epsilon_{\mathbf{k}} \hat{c}^\dagger_{\eta\mathbf{k}\sigma} \hat{c}_{\eta\mathbf{k}\sigma}, \tag{3.2}$$

where $\mathbf{k} \equiv \vec{k}$, η = tip/sub and $\hat{c}_{\eta\mathbf{k}\sigma}$ is the annihilation operator for an electron with momentum $\mathbf{k}$ and spin projection σ in lead η. $\hat{H}_{\mathrm{mol-tip}}$ and $\hat{H}_{\mathrm{mol-sub}}$ describe the transfer of electrons between the molecule and the leads and are described in Sec. 3.1.2.

3.1.1 Minimal model for the molecule

The hypothetical molecule we consider has two p_z-orbitals at $z = d$ with a distance a between them (see Fig. 2.1). Only these two orbitals contribute to electron transport through the molecule, since we assume that they are the only part of the molecule which has a finite overlap to the leads. Moreover, our model molecule is in its neutral state if both p_z-orbitals carry in total two electrons. A real molecule one could think of is for example ethylene, but instead of treating all the vibrational modes, we consider only two of them. We emphasize, that we are not interested in simulating quantitatively the transport through a real molecule, but we want to study qualitatively the effects of a vibrational degree of freedom in the probed molecule on the transport properties of STM, using the reduced density matrix formalism. Note that it is realistic to assume that such a molecule can be stable even though the p_z-orbitals are fully occupied or empty by presuming additional orbitals which do not contribute to transport but stabilize the molecule. In Fig. 2.1 this is indicated by additional p-orbitals that form a σ-bond.

Electronic part

In our model, the purely electronic part of $\hat{H}_{\mathrm{mol}}$ is given by

$$\hat{H}^{\mathrm{el}}_{\mathrm{mol}} = \sum_\sigma \left[\epsilon_e(\hat{n}_{e\sigma} - 1) + \epsilon_o \hat{n}_{o\sigma}\right] + \frac{U}{2}(\hat{N} - 2)^2. \tag{3.3}$$

The subscript e/o denotes an even/odd orbital, σ is the spin degree of freedom, and $\hat{n}_{e/o\,\sigma}$ is the particle number operator given by $\hat{d}^\dagger_{e/o\,\sigma}\hat{d}_{e/o\,\sigma}$. $\hat{d}_{e/o\,\sigma}$ are the corresponding annihilation operators. The even/odd orbitals have onsite energies $\epsilon_{e/o}$ and they form the basis in which $\hat{H}^{\mathrm{el}}_{\mathrm{mol}}$ is diagonal. They can be defined via

$$\hat{d}_{e/o\,\sigma} = \frac{1}{\sqrt{2}}\left(\hat{d}_{\mathrm{L}\sigma} \pm \hat{d}_{\mathrm{R}\sigma}\right), \tag{3.4}$$

where the subscript L/R denotes the left and the right p_z orbital, respectively. Electron-electron interaction is included via the constant interaction term $\frac{U}{2}(\hat{N}-2)^2$, where $\hat{N}$ is the total particle number operator $\sum_\sigma \left(\hat{d}^\dagger_{e\sigma}\hat{d}_{e\sigma} + \hat{d}^\dagger_{o\sigma}\hat{d}_{o\sigma}\right)$. U is a constant which quantifies the strength of the Coulomb interaction between the electrons.
Note that the neutral molecule in its ground state, which is defined via $\sum_\sigma n_{e\sigma} = 2$ and $\sum_\sigma n_{o\sigma} = 0$, has zero electronic energy and the parameters ϵ_e, ϵ_o and U should be chosen such that the energy with respect to the neutral state increases if an electron is added or subtracted.

Vibronic part

We assume, that the vibrational dynamics of our molecule is determined by Hooke's law (harmonic approximation) and the configuration of the springs with stiffness k_1 and k_2 is as given in Fig. 3.1. We choose that particular configuration because it yields two qualitatively different modes, one that does move and one that does not move the nodal plane of the odd molecular orbital. Thus, it is possible to analyse which of the two modes triggers the vibron-assisted tunnelling effect (Sec. 2.3).

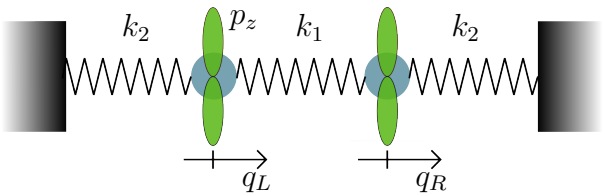

Figure 3.1: Two masses modelling the nuclei of the molecule connected to each other and to the environment by a linear force.

The magnitude of the spring constant k_1 is determined by the chemical-bond (in Fig. 2.1 the σ-bond) between the two atoms, whereas k_2, for example, could stem from the van der Waals forces between the molecule and the thin insulation layer. Another possibility is that k_2 simulates the local dynamics of a larger molecule.

Newtons second law allows us to construct the equations of motion for q_L and q_R, which are the displacement coordinates around the equilibrium positions of the left and the right atom. In matrix form, we have

$$\begin{pmatrix} \ddot{q}_L \\ \ddot{q}_R \end{pmatrix} = \frac{1}{m} \begin{pmatrix} -k_2 - k_1 & k_1 \\ k_1 & -k_2 - k_1 \end{pmatrix} \begin{pmatrix} q_L \\ q_R \end{pmatrix}, \tag{3.5}$$

where m denotes the mass of the left and the right nucleus, respectively. This system of

equations can be solved by the Ansatz

$$\begin{aligned} q_L(t) &= Ae^{i\omega t} + Be^{-i\omega t} \\ q_R(t) &= Ce^{i\omega t} + De^{-i\omega t}, \end{aligned} \tag{3.6}$$

which leads to the simple problem of finding the kernel of a 2 by 2 matrix

$$\begin{pmatrix} k_1 + k_2 - m\omega^2 & -k_1 \\ -k_1 & k_1 + k_2 - m\omega^2 \end{pmatrix} \begin{pmatrix} q_L \\ q_R \end{pmatrix} = 0. \tag{3.7}$$

By solving the equation

$$\begin{vmatrix} k_1 + k_2 - m\omega^2 & -k_1 \\ -k_1 & k_1 + k_2 - m\omega^2 \end{vmatrix} = (k_1 + k_2 - m\omega^2)^2 - k_1^2 = 0 \tag{3.8}$$

we get the frequencies ω for which Eq. 3.5 has solutions. They are given by $\omega_1 = \sqrt{k_2/m}$ and $\omega_2 = \sqrt{(2k_1 + k_2)/m}$. We denote $\omega_S \equiv \omega_1$ and $\omega_D \equiv \omega_2$. The associated eigenvectors (i.e. the vibrational eigenmodes) are

$$\vec{v}_S = \frac{1}{\sqrt{2}} \begin{pmatrix} 1 \\ 1 \end{pmatrix} \quad \text{and} \quad \vec{v}_D = \frac{1}{\sqrt{2}} \begin{pmatrix} 1 \\ -1 \end{pmatrix}. \tag{3.9}$$

The mode determined by $\vec{v}_S$ describes a motion where both atoms oscillate in phase and the nodal plane of the odd molecular orbital moves. Instead, the mode $\vec{v}_D$ describes a motion with a phase shift of π between the two atoms and the nodal plane does not move. A general solution of the dynamics of the system can be written as

$$\begin{pmatrix} q_L(t) \\ q_R(t) \end{pmatrix} = A_S \cos(\omega_S t + \delta_S) \frac{1}{\sqrt{2}} \begin{pmatrix} 1 \\ 1 \end{pmatrix} + A_D \cos(\omega_D t + \delta_S) \frac{1}{\sqrt{2}} \begin{pmatrix} 1 \\ -1 \end{pmatrix} \tag{3.10}$$

where A_S, A_D and δ_S, δ_D are fixed by the initial conditions. This equation motivates to define the normal mode coordinates as

$$Q_k \equiv A_k \cos(\omega_k t + \delta_k), \quad k = S, D, \tag{3.11}$$

which allows us to write Eq. 3.10 as

$$\mathbf{q} = \sum_{k=S,D} Q_k \mathbf{v}_k, \tag{3.12}$$

where $\mathbf{q} \equiv \begin{pmatrix} q_L(t) & q_R(t) \end{pmatrix}^T$. Note that $Q_S = \frac{1}{\sqrt{2}}(q_L(t)+q_R(t))$ and $Q_D = \frac{1}{\sqrt{2}}(q_L(t)-q_R(t))$, which is why we denoted the modes via S for "sum" and D for "difference". The $\{Q_k\}$ satisfy the harmonic oscillator equation of motion. Hence, we can quantize them in terms of bosonic creation and annihilation operators $\hat{a}^\dagger$ and $\hat{a}$, which gives

$$\hat{Q}_k = \Delta x_{0k} \left(\hat{a}_k^\dagger + \hat{a}_k \right). \tag{3.13}$$

The zero-point fluctuations Δx_{0k} are given by $\Delta x_{0D} = \sqrt{\hbar/m\omega_D}$ and $\Delta x_{0S} = \sqrt{\hbar/4m\omega_S}$, which is derived in A.1.

Now, we concentrate on the coupling between the electronic and the vibrational degrees of freedom. We choose a similar derivation as given by [18] and [19]. The adiabatic approximation of M. Born and R. Oppenheimer [20], in which the molecular Hamiltonian depends parametrically on the displacement coordinates, plays a key role. This approximation is justified because the electrons move on a much shorter time scale then the nuclei due to their huge mass difference. Therefore, we can write

$$\hat{H}_{\text{mol}} = \sum_\sigma \left[\epsilon_e(q_L, q_R)(\hat{n}_{e\sigma} - 1) + \epsilon_o(q_L, q_R)\hat{n}_{o\sigma}\right] + \frac{U}{2}(\hat{N}-2)^2 + \sum_{k=S,D} \hbar\omega_k(\hat{a}_k^\dagger \hat{a}_k + \frac{1}{2}), \tag{3.14}$$

where the energies of the orbitals are functions of the displacement coordinates and the harmonic motion of the nuclei gives the additional harmonic oscillator energy. For small displacements, we can expand $\epsilon_{e/o}(q_L, q_R)$ up to the first order in the displacement coordinates around the equilibrium position, which yields

$$\epsilon_{e/o}(q_L, q_R) \approx \epsilon_{e/o}(0,0) + \sum_{i=L,R} \left.\frac{\partial \epsilon_{e/o}(q_L, q_R)}{\partial q_i}\right|_{\mathbf{q}=0} q_i. \tag{3.15}$$

Next, we use Eq. 3.12 and take the quantum limit (Eq. 3.13), which results in

$$\epsilon_{e/o}(q_L, q_R) \approx \epsilon_{e/o} + \sum_{i=L,R} \left.\frac{\partial \epsilon_{e/o}(q_L, q_R)}{\partial q_i}\right|_{\mathbf{q}=0} \sum_{k=S,D} \Delta x_{0k} \left(\hat{a}_k^\dagger + \hat{a}_k \right) (\mathbf{v}_k)_i, \tag{3.16}$$

where we denoted $\epsilon_{e/o} \equiv \epsilon_{e/o}(0,0)$ and $(\mathbf{v}_k)_i$ is the i-th component of the vector $\mathbf{v}_k$. Eq. 3.16 motivates to define the electron-vibron coupling constant g_{jk} as

$$g_{jk} \equiv \sum_{i=L,R} \left.\frac{\partial \epsilon_j(q_L, q_R)}{\partial q_i}\right|_{\mathbf{q}=0} \Delta x_{0k} (\mathbf{v}_k)_i \tag{3.17}$$

where $j = \{e, o\}$ and $k = \{S, D\}$. First, we notice that there is no electron-vibron

coupling to the S-mode, since the motion of the two nuclei are in phase, which means that the distance between them remains unchanged. Therefore, there cannot be any change in the energies of the orbitals if this mode is excited. Or expressed in a mathematical way,

$$g_{jS} = \Delta x_{0S} \left(\left. \frac{\partial \epsilon_j(q_L, q_R)}{\partial q_L} \right|_{\mathbf{q}=0} + \left. \frac{\partial \epsilon_j(q_L, q_R)}{\partial q_R} \right|_{\mathbf{q}=0} \right) = 0 \tag{3.18}$$

since

$$\left. \frac{\partial \epsilon_j(q_L, q_R)}{\partial q_L} \right|_{\mathbf{q}=0} = - \left. \frac{\partial \epsilon_j(q_L, q_R)}{\partial q_R} \right|_{\mathbf{q}=0} . \tag{3.19}$$

Therefore, we denote $g_j \equiv g_{jD}$ and write the molecular Hamiltonian in its final form:

$$\begin{aligned} \hat{H}_{\text{mol}} = & \sum_{\sigma} \left[\epsilon_e(\hat{n}_{e\sigma} - 1) + \epsilon_o \hat{n}_{o\sigma} + g_e(\hat{a}_D^\dagger + \hat{a}_D)(\hat{n}_{e\sigma} - 1) + g_o(\hat{a}_D^\dagger + \hat{a}_D)\hat{n}_{o\sigma} \right] \\ & + \frac{U}{2}(\hat{N} - 2)^2 + \sum_{k=S,D} \hbar\omega_k (\hat{a}_k^\dagger \hat{a}_k + \frac{1}{2}). \end{aligned} \tag{3.20}$$

Note that this Hamiltonian allows a rather intuitive interpretation. As soon as the electronic configuration is changed, the electron-vibron coupling leads to a new equilibrium distance between the nuclei. This is exactly what one would expect in the Franck-Condon picture. In the following pages, we will derive the new equilibrium distance quantitatively.

Diagonalization of the molecular Hamiltonian

In order to get the spectrum of the molecule with its vibrational degrees of freedom we need to diagonalize $\hat{H}_{\text{mol}}$. This can be done using the so-called Lang Firsov (or sometimes Polaron) transformation [21, 22], which is a unitary transformation of the form

$$\tilde{\hat{H}}_{\text{mol}} = e^{\hat{S}} \hat{H}_{\text{mol}} e^{-\hat{S}}. \tag{3.21}$$

For our specific Hamiltonian the appropriate $\hat{S}$ operator reads

$$\hat{S} = \frac{1}{\hbar\omega_D} \sum_{\sigma} \left[g_e(\hat{n}_{e\sigma} - 1) + g_o \hat{n}_{o\sigma} \right] (\hat{a}_D^\dagger - \hat{a}_D) \, . \tag{3.22}$$

For convenience, the hats which indicate operators are omitted for the rest of this this section. Note that S is proportional to the vibronic momentum operator of the D-mode, which is the generator of spatial translations in the corresponding vibronic space. Hence, e^{-S} is an operator which shifts the D-mode states.

To perform the transformation, we use the Hadamard-Lemma (also called Lie formula),

which is the operator identity

$$e^{S}Ae^{-S} = \sum_{m=0}^{\infty} \frac{1}{m!}[S,A]_m \,, \tag{3.23}$$

where $[S,A]_m = [S,[S,A]_{m-1}]$, $[S,A]_0 = A$ and $[S,A]_1 = SA - AS$. For simplicity, each operator is transformed separately. We start with $d_{e\sigma}$ and compute the required commutator, obtaining

$$[S, d_{e\sigma}] = -\frac{g_e}{\hbar\omega_D}(a_D^\dagger - a_D)d_{e\sigma} \tag{3.24}$$

with the help of the relations

$$[n_{e\sigma'}, d_{e\sigma}] = -\{d_{e\sigma'}^\dagger, d_{e\sigma}\}d_{e\sigma} = -\delta_{\sigma\sigma'}d_{e\sigma} \quad \text{and} \quad [n_{o\sigma'}, d_{e\sigma}] = 0. \tag{3.25}$$

In Eq. 3.25, we have used the relation between commutator and anticommutator $[AB, D] = A\{B, C\} - \{A, C\}B$ and the canonical anticommutation relations $\{d_{e\sigma}, d_{e\sigma'}^\dagger\} = \delta_{\sigma\sigma'}$. Using Eqs. 3.23 and 3.24, we get

$$\begin{aligned} \tilde{d}_{e\sigma} = e^{S}d_{e\sigma}e^{-S} &= d_{e\sigma} - \frac{g_e}{\hbar\omega_D}(a_D^\dagger - a_D)d_{e\sigma} + \frac{1}{2}\left[\frac{g_e}{\hbar\omega_D}(a_D^\dagger - a_D)\right]^2 d_{e\sigma} - ... \\ &= d_{e\sigma}\exp\left\{-\frac{g_e}{\hbar\omega_D}(a_D^\dagger - a_D)\right\}. \end{aligned} \tag{3.26}$$

Similarly, one obtains

$$\tilde{d}_{o\sigma} = d_{o\sigma}\exp\left\{-\frac{g_o}{\hbar\omega_D}(a_D^\dagger - a_D)\right\}. \tag{3.27}$$

A direct consequence of Eqs. 3.26 and 3.27 is that the operator $n_{i\sigma}$ is invariant under the polaron transformation, i.e.

$$\tilde{n}_{i\sigma} = \tilde{d}_{i\sigma}^\dagger\tilde{d}_{i\sigma} = n_{i\sigma} \;\text{ for }\; \mathrm{i} = \mathrm{e}, \mathrm{o}. \tag{3.28}$$

The vibronic operators transform as

$$\tilde{a}_D = a_D - \frac{1}{\hbar\omega_D}\sum_\sigma [g_e(n_{e\sigma} - 1) + g_o n_{o\sigma}] \quad \text{and} \quad \tilde{\mathrm{a}}_\mathrm{S} = \mathrm{a}_\mathrm{S}, \tag{3.29}$$

where we have used Eq. 3.23 and the canonical commutation relations of the ladder operators of the harmonic oscillator.

Inserting the transformed operators into Eq. 3.20, one gets the transformed molecular

Hamiltonian

$$\begin{aligned}\tilde{H}_{\mathrm{mol}} =& \sum_{\sigma}\left[\epsilon_e(n_{e\sigma}-1)+\epsilon_o n_{o\sigma}\right]-\frac{1}{\hbar\omega_D}\left[\sum_{\sigma} g_e(n_{e\sigma}-1)+g_o n_{o\sigma}\right]^2 \\ &+\frac{U}{2}(N-2)^2+\sum_{k=S,D}\hbar\omega_k(a_k^\dagger a_k+\frac{1}{2}).\end{aligned} \tag{3.30}$$

The absence of the electron-vibron coupling in $\tilde{H}_{\mathrm{mol}}$ implies that both its spectrum and eigenstates can be calculated in terms of independent electronic and vibronic degrees of freedom.

Spectrum and eigenstates of the molecular Hamiltonian

According to Eq. 3.30, the eigenstates of $\tilde{H}_{\mathrm{mol}}$ can be written in the occupation number representation as

$$\begin{aligned}&|n_{e\uparrow},n_{e\downarrow},n_{o_\uparrow},n_{o\downarrow};m_D,m_S\rangle \\ &=(d_{e\uparrow}^\dagger)^{n_{e\uparrow}}(d_{e\downarrow}^\dagger)^{n_{e\downarrow}}(d_{o\uparrow}^\dagger)^{n_{o\uparrow}}(d_{o\downarrow}^\dagger)^{n_{o\downarrow}}\frac{1}{\sqrt{m_D!}}(a_D^\dagger)^{m_D}\frac{1}{\sqrt{m_S!}}(a_S^\dagger)^{m_S}|0\rangle.\end{aligned} \tag{3.31}$$

The eigenstates of the original Hamiltonian H_{mol} are given by the polaron shifted states of $\tilde{H}_{\mathrm{mol}}$, i.e.

$$|\Psi_{n_{e\uparrow},n_{e\downarrow},n_{o_\uparrow},n_{o\downarrow};m_D,m_S}\rangle = e^{-S}|n_{e\uparrow},n_{e\downarrow},n_{o_\uparrow},n_{o\downarrow};m_D,m_S\rangle. \tag{3.32}$$

Since S consists basically of electronic particle number operators and the vibronic momentum operator of the D-mode, only the D-mode part of the states is shifted, the rest stays unchanged. The magnitude of the shift depends on the electronic configuration. This is consistent to the structure of H_{mol}, which contains a linear part and a parabolic part in the harmonic oscillator coordinate Q_D. These two parts combine to a shifted parabolic part with shifted harmonic oscillator eigenstates. The magnitude of the shift enters via the electronic operators in the linear part. The intuitive explanation is the following: The new equilibrium position between the nuclei due to a change in the electronic configuration leads to a shifted harmonic oscillator state.

The spectrum is easily obtained by using the relation

$$\tilde{H}_{\mathrm{mol}}|n_{e\uparrow},n_{e\downarrow},n_{o_\uparrow},n_{o\downarrow};m_D,m_S\rangle = E_{n_{e\uparrow},n_{e\downarrow},n_{o_\uparrow},n_{o\downarrow};m_D,m_S}|n_{e\uparrow},n_{e\downarrow},n_{o_\uparrow},n_{o\downarrow};m_D,m_S\rangle, \tag{3.33}$$

which yields

$$\begin{aligned} E_{n_{e\uparrow},n_{e\downarrow},n_{o\uparrow},n_{o\downarrow};m_D,m_S} =& \sum_\sigma \left[\epsilon_e(n_{e\sigma}-1)+\epsilon_o n_{o\sigma}\right] - \frac{1}{\hbar\omega_D}\left[\sum_\sigma g_e(n_{e\sigma}-1)+g_o n_{o\sigma}\right]^2 \\ &+ \frac{U}{2}\left[\sum_\sigma (n_{e\sigma}+n_{o\sigma})-2\right]^2 + \sum_{k=S,D}\hbar\omega_k(m_k+\frac{1}{2}) \end{aligned} \tag{3.34}$$

with $n_{e\sigma} \in \{0,1\}$, $n_{o\sigma} \in \{0,1\}$, and $m_k \in \mathbb{N}_0$.

3.1.2 Tunnelling Hamiltonian

The tunneling Hamiltonian describes the transfer of electrons between the leads and the molecule. In our model, it is given by

$$\hat{H}_\mathrm{T} = \sum_{\mathbf{k},i,\sigma}\left(t^{\mathrm{sub}}_{\mathbf{k},i}\hat{c}^\dagger_{\mathrm{sub}\,\mathbf{k}\sigma}\hat{d}_{i\sigma} + t^{\mathrm{tip}}_{\mathbf{k},i}(\hat{Q}_S,\hat{Q}_D)\hat{c}^\dagger_{\mathrm{tip}\,\mathbf{k}\sigma}\hat{d}_{i\sigma} + H.c.\right). \tag{3.35}$$

$t^{\mathrm{sub}}_{\mathbf{k},i}$ is the tunneling matrix element between the substrate and the molecule. From now on, the index $\mathbf{k}$ is omitted because we work in the flat band limit. The index i labels the even and the odd molecular orbital.

The crucial part in our theory is the tunneling matrix element between the tip and the molecule $t^{\mathrm{tip}}_i(\hat{Q}_D,\hat{Q}_S)$, which depends on the molecular vibration via the quantized normal mode coordinates $\hat{Q}_D$ and $\hat{Q}_S$. This can be explained using Chen's derivative rule (Sec. 2.2), which states that for an s-type tip the tunneling matrix element between tip and molecule is proportional to the molecular wavefunction evalutated at the position of the tip. The molecular wavefunction itself depends on the position of the atoms which can be written in terms of the normal mode coordinates of the vibrations. Therefore, for an s-symmetry tip, we have

$$t^{\mathrm{tip}}_{e/o}(\hat{Q}_D,\hat{Q}_S) = \frac{2\pi\hbar^2 C_S}{m\kappa}\Psi_{e/o}(\mathbf{r}_{\mathrm{tip}};\hat{Q}_D,\hat{Q}_S), \tag{3.36}$$

where $\Psi_{e/o}$ is the even and odd molecular wavefunction and $\mathbf{r}_{\mathrm{tip}}$ is the position of the tip appex. In the flat band limit, the prefactor in Eq. 3.36 is just a constant. This constant is not important for us, since the overall prefactor of the tunneling matrix element is just a free parameter of our theory. The molecular wavefunction is a linear combination of two p_z-orbitals (Sec. 3.1.1), i.e.

$$\Psi_{e/o}(\mathbf{r}_{\mathrm{tip}};Q_D,Q_S) = \frac{1}{\sqrt{2}}\left[p_z(\mathbf{r}_{\mathrm{tip}}-\mathbf{r}_1(Q_D,Q_S)) \pm p_z(\mathbf{r}_{\mathrm{tip}}-\mathbf{r}_2(Q_D,Q_S))\right]. \tag{3.37}$$

The positions of the atoms, which are aligned on the y-axis at $y = \mp\frac{a}{2}$ in equilibrium, is given by

$$\begin{aligned}\mathbf{r}_{1/2}(Q_D, Q_S) &= \left(0, \mp\frac{a}{2} + q_{L/R}, 0\right)^T \\ &= \left(0, \mp\frac{a}{2} + \frac{1}{\sqrt{2}}(Q_S \pm Q_D), 0\right)^T .\end{aligned} \tag{3.38}$$

Here, we have used that $q_{L/R} = \frac{1}{\sqrt{2}}(Q_S \pm Q_D)$ which is equivalent to Eq. 3.12. As usual, the p_z-orbital is given by

$$p(\mathbf{r}) = \frac{1}{4\sqrt{2\pi}} \left(\frac{Z_{\text{eff}}}{a_0}\right)^{\frac{5}{2}} z\, e^{-\frac{Z_{\text{eff}}|\mathbf{r}|}{2a_0}}, \tag{3.39}$$

where Z_{eff} is the effective atomic number and a_0 the Bohr radius.

We emphasize that the tunneling matrix element given by Eq. 3.36 enables transitions between different vibronic states even without any electron-vibron coupling. Moreover, we will see that it is the crucial ingredient for the explanation of vibron-assisted tunneling.

3.2 Quantum transport in the density matrix Formalism

The STM setup we consider corresponds to a double-barrier tunneling junction as described in Sec. 2.1 and 3.1, respectively. Therefore, the entire physical system can be divided into the molecule, the tip and the substrate. Since we assume that the molecule is weakly coupled to its leads, the reduced density matrix formalism, which is introduced in the next part of this thesis, is a good choice for the description of the electron transport through this system. In this formalism, the molecule is treated as an open quantum system and the reduced density matrix ρ_{red} describes its dynamics under the influence of the two leads.

3.2.1 The density operator

In quantum mechanics, a pure state of a system is by definition characterized by the eigenvalues of a largest set of mutually commuting independent observables. Since it is often not possible to assign a pure state to a quantum system, the concept of probability weight is introduced. For example, an electron in an unpolarized beam entering the famous Stern-Gerlach filtering apparatus [23, 24] cannot be characterized by a pure state,

but is said to be in a statistical mixture of states.

The average of the measurements of an observable $\hat{Q}$ is then generalized to

$$\begin{aligned}\langle\hat{Q}\rangle &\equiv \sum_i w_i \langle\Psi_i|\hat{Q}|\Psi_i\rangle \\ &= \sum_{i,j} w_i q_j |\langle q_j|\Psi_i\rangle|^2\end{aligned} \tag{3.40}$$

where $\{|q_j\rangle\}$ is a complete set of eigenstates of $\hat{Q}$ with eigenvalues q_j. The pure quantum mechanical probability for the state $|\Psi_i\rangle$ to be found in the eigenstate $|q_j\rangle$ enters via $|\langle q_j|\Psi_i\rangle|^2$, whereas the lack of knowledge appearing in a statistical mixture is attributed to the probabilities w_i. Notice that the $\{|\Psi_i\rangle\}$ need not to be orthogonal nor complete, but the set $\{w_i\}$ has to fulfill $\sum_i w_i = 1$. Eq. 3.40 can be rewritten into

$$\langle\hat{Q}\rangle = \sum_l \sum_k \left(\sum_i w_i \langle\alpha_l|\Psi_i\rangle\langle\Psi_i|\alpha_k\rangle \right) \langle\alpha_k|\hat{Q}|\alpha_l\rangle \tag{3.41}$$

where $\{|\alpha_k\rangle\}$ form an arbitrary orthonormal basis of the Hilbert space under consideration. Eq. 3.41 motivates to define the density operator $\hat{\rho}$ as

$$\hat{\rho} = \sum_i w_i |\Psi_i\rangle\langle\Psi_i| \tag{3.42}$$

with its matrix elements

$$\rho_{lk} = \sum_i w_i \langle\alpha_l|\Psi_i\rangle\langle\Psi_i|\alpha_k\rangle.$$

With that, the average of a measurement of an observable is simply given by

$$\langle\hat{Q}\rangle = \mathrm{Tr}(\hat{\rho}\hat{Q}). \tag{3.43}$$

The trace is evaluated using any orthonormal basis set and the density operator satisfies the normalization condition $\mathrm{Tr}\,\rho = 1$.

3.2.2 The time evolution of the density operator

The time evolution of a quantum mechanical state $|\Psi(t)\rangle$ is governed by the Schrödinger equation

$$i\hbar\frac{\partial}{\partial t}|\Psi(t)\rangle = \hat{H}(t)|\Psi(t)\rangle, \tag{3.44}$$

where $\hat{H}(t)$ is the (in general) time dependent Hamilton operator of the system. Starting from Eq. 3.44, one can directly deduce the time evolution of the density operator

$$\hat{\rho}(t) = \sum_i w_i |\Psi_i(t)\rangle\langle\Psi_i(t)|. \tag{3.45}$$

This leads to the equation of motion

$$i\hbar \frac{\partial}{\partial t}\hat{\rho}(t) = [\hat{H}(t), \hat{\rho}(t)], \tag{3.46}$$

which is called Liouville-von Neumann equation and is written in the Schrödinger picture.

For our system, which is composed of the tip, the molecule and the substrate, it is much too complicated to solve Eq. 3.46. Therefore, we split the total Hamiltonian $\hat{H}$ into three parts. The first part is the Hamiltonian of the molecule $\hat{H}_{\mathrm{mol}}$, the second part is the Hamiltonian of the reservoirs $\hat{H}_{\mathrm{res}}$, and the third part is the tunneling Hamiltonian $\hat{H}_{\mathrm{T}}$ which includes system-bath coupling. A detailed description of these Hamiltonians can be found in Sec. 3.1.

Because of the vacuum barrier between tip and molecule and the insulating layer between substrate and molecule, the total system can be seen as an effective double barrier junction. We assume that the coupling to the tip and the substrate is small enough to treat $\hat{H}_{\mathrm{T}}$ as a perturbation. With that in mind, we define the time evolution operator in the interaction picture as

$$\hat{U}^I(t, t_0) = e^{\frac{i}{\hbar}(\hat{H}_{\mathrm{res}}+\hat{H}_{\mathrm{mol}})(t-t_0)} e^{-\frac{i}{\hbar}\hat{H}(t-t_0)}, \tag{3.47}$$

where t_0 is some arbitrary reference time. We have assumed that the Hamiltonian is not explicitly time dependent. Now, we transform the Liouville-von Neumann equation into the interaction picture, where it takes the form

$$i\hbar \frac{\partial}{\partial t}\hat{\rho}^{\mathrm{I}}(t) = [\hat{H}^{\mathrm{I}}_{\mathrm{T}}(t), \hat{\rho}^{\mathrm{I}}(t)]. \tag{3.48}$$

The superscript I indicates that the operator is written in the interaction picture. Eq. 3.48 can be formally integrated, which yields

$$\hat{\rho}^{\mathrm{I}}(t) = \hat{\rho}^{\mathrm{I}}(t_0) - \frac{i}{\hbar}\int_{t_0}^{t} \mathrm{d}\tau \left[\hat{H}^{\mathrm{I}}_{\mathrm{T}}(\tau), \hat{\rho}^{\mathrm{I}}(\tau)\right]. \tag{3.49}$$

Reinserting Eq. 3.49 into Eq. 3.48 results in

$$\dot{\hat{\rho}}^{\mathrm{I}}(t) = -\frac{i}{\hbar}\left[\hat{H}_T^{\mathrm{I}}(t), \hat{\rho}^{\mathrm{I}}(t_0)\right] - \frac{1}{\hbar^2}\int_{t_0}^{t} \mathrm{d}\tau \left[\hat{H}_{\mathrm{T}}^{\mathrm{I}}(t), \left[\hat{H}_{\mathrm{T}}^{\mathrm{I}}(\tau), \hat{\rho}^{\mathrm{I}}(\tau)\right]\right], \tag{3.50}$$

which is a good starting point for a perturbative solution of the equation of motion for the density operator.

3.2.3 Generalized Master Equation

In this section, the derivation of the Generalized Master Equation for the reduced density operator is presented, following [25, 26].

In the scope of this thesis, we are interested in the transport through the molecule, for instance in the particle current

$$\langle I \rangle = \frac{\mathrm{d}}{\mathrm{d}t}\langle \hat{N}_{\mathrm{mol}} \rangle = \mathrm{Tr}\left(\dot{\hat{\rho}}(t)\hat{N}_{\mathrm{mol}}\right). \tag{3.51}$$

$\hat{N}_{\mathrm{mol}}$ is the particle number operator of the molecule, which only acts on states of the molecular Fock space. Therefore, it makes sense to split the trace into a molecular and a reservoir part, which leads to

$$\langle I \rangle = \mathrm{Tr}_{\mathrm{mol}}\left\{\mathrm{Tr}_{\mathrm{res}}\left(\dot{\hat{\rho}}\right)\hat{N}_{\mathrm{mol}}\right\}. \tag{3.52}$$

This motivates to define the reduced density operator as

$$\hat{\rho}_{\mathrm{red}} = \mathrm{Tr}_{\mathrm{res}}(\hat{\rho}). \tag{3.53}$$

As one can see from Eq. 3.52, it is enough to know $\hat{\rho}_{\mathrm{red}}$ in order to get the particle current into the molecule. Hence, the goal is to deduce an equation of motion for $\hat{\rho}_{\mathrm{red}}$, which can be done from Eq. 3.50. To this end, we rewrite the full density operator in a factorized and a non-factorized part:

$$\hat{\rho}^{\mathrm{I}}(t) = \hat{\rho}_{\mathrm{red}}^{\mathrm{I}}(t) \otimes \hat{\rho}_{\mathrm{res}} + \mathcal{O}(\hat{H}_{\mathrm{T}}). \tag{3.54}$$

This is possible if one assumes that the molecule and the reservoirs are uncorrelated at some time t_0 (the proof can be found in A.2). Note that $\hat{\rho}_{\mathrm{res}}$ is simply given by $\hat{\rho}_{\mathrm{res}} \equiv \hat{\rho}_{\mathrm{tip}} \otimes \hat{\rho}_{\mathrm{sub}}$. We assume that the tip and the substrate are huge reservoirs which are not effected by the rest of the system and which are in thermal equilibrium. Their

density operators are given by

$$\hat{\rho}_\eta = \frac{e^{-\beta(\hat{H}_\eta - \mu_\eta \hat{N}_\eta)}}{\mathrm{Tr}\left\{e^{-\beta(\hat{H}_\eta - \mu_\eta \hat{N}_\eta)}\right\}}, \tag{3.55}$$

where β is the inverse thermal energy and $\eta = \mathrm{tip/sub}$. With that, we return to Eq. 3.50, from which we trace out the tip and substrate degrees of freedom. We also apply Eq. 3.54 and obtain

$$\begin{aligned}\dot{\hat{\rho}}^I_{\mathrm{red}}(t) = &-\frac{i}{\hbar}\,\mathrm{Tr}_{\mathrm{res}}\left\{\left[\hat{H}^I_T(t), \hat{\rho}_{\mathrm{red}}(t_0)\otimes\hat{\rho}_{\mathrm{res}}\right]\right\} \\ &-\frac{1}{\hbar^2}\int_{t_0}^{t} \mathrm{d}\tau\,\mathrm{Tr}_{\mathrm{res}}\left\{\left[\hat{H}^I_{\mathrm{T}}(t), \left[\hat{H}^I_{\mathrm{T}}(\tau), \hat{\rho}^I_{\mathrm{red}}(\tau)\otimes\hat{\rho}_{\mathrm{res}}\right]\right]\right\} + \mathcal{O}((\hat{H}_{\mathrm{T}})^3).\end{aligned} \tag{3.56}$$

The first term in Eq. 3.56 vanishes, since $\hat{H}_{\mathrm{T}}$ does not conserve the particle number in the reservoirs. If we keep only the first non-vanishing order in the tunneling Hamiltonian, we are left with

$$\dot{\hat{\rho}}^I_{\mathrm{red}}(t) = -\frac{1}{\hbar^2}\int_{t_0}^{t} \mathrm{d}\tau\,\mathrm{Tr}_{\mathrm{res}}\left\{\left[\hat{H}^I_{\mathrm{T}}(t), \left[\hat{H}^I_{\mathrm{T}}(\tau), \hat{\rho}^I_{\mathrm{red}}(\tau)\otimes\hat{\rho}_{\mathrm{res}}\right]\right]\right\}. \tag{3.57}$$

If the temperature is large enough, the first step of the Markov approximation, also known as the local time approximation, is valid. To be more precise, $\hbar\Gamma_{\max} \ll k_B T$ should be satisfied, where $\Gamma_{\max}$ is the maximum rate between the molecule and the reservoirs. Thereby, $\hat{\rho}^I_{\mathrm{red}}(\tau)$ is replaced by $\hat{\rho}^I_{\mathrm{red}}(t)$ in Eq. 3.57. The second step in the Markov approximation is to extend the integral in Eq. 3.57 to $t_0 \to -\infty$, which is valid if we are only interested in the long-term behaviour of our system (times larger than the bath correlation time $\hbar\beta$). Since we only care about the stationary solution of the current ($t \to \infty$), this is always fulfilled. In fact, in this limit, the Markov approximation becomes even exact. After the transformation of variables $\tau \to t - t'$, Eq. 3.57 finally becomes

$$\dot{\hat{\rho}}^I_{\mathrm{red}}(t) = -\frac{1}{\hbar^2}\int_{0}^{\infty} \mathrm{d}t'\,\mathrm{Tr}_{\mathrm{res}}\left\{\left[\hat{H}^I_{\mathrm{T}}(t), \left[\hat{H}^I_{\mathrm{T}}(t-t'), \hat{\rho}^I_{\mathrm{red}}(t)\otimes\hat{\rho}_{\mathrm{res}}\right]\right]\right\}. \tag{3.58}$$

The next step is to write out explicitly the tunneling Hamiltonian (Eq. 3.35) and to perform the trace over the reservoirs. The density matrices of the reservoirs preserve the particle number, therefore terms with exclusively creation or annihilation operators

vanish. Mixed terms can be rewritten as

$$\begin{aligned}\mathrm{Tr}_{\mathrm{res}}\{\hat{c}^{\dagger}_{\eta\,\mathbf{k}\sigma}(t)\hat{c}_{\eta'\,\mathbf{k}'\sigma'}(t-t')\hat{\rho}_{\mathrm{res}}\} =& \,\mathrm{Tr}_{\mathrm{res}}\{\hat{c}^{\dagger}_{\eta\,\mathbf{k}\sigma}\hat{c}_{\eta\,\mathbf{k}\sigma}\hat{\rho}_{\mathrm{res}}\}e^{\frac{i}{\hbar}\epsilon t'}\delta_{\eta\eta'}\delta_{\sigma\sigma'}\delta_{\mathbf{k}\mathbf{k}'}\\ =& f^{+}_{\eta}(\epsilon_{\mathbf{k}})e^{\frac{i}{\hbar}\epsilon t'}\delta_{\eta\eta'}\delta_{\sigma\sigma'}\delta_{\mathbf{k}\mathbf{k}'}.\end{aligned} \tag{3.59}$$

Here, time dependent operators are written in the interaction picture unless indicated otherwise. We have used that the time evolution of the annihilation operators of the reservoirs is given by $c_{\eta\,\mathbf{k}\sigma}(t) = c_{\eta\,\mathbf{k}\sigma}e^{-\frac{i}{\hbar}\epsilon_{\mathbf{k}}t}$, which can be easily derived by solving the differential equation

$$\frac{\mathrm{d}}{\mathrm{d}t}\hat{c}_{\eta\,\mathbf{k}\sigma}(t) = \frac{\mathrm{d}}{\mathrm{d}t}\hat{U}^{\dagger}_{0}(t)\hat{c}_{\eta\,\mathbf{k}\sigma}\hat{U}_{0}(t) \tag{3.60}$$

with $\hat{U}_0 = e^{-\frac{i}{\hbar}(\hat{H}_{\mathrm{res}}+\hat{H}_{\mathrm{mol}})t}$. Eq. 3.60 is just the time derivative of the usual time evolution of operators in the interaction picture. In Eq. 3.59, the Fermi function $f^{+}_{\eta}(\epsilon_{\mathbf{k}}) = \frac{1}{e^{\beta(\epsilon_{\mathbf{k}}-\mu_{\eta})}+1}$ appears, since $\mathrm{Tr}_{\eta}\{\hat{c}^{\dagger}_{\eta\,\mathbf{k}\sigma}\hat{c}_{\eta\,\mathbf{k}\sigma}\hat{\rho}_{\eta}\}$ is the expectation value of the particle number operator $\hat{n}_{\eta\,\mathbf{k}\sigma}$. Similarly, we get

$$\mathrm{Tr}_{\mathrm{res}}\{\hat{c}_{\eta\,\mathbf{k}\sigma}(t)\hat{c}^{\dagger}_{\eta'\,\mathbf{k}'\sigma'}(t-t')\hat{\rho}_{\mathrm{res}}\} = f^{-}_{\eta}(\epsilon_{\mathbf{k}})e^{\frac{i}{\hbar}\epsilon t'}\delta_{\eta\eta'}\delta_{\sigma\sigma'}\delta_{\mathbf{k}\mathbf{k}'}, \tag{3.61}$$

where we have used the fermionic anticommutation relations of the annihilation and creation operators for the leads and denoted $f^{-}_{\eta}(\epsilon_{\mathbf{k}}) \equiv 1 - f^{+}_{\eta}(\epsilon_{\mathbf{k}})$.

Putting everything together and transforming it into the Schrödinger picture via

$$\dot{\hat{\rho}}^{S}_{\mathrm{red}}(t) = -\frac{i}{\hbar}[\hat{H}_{\mathrm{mol}} + \hat{H}_{\mathrm{res}}, \hat{\rho}^{S}_{\mathrm{red}}(t)] + \hat{U}_0(t)\dot{\hat{\rho}}^{I}_{\mathrm{red}}(t)\hat{U}^{\dagger}_{0}(t) \tag{3.62}$$

yields our final form of the generalized master equation for the reduced density operator

$$\begin{aligned}\dot{\hat{\rho}}^{S}_{\mathrm{red}}(t) =& -\frac{i}{\hbar}[\hat{H}_{\mathrm{mol}}, \hat{\rho}^{S}_{\mathrm{red}}(t)] - \frac{1}{\hbar^2}\int_{0}^{\infty}\mathrm{d}t' \sum_{\eta\mathbf{k}ij\sigma}\{\\ &+ t^{\eta}_{i}(\hat{Q}_D,\hat{Q}_S)\hat{d}_{i\sigma}[t^{\eta}_{j}(\hat{Q}_D,\hat{Q}_S)(-t')]^{\dagger}\hat{d}^{\dagger}_{j\sigma}(-t')\hat{\rho}^{S}_{\mathrm{red}}(t)f^{+}_{\eta}(\epsilon_{\mathbf{k}})e^{\frac{i}{\hbar}\epsilon_{\mathbf{k}}t'}\\ &+ [t^{\eta}_{i}(\hat{Q}_D,\hat{Q}_S)]^{\dagger}\hat{d}^{\dagger}_{i\sigma}t^{\eta}_{j}(\hat{Q}_D,\hat{Q}_S)(-t')\hat{d}_{j\sigma}(-t')\hat{\rho}^{S}_{\mathrm{red}}(t)f^{-}_{\eta}(\epsilon_{\mathbf{k}})e^{-\frac{i}{\hbar}\epsilon_{\mathbf{k}}t'}\\ &- t^{\eta}_{i}(\hat{Q}_D,\hat{Q}_S)\hat{d}_{i\sigma}\hat{\rho}^{S}_{\mathrm{red}}(t)[t^{\eta}_{j}(\hat{Q}_D,\hat{Q}_S)(-t')]^{\dagger}\hat{d}^{\dagger}_{j\sigma}(-t')f^{-}_{\eta}(\epsilon_{\mathbf{k}})e^{\frac{i}{\hbar}\epsilon_{\mathbf{k}}t'}\\ &- [t^{\eta}_{i}(\hat{Q}_D,\hat{Q}_S)]^{\dagger}\hat{d}^{\dagger}_{i\sigma}\hat{\rho}^{S}_{\mathrm{red}}(t)t^{\eta}_{j}(\hat{Q}_D,\hat{Q}_S)(-t')\hat{d}_{j\sigma}(-t')f^{+}_{\eta}(\epsilon_{\mathbf{k}})e^{-\frac{i}{\hbar}\epsilon_{\mathbf{k}}t'}\\ &+ H.c.\,\}\,.\end{aligned} \tag{3.63}$$

3.2.4 Rate equations and current

In order to get the rate equations of the double barrier junction, we project Eq. 3.63 onto the eigenstates $|\Psi_\beta\rangle$ of the molecular Hamiltonian. The many body eigenstates are

labelled by the multi-index $\beta = (n_{e\uparrow}, n_{e\downarrow}, n_{o\uparrow}, n_{o\downarrow}; m_D, m_S)$. By including the identities $\sum_{\beta'} |\Psi_{\beta'}\rangle\langle\Psi_{\beta'}|$ at the position of the time dependent operators, we can gather the time dependence in one exponential, which is simply a phase factor. Using the identity

$$\int_0^\infty \mathrm{d}t\, e^{\frac{i}{\hbar}Et} = \pi\hbar\delta(E) + i\hbar\mathrm{PV}\left(\frac{1}{E}\right), \tag{3.64}$$

where PV() is the principal value, it is now possible to perform the time integration over this phase factor.

As a next step, we neglect all terms with off-diagonal elements of the reduced density matrix, which is called secular approximation. These off-diagonal elements are called coherences. The secular approximation is valid, if the rates (in terms of energies) are small compared to the energy differences of the system. Therefore, coherences are especially important for systems with degeneracies. In our system, there are only spin degeneracies which are zero anyway, because we have no spin flip processes. The rate which could endanger the secular approximation is the rate between the molecule and the substrate. However, it is roughly around 1meV [27], which is small compared to typical vibrational energies in molecules. Thus, in our system the secular approximation is justified.

After taking the continuum limit $\sum_{\mathbf{k}} \to \int \mathrm{d}\epsilon_{\mathbf{k}} D_{\epsilon_{\mathbf{k}}}$ and the flat band limit for the density of states of the leads ($D_{\epsilon_{\mathbf{k}}} \to D$) we perform the integration over $\epsilon_{\mathbf{k}}$, which is easily done because of the delta distribution in Eq. 3.64.

Putting everything together, one finally gets the rate equations for the double barrier junction. It reads

$$\begin{aligned}\dot{P}_\beta(t) = &- \sum_{\eta,i,\sigma,\beta'} \left[\Gamma^{\beta\beta'}_{i\sigma\eta} f^+_\eta(\omega_{\beta'\beta}) + \Gamma^{\beta'\beta}_{i\sigma\eta} f^-_\eta(\omega_{\beta\beta'})\right] P_\beta(t) \\ &+ \sum_{\eta,i,\sigma,\beta'} \left[\Gamma^{\beta\beta'}_{i\sigma\eta} f^-_\eta(\omega_{\beta'\beta}) + \Gamma^{\beta'\beta}_{i\sigma\eta} f^+_\eta(\omega_{\beta\beta'})\right] P_{\beta'}(t),\end{aligned} \tag{3.65}$$

where $P_\beta(t) = \langle\Psi_\beta|\hat{\rho}^S_{\mathrm{red}}(t)|\Psi_\beta\rangle$ are the so-called populations of the reduced density matrix, which give the probability that the system is in the state β. The Bohr frequencies are given by $w_{\beta\beta'} = E_\beta - E'_\beta$. Crucial for the transport properties of the system are the rates, which read

$$\Gamma^{\beta\beta'}_{i\sigma\,\mathrm{sub}} \equiv \frac{2\pi}{\hbar} D_{\mathrm{sub}} |\langle\Psi_\beta| t_i^{sub}\, \hat{d}_{i\sigma} |\Psi_{\beta'}\rangle|^2 \tag{3.66}$$

and

$$\Gamma^{\beta\beta'}_{i\sigma\,\mathrm{tip}} \equiv \frac{2\pi}{\hbar} D_{\mathrm{tip}} |\langle\Psi_\beta| t_i^{\mathrm{tip}}(\hat{Q}_D, \hat{Q}_S)\, \hat{d}_{i\sigma} |\Psi_{\beta'}\rangle|^2. \tag{3.67}$$

They will be discussed in detail in Sec. 3.3.

Eq. 3.65 can be visualized in the following way. A term involving an $f^+_\eta(\omega_{\beta\beta'})$

function corresponds to a tunneling process from the lead η into the molecule, where the electron has an energy $\omega_{\beta\beta'}$. All terms with an $f_\eta^-(\omega_{\beta\beta'})$ function correspond to tunneling processes out of the molecule and into the lead η. The applied bsias enters via the chemical potentials $\mu_{\text{tip}} = \mu_0 + cV_b$ and $\mu_{\text{sub}} = \mu_0 - (1-c)V_b$, which appear in the Fermi functions. Here, V_b is written in electron volt, c determines the asymmetry of the bias drop, and μ_0 is the chemical potential of the leads without bias voltage.

It is convenient to rewrite Eq. 3.65 into matrix form, i.e.

$$\dot{\vec{P}} = \mathcal{L}\vec{P}. \tag{3.68}$$

$\mathcal{L}$ contains all the transport characteristics of the system within the approximations we made and is called Liouvillean.

In the experiment, usually the current through the molecule is measured. Therefore, it is for us desirable to compute this observable. The expectation value of the particle current flowing into the molecule is given by the time derivative of the expectation value of the particle number operator of the molecule, i.e.

$$\langle \hat{I} \rangle = \frac{\mathrm{d}}{\mathrm{d}t} \operatorname{Tr}\{\hat{\rho}(t)\hat{N}_{\text{mol}}\}. \tag{3.69}$$

Performing the trace over the reservoirs and using Eq. 3.68, yields

$$\langle \hat{I} \rangle = \operatorname{Tr}_{\text{mol}}\{\dot{\hat{\rho}}_{\text{red}}\hat{N}_{\text{mol}}\} = \sum_{\beta\beta'} N^\beta_{\text{mol}} \mathcal{L}_{\beta\beta'} P_{\beta'}, \tag{3.70}$$

where N^β_{mol} is the number of particles in the state β. We are only interested in the stationary solution, i.e. in the case $\langle \hat{I} \rangle = 0$. In this situation, the current flowing from the tip into the molecule $\langle \hat{I}^{\text{in}}_{\text{tip}} \rangle$ equals the current flowing out of the molecule into the substrate $\langle \hat{I}^{\text{out}}_{\text{sub}} \rangle$. Solving $\mathcal{L}\vec{P} = 0$ yields the populations in the stationary solution $\vec{P}^{\text{stat}}$, which are necessary to compute

$$\langle \hat{I}^{\text{in}}_{\text{tip}} \rangle = \sum_{\beta\beta'} N^\beta_{\text{mol}} \mathcal{L}^{\text{tip}}_{\beta\beta'} P^{\text{stat}}_{\beta'}, \tag{3.71}$$

which is the observable we are interested in. $\mathcal{L}^{\text{tip}}_{\beta\beta'}$ is the part of the Liouvillean which is responsible for the current between the tip and the molecule. It contains only Fermi functions of the tip. Often, one is interested in the differential conductance, which can be obtained by taking the derivative of $\langle \hat{I}^{\text{in}}_{\text{tip}} \rangle$ with respect to the bias V_b.

3.3 The rates between the molecule and the leads

The transport characteristics of our STM setup are encoded in the rates given by Eq. 3.66 and 3.67. Of special interest are the rates between the tip and the molecule, which contain tunneling matrix elements which are a function of the quantized normal mode coordinates of the molecular vibrations. The reason for this is explained in Sec. 3.1.2. As we will see, these tunneling matrix elements leads to unique dI/dV-characteristics, emerging from modified Franck-Condon factors that will be introduced in Sec. 3.3.2. First, we consider the rate between the molecule and the substrate.

3.3.1 The rates between the molecule and the substrate - The Franck-Condon factors

The rate between the molecule and the substrate, given by Eq. 3.66, can be calculated exactly on an analytical level. First, note that t_i^{sub} is just a number and can be therefore pulled out of the matrix element contained in $\Gamma^{\beta\beta'}_{i\sigma\,\text{sub}}$. Hence, we have

$$\langle\Psi_\beta|t_i^{\text{sub}}\hat{d}_{i\sigma}|\Psi_{\beta'}\rangle = t_i^{\text{sub}}\langle\beta|e^{\hat{S}}\hat{d}_{i\sigma}e^{-\hat{S}}|\beta'\rangle = t_i^{\text{sub}}\langle\beta|\tilde{\hat{d}}_{i\sigma}|\beta'\rangle, \tag{3.72}$$

where $|\Psi_\beta\rangle$ are the exact eigenstates of the molecular Hamiltonian and β labels the many body states. $\hat{S}$ is the operator used for the transformation which diagonalizes $\hat{H}_{\text{mol}}$ and $\hat{d}_{i\sigma}$ is the annihilator of an electron in an odd or even orbital, respectively. For details we refer to Sec. 3.1.1. Applying Eqs. 3.26 and 3.27, factorizing the electronic from the vibronic part, and using the orthogonality of the harmonic oscillator states, we get

$$\langle\Psi_\beta|t_i^{\text{sub}}\hat{d}_{i\sigma}|\Psi_{\beta'}\rangle = t_i^{\text{sub}}\langle\alpha|\hat{d}_{i\sigma}|\alpha'\rangle\langle m_D|e^{-\frac{g_i}{\hbar\omega_D}(\hat{a}_D^\dagger-\hat{a}_D)}|m_D'\rangle\delta_{m_S m_S'} \tag{3.73}$$

where $\alpha = (n_{e\uparrow}, n_{e\downarrow}, n_{o\uparrow}, n_{o\downarrow})$ labels the purely electronic part of the many body states, i.e. $\beta = (\alpha; m_D, m_S)$. We denote

$$F(m, m', \lambda) \equiv \left|\langle m|e^{-\lambda(\hat{a}^\dagger-\hat{a})}|m'\rangle\right|^2, \tag{3.74}$$

which are the so-called Franck-Condon (FC) factors. We omitted the subscript D since we use definition 3.74 for arbitrary modes, and introduced the dimensionless electron-vibron coupling constant $\lambda \equiv \frac{g}{\hbar\omega}$. From now on, we will omit "dimensionless" when we talk about λ. Note that the FC factors are the crucial part responsible for vibronic transitions

in the molecule-substrate rates and that they can be calculated exactly. The result reads

$$F(m,m',\lambda) = e^{-\lambda^2}\lambda^{2|m'-m|}\left(\frac{m!}{m'!}\right)^{\mathrm{sgn}(m'-m)}\left[L^{|m'-m|}_{\min(m,m')}(\lambda^2)\right]^2, \tag{3.75}$$

where $sgn()$ is the Signum function and $L^{|m'-m|}_{\min(m,m')}(\lambda^2)$ are the associated Laguerre polynomials. They are given by

$$L^k_n(x) = \sum_{m=0}^{n}(-1)^m\frac{(n+k)!}{(n-m)!(k+m)!m!}x^m. \tag{3.76}$$

A derivation of Eq. 3.75 can be found in A.3.

A more intuitive way of writing the FC factors (Eq. 3.74) is probably

$$F(m,m',\lambda) = \left[\int_{-\infty}^{\infty}\mathrm{d}Q\ \Phi_m(Q)\Phi_{m'}(Q+2\Delta x_0\lambda)\right]^2, \tag{3.77}$$

where Δx_0 is the zero-point fluctuation of the harmonic oscillator associated with the mode one considers, and $\Phi_m(Q)$ is an eigenfunction of the harmonic oscillator. We have used that $e^{-\lambda(\hat{a}^\dagger-\hat{a})}$ can be written in terms of the momentum operator of the harmonic oscillator as $e^{\frac{i}{\hbar}2\Delta x_0\lambda\hat{p}}$ and therefore generates translations. Eq. 3.77 tells us that a FC factor is just the overlap of two harmonic oscillator states where one of them is shifted. The magnitude of the shift is proportional to the electron-vibron coupling constant and the zero-point fluctuation. It is the distance between the old and the new equilibrium position of the nuclei after a charging process.

To visualize further the meaning of the FC factors, consider Fig. 3.2. It shows the so-called FC parabolas for two different electron-vibron coupling constants. For zero electron-vibron coupling we obviously have $F(m,m',\lambda) = \delta_{m,m'}$, which means that the FC parabola is a diagonal. For small electron-vibron coupling, e.g. $\lambda = 0.5$, this diagonal opens and becomes a narrow parabola, which can be seen in the left part of Fig. 3.2. In the right part, there is a strong electron-vibron coupling of $\lambda = 4$ and therefore the parabola is very wide. A large λ leads also to a suppression of transitions with small m and m', which can result in a significant current suppression at low bias voltage. This effect is termed FC blockade [28]. Also note that there are quantum oscillations in the central regions of the FC parabolas, whereas there is a strong suppression outside.

Putting everything together, we can give the final form of the molecule-substrate rate, which is

$$\Gamma^{\beta\beta'}_{i\sigma\,\mathrm{sub}} = \frac{2\pi}{\hbar}D_{\mathrm{sub}}|t^{\mathrm{sub}}_i\langle\alpha|\hat{d}_{i\sigma}|\alpha'\rangle|^2F(m_D,m'_D,\lambda_i)\delta_{m_S m'_S} \tag{3.78}$$

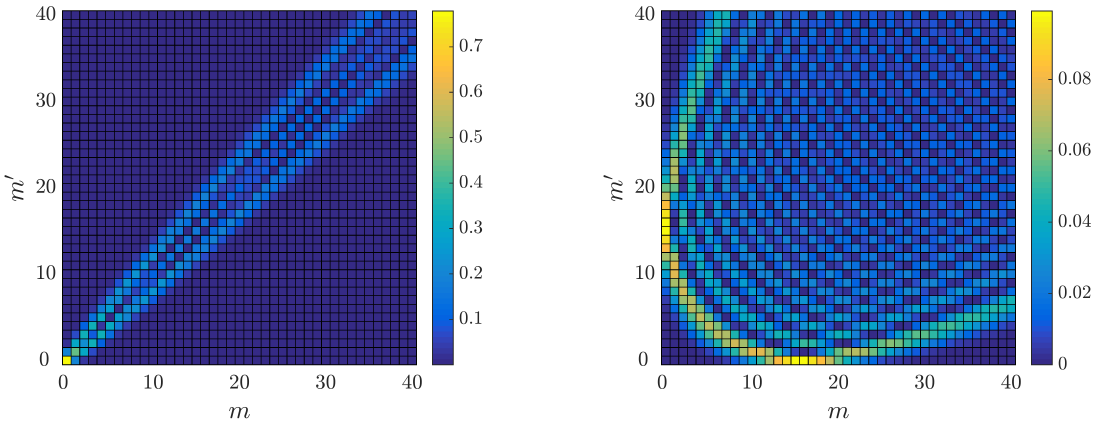

Figure 3.2: The FC parabolas for $\lambda = 0.5$ (left) and $\lambda = 4$ (right).

with $\lambda_i = \frac{g_i}{\hbar\omega_D}$.

3.3.2 The rates between the molecule and the tip - The modified Franck-Condon factors

In this section we analyze the tip-molecule rate, given by Eq. 3.67. We are interested in the matrix element which is contained in the rate. It can be written as

$$\langle \Psi_\beta | t_i^{\text{tip}}(\hat{Q}_D, \hat{Q}_S)\hat{d}_{i\sigma} | \Psi_{\beta'} \rangle = \langle \beta | \tilde{t}_i^{\text{tip}}(\hat{Q}_D, \hat{Q}_S)\tilde{\hat{d}}_{i\sigma} | \beta' \rangle, \tag{3.79}$$

where we have used the unitarity of the Lang Firsov transformation. We need to calculate the transformed tunneling matrix element

$$\tilde{t}_i^{\text{tip}}(\hat{Q}_D, \hat{Q}_S) = e^{\hat{S}} t_i^{\text{tip}}(\hat{Q}_D, \hat{Q}_S) e^{-\hat{S}}, \tag{3.80}$$

which is done in A.4. The result is

$$\tilde{t}_i^{\text{tip}}(\hat{Q}_D, \hat{Q}_S) = t_i^{\text{tip}}\left(\hat{Q}_D - \Delta\hat{Q}_D, \hat{Q}_S\right), \tag{3.81}$$

where we have denoted

$$\Delta\hat{Q}_D \equiv 2\Delta x_{0D} \sum_\sigma \left[\lambda_e(\hat{n}_{e\sigma} - 1) + \lambda_o \hat{n}_{o\sigma}\right]. \tag{3.82}$$

Δx_{0D} labels the zero-point fluctuation of the D-mode. We insert $\tilde{t}_i^{\,\mathrm{tip}}(\hat{Q}_D, \hat{Q}_S)$ and $\tilde{\hat{d}}_{i\sigma}$ into Eq. 3.79, apply $\Delta\hat{Q}_D$ which contains electronic operators to the bra $\langle\beta|$, and factorize the electronic from the vibronic part. This leads to

$$\begin{aligned}\langle\Psi_\beta|t_i^{\mathrm{tip}}(\hat{Q}_D, \hat{Q}_S)\hat{d}_{i\sigma}|\Psi_{\beta'}\rangle = \\ \langle\alpha|\hat{d}_{i\sigma}|\alpha'\rangle\langle m_D, m_S|t_i^{\,\mathrm{tip}}\left(\hat{Q}_D - \Delta Q_D^\alpha, \hat{Q}_S\right)e^{-\lambda_i(\hat{a}_D^\dagger - \hat{a}_D)}|m'_D, m'_S\rangle,\end{aligned} \tag{3.83}$$

where $\langle\alpha|\Delta\hat{Q}_D = \langle\alpha|\Delta Q_D^\alpha$.

Nontrivial in Eq. 3.83 is the vibronic part. Its square is similar to the FC factors, but modified by the tunneling matrix element between the tip and the molecule. Thus we denote

$$\left|\langle m_D, m_S|t_i^{\,\mathrm{tip}}\left(\hat{Q}_D - \Delta Q_D^\alpha, \hat{Q}_S\right)e^{-\lambda_i(\hat{a}_D^\dagger - \hat{a}_D)}|m'_D, m'_S\rangle\right|^2 \tag{3.84}$$

modified FC (MFC) factors. Note that it is not possible to factorize the vibronic D-mode part from the vibronic S-mode part, nor to pull out the tunneling matrix element. For interpretation purposes, we rewrite the MFC factors into integral form and use Chen's derivative rule. Neglecting the constant prefactor, this gives

$$\left[\int_{-\infty}^{\infty}\mathrm{d}Q_D\int_{-\infty}^{\infty}\mathrm{d}Q_S\,\Phi_{m_D}(Q_D)\Phi_{m_S}(Q_S)\Psi_i(\mathbf{r}_{\mathrm{tip}}; Q_D - \Delta Q_D^\alpha, Q_S)\Phi_{m'_D}(Q_D + \sqrt{2}\Delta x_{0D}\lambda_i)\Phi_{m'_S}(Q_S)\right]^2. \tag{3.85}$$

From now on, we will only consider the odd molecular orbital ($i = o$) because it has varying local symmetries, whereas the even orbital has only s-symmetry. This is the more interesting case for us, since we want to study the effect of different local symmetries of the molecule on the transport characteristics of STM.

The origin of vibron-assisted tunneling

Calculating the integrals in Eq. 3.85 numerically, one gets the MFC factors for a certain tip position and electron-vibron coupling constant. In order to visualize them as the FC factors in Fig. 3.2, one has to fix at least two of the four indices m_D, m_S, m'_D, m'_S or plot them in a tensor product way. The latter is done in Figs. 3.3(a)-(c), which show the MFC factors for tip positions indicated in Fig. 3.3(d). Each of the Figs. 3.3(a)-(c) can be divided into 5x5-blocks, where each block corresponds to a specific D-mode transition and consists of several S-mode transitions. The blocks are specified by blue braces and labelled by blue numbers. The content of each block (i.e. the S-mode

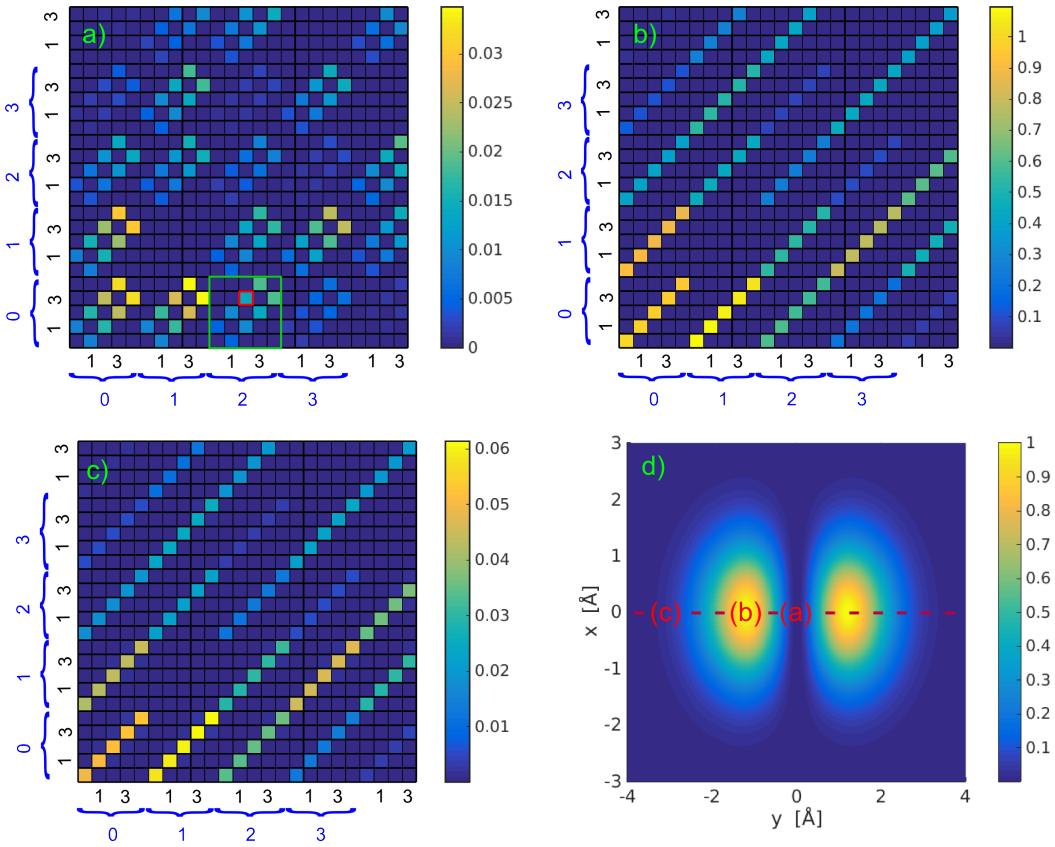

Figure 3.3: (a,b,c) show the MFC factors for tip positions indicated in (d) and for a electron-vibron coupling constant $\lambda_o = 1$. They are normalized to the ground to ground state transition in (b). Since the MFC factors have four indices, they are visualized in a tensor product way. $|m_D, m_S\rangle = |m_D\rangle \otimes |m_S\rangle$ runs along the horizontal axis and $|m'_D, m'_S\rangle = |m'_D\rangle \otimes |m'_S\rangle$ along the vertical axis. The black numbers label the S-mode states, the blue numbers the D-mode states. The MFC factors are calculated with zero-point fluctuations of $\Delta x_{0S} = a/10$ and $\Delta x_{0D} = a/20$, where $a = 1.34$Å is the distance between the two p_z-orbitals. Note that there is a large effect of Δx_{0S} on the MFC factors, which is discussed in detail in Sec. 5.4. (d) shows a constant height current map of the odd molecular orbital. The current is normalized to its maximum value.

transitions) is labelled by black numbers. As an example we have indicated the transition $(m_D = 2, m_S = 2) \to (m'_D = 0, m'_S = 3)$ by a red square in Fig. 3.3(a). The green square corresponds to the block $(m_D = 2, m'_D = 0)$. Within this block the red square corresponds to $(m_S = 2, m'_S = 3)$.

First, we analyze the structure of the MFC factors with respect to D-mode transitions. This means that we consider entire blocks. For comparison, Fig. 3.4(a) shows the corresponding unmodified FC factors for one mode. Clearly, one recognizes the structure

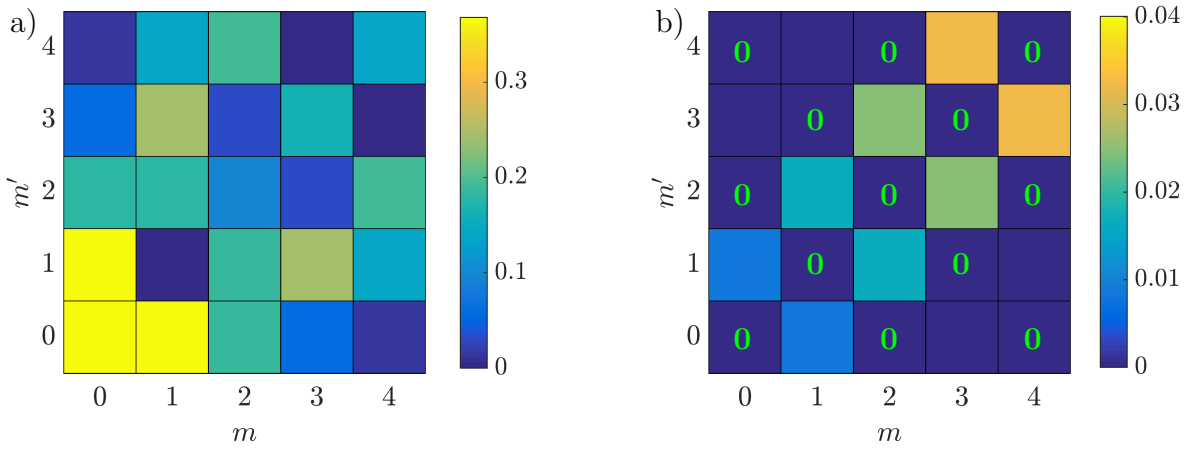

Figure 3.4: (a) shows the FC factors for $\lambda = 1$. (b) shows the MFC factors for the S-mode with $m_D = m'_D = 0$. The parameters are chosen as in Fig. 3.3.

of the unmodified FC factors by comparing D-mode blocks of the MFC factors. For example, the transition $m = 1 \to m' = 1$ in Fig. 3.4(a) corresponds to the blocks $(m_D = 1, m'_D = 1)$ in Figs. 3.3(a)-(c) and both are vanishing. However, there are also differences. For example, there is an asymmetry with respect to the diagonal in the MFC factors, which becomes even stronger if the tip is positioned on the outside of the orbital lobe (Fig. 3.3(c)). This means that the preference of heating or cooling the system via vibron excitations depends on whether an electron is attached or detached.

Nonetheless, the effect of the tunneling matrix element between the tip and the molecule on the structure of the D-mode blocks of the MFC factors is relatively small. In particular, vibron-assisted tunneling cannot be explained by the D-mode. According to Fig. 3.3(a), vibrational ground to ground state transitions with respect to the S-mode vanish for all (m_D, m'_D) if the tip is positioned above the nodal plane. Therefore, one would not observe differential conductance peaks at any bias without the S-mode for that tip position. This can also be explained by Eq. 3.85. The odd molecular wave function without the S-mode is zero for all Q_D if the tip is positioned above the nodal plane. The reason for that is that the position of the nodal plane is not changed by the D-mode.

Now, let us concentrate on the S-mode. In Fig. 3.3(a), the blocks are off-diagonal, whereas in Fig. 3.3(b,c) they are diagonal. Therefore, the transition $m_S = 0$ to $m'_S = 0$ if the tip is above the nodal plane is forbidden, but $m_S = 0$ to $m'_S = 1$ is allowed. Instead, for tip positions above the maximum of the orbital, the transition $m_S = 0$ to $m'_S = 0$ is allowed. These simple observations show that the reason for the vibron-assisted tunneling effect can indeed be found in the MFC factors, and that the crucial component is a mode which moves the nodal plane.

Fig. 3.4(b) shows one of these S-mode blocks of Fig. 3.3(a), which means that m_D and m'_D are fixed. The transitions which are exactly zero are marked. Obviously, there is a selection rule, namely $m_S + m'_S$ must be an odd number in order to get a nonvanishing rate. In the next part, we will see that one can deduce this selection rule directly from Eq. 3.85.

Selection rule

In order to derive the selection rule, we analyze the odd molecular wave function Ψ_o. Fig. 3.5(a) shows Ψ_o for fixed x_tip and z_tip as a function of y_tip, Fig. 3.5(b) shows Ψ_o as a function of Q_S for $y_\mathrm{tip} = y_\mathrm{np}$ and fixed x_tip and z_tip. Here, y_np denotes the tip position above the nodal plane. Except for the direction of the axis, a) and b) look the same, which means that Ψ_o is not only an odd function of y_tip but also of Q_S. The reason for this is, that the S-mode moves both atoms in phase. This leads to the first selection rule, since the two harmonic oscillator functions for the S-mode in Eq. 3.85 need to have different symmetries in order to cancel the odd symmetry of Ψ_o and to get a non-vanishing rate. In other terms, we have

$$\Gamma^{\beta\beta'}_{i\sigma\,\mathrm{tip}} = 0 \quad \text{for} \quad m_S + m'_S = 2n \quad \text{with} \quad n \in \mathbb{N}_0, \tag{3.86}$$

for $y_\mathrm{tip} = y_\mathrm{np}$. This works also for non-zero Q_D, because the D-mode respects the symmetry of Ψ_o.

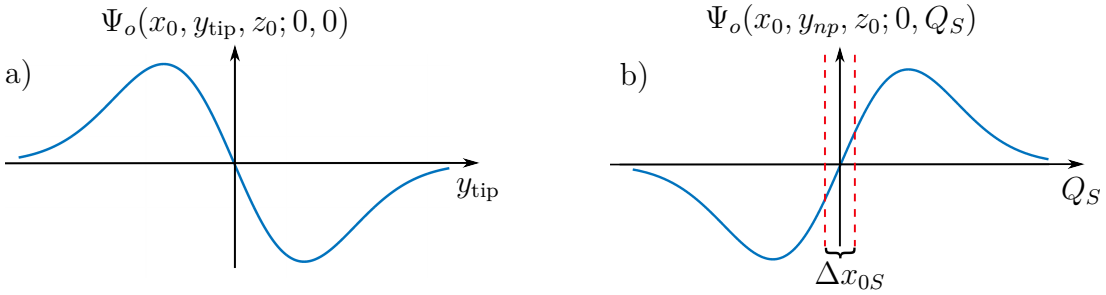

Figure 3.5: Odd molecular orbital as a function of (a) y_tip and (b) Q_S.

The case that the entire orbital is an odd function with respect to the normal mode coordinate is rather special. Therefore, we want to emphasize that this condition is not necessary. It is enough that the position of the tip is above a nodal plane of the molecular orbital. The explanation for that can be seen in Fig. 3.5(b). Only a tiny region with a length of a few Δx_{0S} around $Q_S = 0$, marked via the red dashed lines, contributes to the integral in Eq. 3.85. This is because outside this region, the harmonic oscillator states are exponentially suppressed. Within this region, the orbital is obviously linear in Q_S, i.e.

can be written as $\Psi_o \propto Q_S$. Therefore the integrals in Eq. 3.85 can be separated and we are left with

$$\Gamma^{\beta\beta'}_{i\sigma\,\mathrm{tip}} \propto \left[\int_{-\infty}^{\infty} \mathrm{d}Q_S \; \Phi_{m_S}(Q_S) Q_S \Phi_{m'_S}(Q_S) \right]^2 , \tag{3.87}$$

where we directly see selection rule 3.86 again.

Another selection rule emerges from the situation where the tip is positioned directly above the maximum of an orbital lobe. According to Fig. 3.6, we have $\Psi_o \propto 1 - Q_S^2$ in the region which contributes to the integral in Eq. 3.85 for $Q_D = 0$. Therefore, the integral over the normal mode coordinate of the S-mode is given by

$$\int_{-\infty}^{\infty} \mathrm{d}Q_S \; \Phi_{m_S}(Q_S)(1 - Q_S)^2 \Phi_{m'_S}(Q_S) = \delta_{m_S, m'_S} - \int_{-\infty}^{\infty} \mathrm{d}Q_S \; \Phi_{m_S}(Q_S) \; Q_S^2 \; \Phi_{m'_S}(Q_S), \tag{3.88}$$

which leads to a selection rule for $y = y_{\max}$. It reads

$$\Gamma^{\beta\beta'}_{i\sigma\,\mathrm{tip}} = 0 \quad \text{for} \quad m_S + m'_S = 2n + 1 \quad \text{with} \quad n \in \mathbb{N}_0. \tag{3.89}$$

Summarizing, one can say that Eq. 3.85 explains the vibron-assisted tunneling effect on a qualitative level and gives additional information about all possible transitions. In particular, selection rules emerge for special positions of the tip.

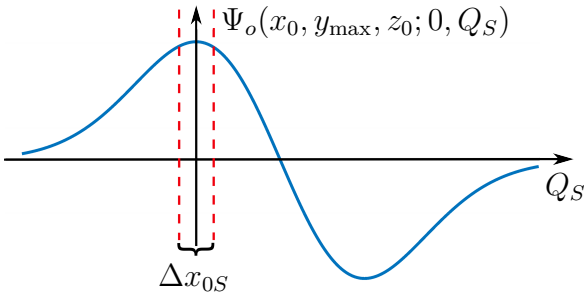

Figure 3.6: Odd molecular orbital as a function of Q_S for $y_{\mathrm{tip}} = y_{\max}$. The red dashed lines indicate the region in which the harmonic oscillator functions contribute to the MFC factors. Outside this region, they are exponentially suppressed.

However, by comparing the scales in Fig. 3.3(a) and (b), it is obvious that the MFC factors for $y = y_{\mathrm{np}}$ are much smaller (about a factor of $\sim 10^2$) than the MFC factors for $y = y_{\max}$. This makes sense if one compares Fig. 3.5(b) to Fig. 3.6. Inside the region of the red dashed lines, the molecular wave function in Fig. 3.5(b) is much smaller than in Fig. 3.6 and thus the MFC differ by two orders of magnitude. This rather important fact obviously depends on the size of the zero-point fluctuation and is discussed in detail in Sec. 5.4.

3.4 Model with relaxation rate

In the last section, we showed that only the S-mode leads to the vibron-assisted tunneling effect (see also Sec. 4.2). Moreover, in order to study the effect of a vibronic degree of freedom in the molecule in combination with different local symmetries of the molecular wave function, it is enough to take into account only one spinless electronic state. Therefore, we consider a simplified model with one spinless odd molecular orbital and a vibronic S-mode in this section. Furthermore, we add an additional relaxation term, which brings the system into thermal equilibrium with a certain rate, to the Liouvillean. The physical origin for this term is for instance vibron-phonon coupling to the insulating film.

The Hamiltonian for the simplified molecular system can be written as

$$\hat{H}_{\mathrm{mol}}^{\mathrm{sim}} = \epsilon\hat{N} + g\hat{N}\left(\hat{a}^\dagger + a\right) + \hbar\omega\left(\hat{a}^\dagger\hat{a} + \frac{1}{2}\right). \tag{3.90}$$

g quantifies the electron-vibron coupling, $\hat{N} = d^\dagger d$ is the particle number operator of the molecular system and $d^\dagger$ creates an electron in the molecular orbital. $\hat{a}$ is the annihilation operator of an S-type mode, i.e. a mode which moves the atoms in phase. Using the Lang Firsov transformation, $\hat{H}_{\mathrm{mol}}^{\mathrm{sim}}$ can be diagonalized in a similar way as the Hamiltonian in Sec. 3.1.1. The diagonalization leads to

$$\tilde{\hat{H}}_{\mathrm{mol}}^{\mathrm{sim}} = e^{\hat{S}}\hat{H}_{\mathrm{mol}}^{\mathrm{sim}}e^{-\hat{S}} = \epsilon\hat{N} + \hbar\omega\left(\hat{a}^\dagger\hat{a} + \frac{1}{2}\right) - \frac{g^2}{\hbar\omega}\hat{N}^2, \tag{3.91}$$

where $\hat{S} \equiv \lambda\hat{N}(\hat{a}^\dagger - \hat{a})$ with $\lambda \equiv \frac{g}{\hbar\omega}$.

The eigenstates of $\hat{H}_{\mathrm{mol}}^{\mathrm{sim}}$ can be labelled by one electronic quantum number ($n \in \{0, 1\}$) and one vibronic quantum number ($m \in \mathbb{N}_0$). They are given by

$$|\Psi_{n;m}\rangle = e^{-S}|n; m\rangle \tag{3.92}$$

with the eigenenergies E_{nm}

$$\begin{aligned} E_{0m} &= \hbar\omega\left(m + \frac{1}{2}\right) \\ E_{1m} &= \epsilon - \frac{g^2}{\hbar\omega} + \hbar\omega\left(m + \frac{1}{2}\right). \end{aligned} \tag{3.93}$$

The rate equations 3.65 hold also for the simplified system, except that the degrees of freedom of the molecular orbital and the spin are gone. The relaxation rate is included

into the rate equations phenomenologically, as for example done in [28]. This leads to

$$\begin{aligned}\dot{P}_\beta(t) = &-\sum_{\eta,\beta'}\left[\Gamma_\eta^{\beta\beta'} f_\eta^+(\omega_{\beta'\beta}) + \Gamma_\eta^{\beta'\beta} f_\eta^-(\omega_{\beta\beta'})\right] P_\beta(t) \\ &+\sum_{\eta,\beta'}\left[\Gamma_\eta^{\beta\beta'} f_\eta^-(\omega_{\beta'\beta}) + \Gamma_\eta^{\beta'\beta} f_\eta^+(\omega_{\beta\beta'})\right] P_{\beta'}(t) \\ &-\frac{1}{\tau}\left[P_{nm} - P_m^{\mathrm{eq}}\sum_{m'} P_{nm'}\right],\end{aligned} \tag{3.94}$$

where $\beta = (n;m)$ labels the eigenstates, τ is the relaxation time and P_m^{eq} is the thermal vibron distribution, i.e.

$$P_m^{\mathrm{eq}} = \frac{e^{-\beta\hbar\omega\left(m+\frac{1}{2}\right)}}{\sum_m e^{-\beta\hbar\omega\left(m+\frac{1}{2}\right)}}. \tag{3.95}$$

In equilibrium ($\mu_{\mathrm{tip}} = \mu_{\mathrm{sub}}$), the solution of Eq. 3.94 is given by the grand canonical distribution (as in the case without relaxation term). In out-of equilibrium conditions, the relaxation term thermalizes only the vibronic part of the populations, i.e. it does not change the number of electrons. This can be explained by considering the time derivative of the probability of the occupation number of electrons $\sum_m \dot{P}_{nm}$, which does not get any contribution by the relaxation term. The reason for this is that

$$\sum_m\left[P_{nm} - P_m^{\mathrm{eq}}\sum_{m'} P_{nm'}\right] = 0, \tag{3.96}$$

since $\sum_m P_m^{\mathrm{eq}} = 1$.

Similar to Eq. 3.66 and 3.67, the rates are given by

$$\Gamma_{\mathrm{sub}}^{\beta\beta'} \equiv \frac{2\pi}{\hbar} D_{\mathrm{sub}} |\langle\Psi_\beta| t^{sub}\, \hat{d} |\Psi_{\beta'}\rangle|^2 \tag{3.97}$$

and

$$\Gamma_{\mathrm{tip}}^{\beta\beta'} \equiv \frac{2\pi}{\hbar} D_{\mathrm{tip}} |\langle\Psi_\beta| t^{\mathrm{tip}}(\hat{Q})\, \hat{d} |\Psi_{\beta'}\rangle|^2. \tag{3.98}$$

The tunneling matrix element between an s-symmetric tip and our molecular orbital Ψ_o reads

$$t^{\mathrm{tip}}(\hat{Q}) = \frac{2\pi\hbar^2 C_S}{m\kappa}\Psi_o(\mathbf{r}_{\mathrm{tip}};\hat{Q}), \tag{3.99}$$

where

$$\Psi_o(\mathbf{r}_{\mathrm{tip}};\hat{Q}) = \frac{1}{\sqrt{2}}\left[p\left(x_{\mathrm{tip}}, y_{\mathrm{tip}} + \frac{a}{2} - \hat{Q}, z_{\mathrm{tip}}\right) - p\left(x_{\mathrm{tip}}, y_{\mathrm{tip}} - \frac{a}{2} - \hat{Q}, z_{\mathrm{tip}}\right)\right]. \tag{3.100}$$

For the notation we refer to the end of Sec. 3.1.1. The transformed tunneling matrix

element $\tilde{t}^{\mathrm{tip}}(\hat{Q}) = e^{\hat{S}} t^{\mathrm{tip}}(\hat{Q}) e^{-\hat{S}}$ can be calculated similar as in A.4, which yields

$$\tilde{t}^{\mathrm{tip}}(\hat{Q}) = t^{\mathrm{tip}}(\hat{Q} - \sqrt{2}\Delta x_0 \lambda \hat{N}). \tag{3.101}$$

In Sec. 5, we analyse numerically the transport characteristics of the simplified model introduced in this section. In particular, we will focus on the effect of the relaxation rate.

4

Numerical results obtained for the model without relaxation rate

In this chapter, we show the results obtained with a numerical implementation of the Liouville-equation approach, which is applied to the system specified in Sec. 3.1.

In the program, the Liouvillean $\mathcal{L}$ (defined by Eqs. 3.68 and 3.65) is constructed by computing the spectrum (Eq. 3.33) and the corresponding Bohr frequencies which are needed for the Fermi functions. Moreover, the rates between the molecule and the leads are required. Using the analytical expression for the FC factors given by Eq. 3.75, yields the exact rates between the molecule and the substrate (Sec. 3.3.1). The rates between the tip and the molecule (Sec. 3.3.2) are computed by writing the operators as finite dimensional matrices acting in a restricted finite dimensional Hilbert space. Here, only states which contribute to the transport through the molecule are taken into account.

We are interested in the populations of the stationary solution, i.e. in the solution of $\dot{\vec{P}} = 0$. Because of Eq. 3.68, this solution is simply given by the kernel of the Liouvillean. The stationary populations and the Liouvillean are then used to compute the current via Eq. 3.71. Finally, the derivative with respect to the bias gives the desired differential conductance.

4.1 Stability diagram of the model molecule

Studying simultaneously the entire electronic structure of our model molecule and its vibrational degree of freedom is unnecessarily complicated. In particular, we are mainly interested in the effects of the vibrational degree of freedom on the transport characteristics of STM. Therefore, it is convenient to restrict ourselves to one certain electronic transition and to study the vibrational structure in full detail. This is possible because the energy scale of the electronic transitions is much larger than the energy scale of the vibrational ones. In order to find a suitable bias and chemical potential range, we examine the so-called stability diagram of our system. It shows the differential conductance as a function of bias voltage V_b and zero-bias chemical potential μ_0.

A stability diagram which shows the entire electronic structure of our model molecule is given in Fig. 4.1(a). Here, the leads are two identical substrates. In several Coulomb Diamonds the occupation of the states is given. For example, within the central diamond, there are two electrons in the even and zero electrons in the odd molecular orbital.

In order to study the effect of different local symmetries of the molecular orbital on the transport characteristics of STM, it is necessary to choose an electronic transition which corresponds to a tunneling process into an odd molecular orbital. Fig. 4.1(b) shows the part of Fig. 4.1(a) that is indicated with the green box. The red arrow crosses a $\mathrm{d}I/\mathrm{d}V$-peak which corresponds to the transition $|n_e = 2, n_o = 1\rangle$ to $|n_e = 2, n_o = 2\rangle$, where $n_{e/o} = \sum_\sigma n_{e/o\,\sigma}$. Since one electron is added to the odd molecular orbital, this transition is suitable for us.

Fig. 4.1(c) shows a stability diagram where the bias and the chemical potential range are given by the green box depicted in Fig. 4.1(b). Here, vibrational excitation lines appear because electron-vibron coupling to the D-mode is turned on. The entire peak structure has to correspond to the same electronic resonance, namely to the resonance between the two states $|n_e = 2, n_o = 1\rangle$ and $|n_e = 2, n_o = 2\rangle$. The reason for this is that the other electronic states are not in the given energy range. Since both leads are extended substrates, S-mode excitations are not allowed (Eq. 3.78). Therefore, all excitation lines correspond to the D-mode.

4.2 Transport near the charge degeneracy point

In this section, we analyze the particularly simple situation where μ_0 is very close to the charge degeneracy point (CDP) of the many body states $|n_e = 2, n_o = 1\rangle$ and $|n_e = 2, n_o = 2\rangle$. This CDP is marked in Fig. 4.1(c) with a red circle. More precisely, we choose μ_0 such that the distance to the CDP is smaller than one vibron energy $\hbar\omega$.

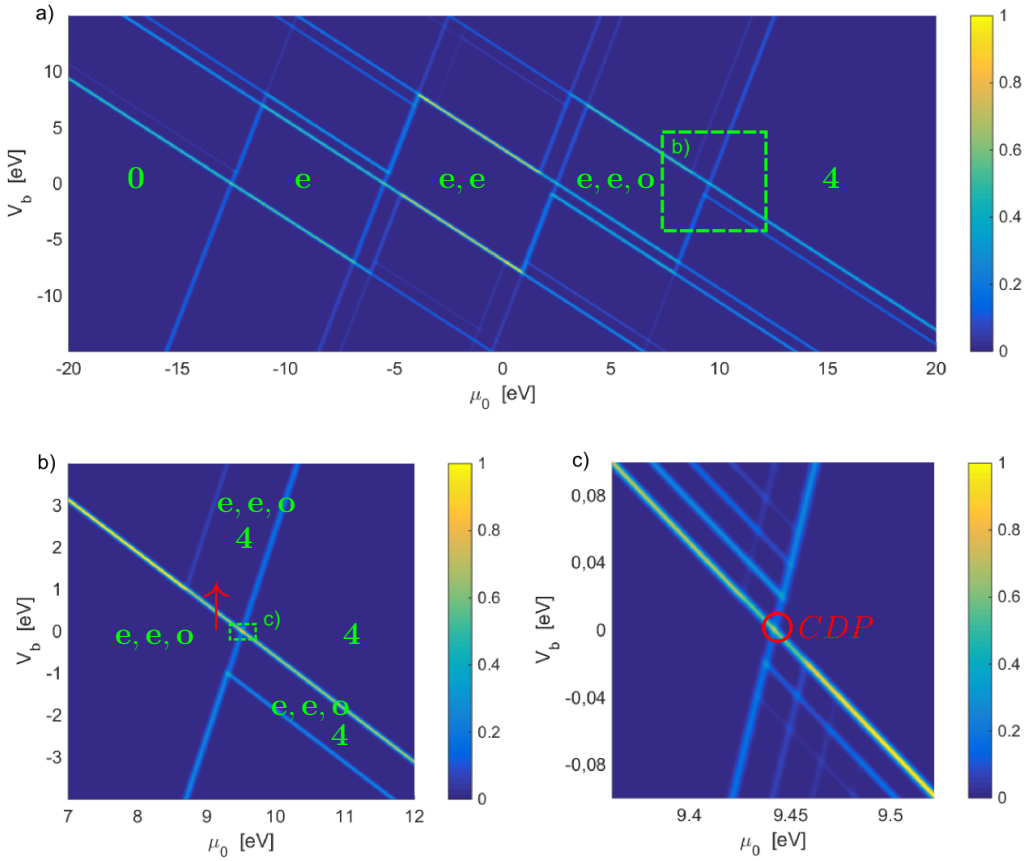

Figure 4.1: (a - c) show the differential conductance as a function of bias voltage V_b and zero-bias chemical potential μ_0. The leads are two identical substrates and their chemical potential is given by $\mu_1 = \mu_0 + cV_b$ and $\mu_2 = \mu_0 - (1-c)V_b$, where c determines the bias drop between the leads and the molecule. Each diagram is normalized to the maximum of the differential conductance independently. The values for the parameters are the following: $\epsilon_e = -2$, $\epsilon_o = -1$, $U = 7$, $c = 0.8$. All energies are given in electron volts. The temperature varies from one plot to the other and is chosen such that there is an appreciable width of the differential conductance lines and a suitable spectral resolution. The values are: (a) 50meV, (b) 20meV, (c) 1meV. The occupation of the states is indicated in some of the Coulomb diamonds. "e/o" means that one electron is in the even/odd orbital, "0" means no electrons at all. "4" labels the many body state where all orbitals are fully occupied. In (c), electron-vibron coupling to the D-mode with $\lambda_o = 1$ is turned on. The charge degeneracy point (CDP) is marked with a red circle.

Additionally, we consider a bias drop which is totally asymmetric ($c = 1$) and include a small electron-vibron coupling to the S-mode ($\lambda_S = 10^{-3}$). The latter opens the diagonal FC parabola of the S-mode in the substrate rate. Hence, also off-diagonal transitions

are allowed, at least with a small probability. This is physically reasonable, even though we showed in Sec. 3.1.1 that $\lambda_S = 0$. The reason for this is that we only considered the molecule alone without any environment. In reality, an additional charge on the molecule will change the electrostatics with respect to the substrate, which leads to a change in the equilibrium position of the molecule and thus to $\lambda_S \neq 0$. Besides, there is an electron-vibron coupling to the S-mode, if this mode is assumed to model the local dynamics of a large molecule instead of being an external mode which moves the entire molecule without changing its configuration. Therefore, the case where λ_S is exactly zero, seems rather artificial.

Fig. 4.2 shows the free energy diagram for the situation described in the paragraph above but simplified to one mode. This time we consider one tip and one substrate as leads. The tip-molecule tunneling process, depicted by the thin arrow, corresponds to the transition $|n_e = 2, n_o = 1; m = 0\rangle$ to $|n_e = 2, n_o = 2; m = 4\rangle$. Because of the huge substrate rates (compared to the tip rate), depicted by the thick arrows, the molecule will end up very fast in its ground state after each tip transition. Hence, the populations of the stationary solution of the two degenerate ground states are $P^{\text{stat}}_{n_e=2,n_o=1;m=0} \approx 1$, which translates into $P^{\text{stat}}_{n_e=2,n_o=1;m_D=0,m_S=0} \approx 1$ for the system with two modes.

In this simple situation, the current given by Eq. 3.71 can be written as

$$\langle \hat{I}^{\text{in}}_{\text{tip}} \rangle = \sum_{m_D, m_S} W^{\text{tip}}_{m_D m_S} f^{+}_{\text{tip}}(\Delta E_{m_D m_S}), \tag{4.1}$$

where

$$\begin{aligned} W^{\text{tip}}_{m_D m_S} &\equiv \Gamma^{(1,1,0,1;0,0)(1,1,1,1;m_D,m_S)}_{o\uparrow\,\text{tip}} + \Gamma^{(1,1,1,0;0,0)(1,1,1,1;m_D,m_S)}_{o\downarrow\,\text{tip}} \\ &= \frac{4\pi}{\hbar} D_{\text{tip}} |\langle 0,0| t_o^{\text{tip}} \left(\hat{Q}_D - \Delta Q_D^{(n_e=2,n_o=1)}, \hat{Q}_S \right) e^{-\lambda_o(\hat{a}_D^\dagger - \hat{a}_D)} |m_D, m_S\rangle|^2 \end{aligned} \tag{4.2}$$

and

$$\Delta E_{m_D m_S} = \omega_{(n_e=2,n_o=2;m_D,m_S)(n_e=2,n_o=1;0,0)} = E_{n_e=2,n_o=2;m_D,m_S} - E_{n_e=2,n_o=1;0,0}. \tag{4.3}$$

The notation for the tip rates Γ can be found in Sec. 3.2.4. According to Eqs. 4.1 and 4.2, one is probing the MFC factors by measuring the current (or the differential conductance) as a function of the bias voltage. More precisely, only MFC factors that contain a vibrational ground state are involved. We emphasize, that all of this is only true for the particular situation we consider here. Nevertheless, it is a suitable starting point for further investigations and for consistency checks.

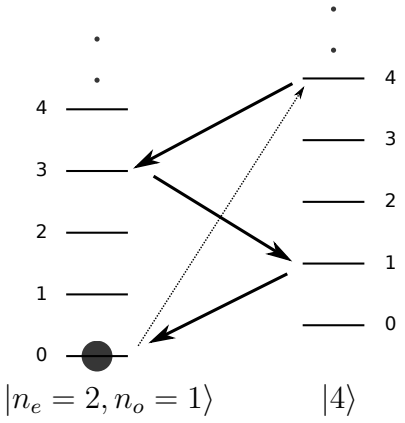

Figure 4.2: Free energy ($\hat{H} - \mu_0 \hat{N}$) diagram for μ_0 in the range $\mu_{CDP} - \hbar\omega < \mu_0 < \mu_{CDP}$, where μ_{CDP} is the chemical potential at the CDP. The two columns correspond to the two electronic states $|n_e = 2, n_o = 1\rangle$ and $|n_e = 2, n_o = 1\rangle \equiv |4\rangle$. Note that $|n_e = 2, n_o = 1\rangle$ is two-fold degenerate. Each of these electronic states has vibronic excitations which are given by the horizontal lines and labeled by the harmonic oscillator quantum numbers. For simplicity, only one mode is depicted, thus the vibronic energies are equidistant. As an example, some of the possible lead transitions are plotted. The thin arrow depicts a tip transition and the thick arrows represent substrate transitions.

4.2.1 Verification of the numerical code with the Poisson distribution

As described in the previous section, under certain conditions one is probing the MFC factors by measuring the differential conductance. This fact can be used to verify part of our numerical code, as is discussed in the following.

We consider again the situation from the last section, but we choose two substrates as leads, where one of them has a much smaller rate compared to the other one. This means that we will verify the program without the tip-molecule tunneling matrix element. We restrict ourselves to a situation where the bias drop occurs entirely between the substrate with the smaller rate and the molecule. Moreover, we consider the case $\hbar\omega_S \to \infty$ (i.e. we consider only the D-mode), and $\mu_0 = \mu_{\mathrm{CDP}} - 0.5\hbar\omega$.

As explained in the previous section, for these parameters and for reasonable electron-vibron coupling only the ground state is occupied (see Fig. 4.2). It follows that we probe the FC factors by measuring the differential conductance. Note that we do not probe the MFC factors because we do not consider a vibronic mode dependent tunneling matrix element. To be more precise, we are probing

$$F(0, m, \lambda) = \frac{\lambda^{2m}}{m!} e^{-\lambda^2}, \tag{4.4}$$

where we have used Eq. 3.75 to compute the FC factors. Eq. 4.4 is directly related to

the Poisson distribution $P_\nu(k)$, which reads

$$P_\nu(k) = \frac{\nu^k}{k!} e^{-\nu}. \tag{4.5}$$

For $\nu = \lambda^2$ the two functions coincide. Hence, the relative height of the differential conductance peaks should be given by the Poisson distribution.

Fig. 4.3(a) shows the differential conductance as a function of V_b for $\lambda_o = 1$. Fig. 4.3(b) depicts the Poisson distribution for $\nu = 1$. To allow a convenient comparison, the differential conductance in Fig. 4.3(a) is normalized to its maximum and multiplied by the maximum of the Poisson distribution.

As expected, both figures match perfectly. Thus, our numerical code without the tip-molecule tunneling matrix element seems to give correct results.

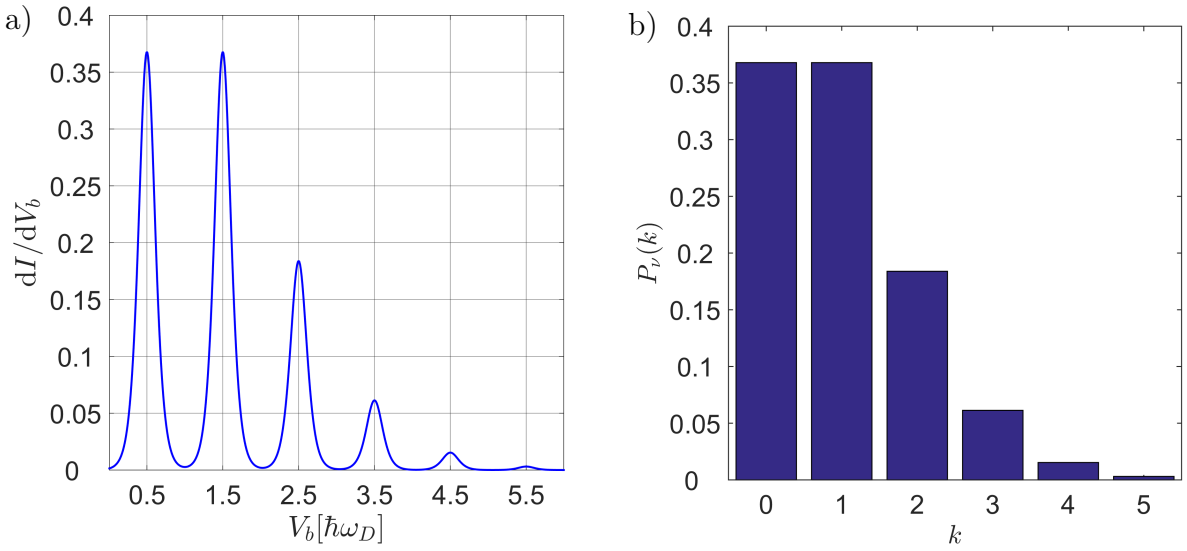

Figure 4.3: (a) shows the differential conductance for $\lambda_o = 1$, $\mu_0 = \mu_{\mathrm{CDP}} - 0.5\hbar\omega$, and $c = 1$. (b) shows the Poisson distribution for $\nu = 1$.

4.2.2 Vibron-assisted tunneling

In this section, we will address the vibron-assisted tunneling effect in the situation described in the beginning of Sec. 4.2 (i.e. $\mu_{CDP} - \hbar\omega < \mu_0 < \mu_{CDP}$). Fig. 4.4(a) shows the differential conductance as a function of the tip position and the bias voltage. The tip position runs along the long axis of the molecule, which is indicated by the dashed red line in Fig. 3.3(d). The energy of the D-mode is about ten times larger than the energy of the S-mode, which could for example model the fact that a chemical bond is

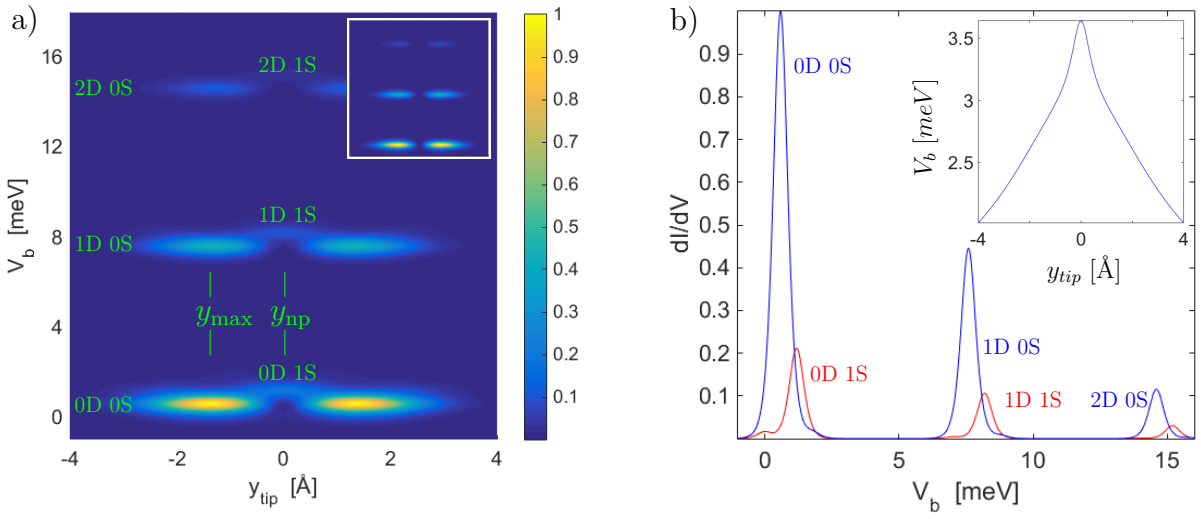

Figure 4.4: (a) shows the differential conductance as a function of the bias voltage and the tip position, which runs along the long axis of the molecule. The $\mathrm{d}I/\mathrm{d}V$ - peaks are labelled by the number of excited vibrons of the D- and S-mode. The inset shows the same, except that $\hbar\omega_S \to \infty$. (b) shows a bias trace for $y_{\mathrm{tip}} = y_{\mathrm{np/max}}$ which corresponds to the red/blue curve. The inset shows the centroid of the spectra in (a) as a function of the tip position. The differential conductance in (a) and (b) is normalized to the maximum value in the displayed parameter range. The chemical potential μ_0 is such that we are in the situation depicted in Fig. 4.2. The electron-vibron coupling constant is $\lambda_o = 0.75$, the bias drop parameter is chosen as $c = 1$, and the temperature is $T = 2.1\mathrm{K}$. The largest tip rate is 10^{-4} times smaller than the largest substrate rate. As zero-point fluctuations, we chose $\Delta x_{0D} = 0.17\text{Å}$ and $\Delta x_{0S} = 0.54\text{Å}$ with a distance between the atoms of $a = 1.339\text{Å}$.

much stronger than the van der Waals force. However, the precise strength of the van der Waals force which keeps the molecule on the insulating layer, is not known. Moreover, the insulating layer can also be an ionic compound, as for example NaCl. In this case, electrostatic forces are also responsible for the adsorption of the molecule. Therefore, the ratio 10:1 is just an arbitrary choice. Also the absolute values of the vibronic energies are just one possible choice in a large interval. Note that the vibronic energies are directly related to the zero-point fluctuations via

$$\Delta x_{0D} = \frac{\hbar}{\sqrt{m\hbar\omega_D}} \quad \text{and} \quad \Delta x_{0S} = \frac{\hbar}{\sqrt{4m\hbar\omega_S}}, \tag{4.6}$$

which is derived in A.1. A detailed analysis of the influence of different vibronic energies and thus zero-point fluctuations on the $\mathrm{d}I/\mathrm{d}V$- structure is given in Sec. 5.4.

In the experiments [2], briefly introduced in Sec. 2.3, single excitation lines could

not be resolved because of coupling to phonons in the insulating film [29, 30]. This substrate-induced broadening is not included in our model. Hence, we can resolve single excitation lines if we choose the temperature small enough compared to the vibronic energies, which is the case in Fig. 4.4(a).

The excitation lines are labelled by the number of excited vibrons in the D- and S-mode. As expected, the vibrational ground to ground state transition line is very pronounced in a region around $y_{\mathrm{tip}} = y_{\mathrm{max}}$. The reason for this is that this transition is allowed by Chen's derivative rule because the symmetries between the tip and the molecule match. Furthermore, the electron-vibron coupling of $\lambda_o = 0.75$ prefers ground to ground state transitions, i.e. we are not in the FC blockade regime. Whereas the ground to first excited S-mode transition is not appearing at all for $y_{\mathrm{tip}} = y_{\mathrm{max}}$, higher D-mode excitation lines are visible. The absence of the first S-mode excitation is explained by selection rule 3.89. Higher odd S-mode excitations are too weak to be visible.

When the tip is positioned above the center of the molecule ($y_{\mathrm{tip}} = y_{\mathrm{np}}$) the ground to ground state transition line vanishes and the ground to first excited transition line regarding the S-mode appears. This is explained by selection rule 3.86 and it means, that even though symmetries between tip and molecule do not match, tunneling is allowed but only if a vibron in the S-mode is excited. Thus, vibron-assisted tunneling is clearly visible in Fig. 4.4(a). For larger bias, the D-mode gives just weaker replica of the transition lines which can all be assigned to $m_S = 1$. Hence, it is obvious that the vibron-assisted tunneling effect comes exclusively from the S-mode. This can also be seen in the inset of Fig. 4.4(a), where the S-mode excitations are turned off by taking the limit $\hbar\omega_S \to \infty$.

The differential conductance for $y_{\mathrm{tip}} = y_{\mathrm{np}}$ (red curve) and $y_{\mathrm{tip}} = y_{\mathrm{max}}$ (blue curve) is depicted in Fig. 4.4(b). The parameters are the same as in Fig. 4.4(a). By comparing the two curves, one can see that the peaks of the red curve are shifted to larger bias about a distance of $\hbar\omega_S$. This makes sense because there must be an excitation of a vibron in the S-mode in order to get a non-vanishing rate for the situation where symmetries do not match. Furthermore, the height of the peaks of the red curve is smaller, which is discussed in detail in Sec. 5.4. Since Fig. 4.4(b) shows only bias traces from Fig. 4.4(a), Fig. 4.4(b) gives no new information. Nevertheless, small features are better visible in a $\mathrm{d}I/\mathrm{d}V$ versus V_b plot. For example, there is a small shoulder at $V_b = 0$, which comes from a thermally excited state and which is not visible in Fig. 4.4(a).

One of the experimental results discussed in Sec. 2.3 was the centroid of the $\mathrm{d}I/\mathrm{d}V$-curves for different positions of the tip along the long axis of the molecule. Our theoretical pendant is depicted in the inset in Fig. 4.4(b). As in the experiments, there is a maximum in the center and it decreases towards larger $|y_{\mathrm{tip}}|$.

The next example we analyze is similar to the situation in Fig. 4.4, but this time the electron-vibron coupling is reduced to $\lambda_o = 0.25$. In this case, only the ground to ground state transition regarding the D-mode is visible. Hence, it is appropriate to choose a reduced bias range, which is done in Fig. 4.5(a). Again the vibron-assisted tunneling

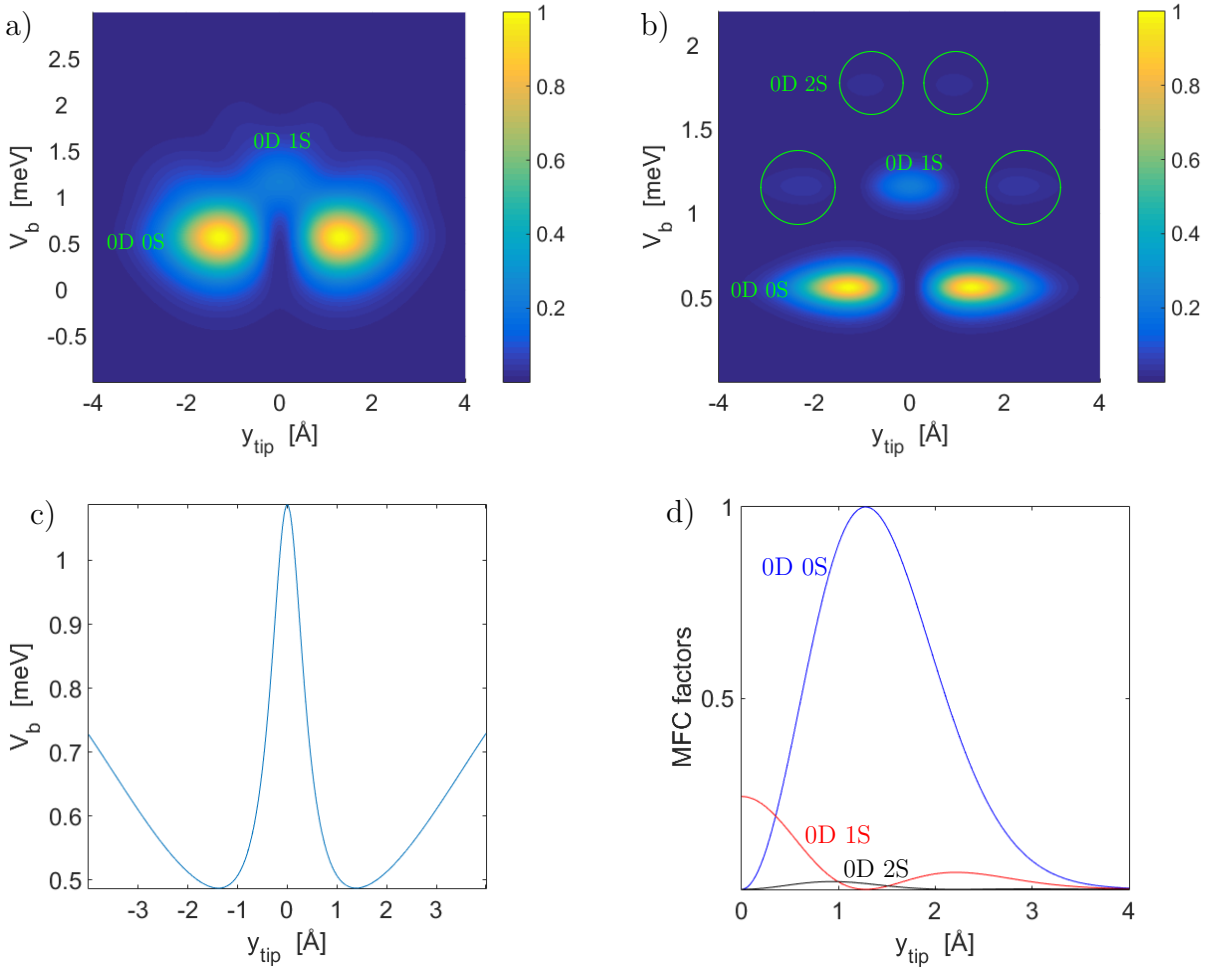

Figure 4.5: (a),(b) show the differential conductance as a function of y_{tip} and V_b. The parameters are the same as in Fig. 4.4(a), except for the electron-vibron coupling and the temperature. For those we chose $\lambda_o = 0.25$, $T = 2.1$K in (a) and $\lambda_o = 0.25$, $T = 0.50$K in (b). Again, the differential conductance is normalized to the maximum value in the displayed parameter range. (c) shows the centroid as function of y_{tip}. (d) shows the square of the MFC factors for the transitions $|m_D = 0, m_S = 0\rangle \rightarrow |m'_D = 0, m'_S = 0, 1, 2\rangle$ as a function of y_{tip}. They are normalized to the maximum of the $|m_D = 0, m_S = 0\rangle \rightarrow |m'_D = 0, m'_S = 0\rangle$ transition. Here, we label the transitions only via the vibronic quantum numbers, because we restrict ourselves to one single electronic transition (see Sec. 4.1). In (a)-(d), y_{tip} runs along the long axis of the molecule. In (d) only one half of the molecule is shown.

effect is clearly visible. For $y_{\mathrm{tip}} = 0$, the ground to ground state transition is vanishing, but a $\mathrm{d}I/\mathrm{d}V$- peak is found at a bias which can be assigned to the excitation of one vibron in the S-mode.

A huge difference to the experimental results and to the inset in Fig. 4.4(b) is found by looking at the centroid of the peak structure of Fig. 4.5(a), which is shown in Fig. 4.5(c). It has again a maximum in the center but it reaches a minimum at $y_{\mathrm{tip}} \approx y_{\mathrm{max}}$ and increases again for larger $|y_{\mathrm{tip}}|$. This can be explained by looking at the $\mathrm{d}I/\mathrm{d}V(y_{\mathrm{tip}}, V_b)$ plot in Fig. 4.5(a) at lower temperature, which is depicted in Fig. 4.5(b). Obviously, the $|m_D = 0, m_S = 0\rangle \rightarrow |m'_D = 0, m'_S = 1\rangle$ excitation line occurs not only at $y_{\mathrm{tip}} = 0$, but also for tip positions beyond the maximum of the molecular wave function. These excitation lines are marked by the large green circles. Moreover, the excitation lines that can be assigned to the state $|m_D = 0, m_S = 2\rangle$ (marked by the small green circles) appear. These additional lines lead to an increase of the centroid for $y_{\mathrm{tip}} > y_{\mathrm{max}}$.

As explained in the beginning of Sec. 4.2, we are in the particular parameter regime where we are probing the MFC factors by measuring the current. Therefore, the origin of these additional lines should be found in the MFC factors. Indeed, this is confirmed by Fig. 4.5(d), where the MFC factors which are responsible for the transition lines are plotted as a function of the tip position. As expected, the MFC factor corresponding to the vibronic ground to ground state transition (blue curve) is zero at the center and has a maximum at $y_{\mathrm{tip}} = y_{\mathrm{max}}$. The MFC factor for the transition into a state with one vibron in the S-mode (red curve) has a maximum in the center (which yields the vibron-assisted tunneling effect) and decreases towards $y_{\mathrm{tip}} = y_{\mathrm{max}}$. For $y_{\mathrm{tip}} > y_{\mathrm{max}}$ it increases again, which leads to the increase of the centroid.

Fig. 4.6(a) and (b) show constant height differential conductance maps at bias voltages which correspond to the transitions $|m_D = 0, m_S = 0\rangle \rightarrow |m'_D = 0, m'_S = 0\rangle$ and $|m_D = 0, m_S = 0\rangle \rightarrow |m'_D = 0, m'_S = 1\rangle$, respectively. As expected, at the bias voltage which corresponds to the onset of the elastic tunneling one is simply scanning the probability distribution of the molecular orbital $|\Psi_{\mathrm{mol}}(\mathbf{r}_{\mathrm{tip}})|^2$. By increasing the bias up to the inelastic tunneling peak, the entire constant height map changes. A maximum in the differential conductance is found at the position of the nodal plane and additional side maxima are appearing. Without these side maxima, the image would resemble the constant height image obtained with a p-symmetric tip at the bias which corresponds to the elastic tunneling. In the experimental results presented in [2], changing the bias from the elastic to the inelastic transition is similar to exchanging the p- with an s-symmetric tip. However, in our case the side maxima are clearly appearing and they originate from the MFC factor which corresponds to the transition $|m_D = 0, m_S = 0\rangle \rightarrow |m'_D = 0, m'_S = 1\rangle$ (red curve in Fig. 4.5(d)).

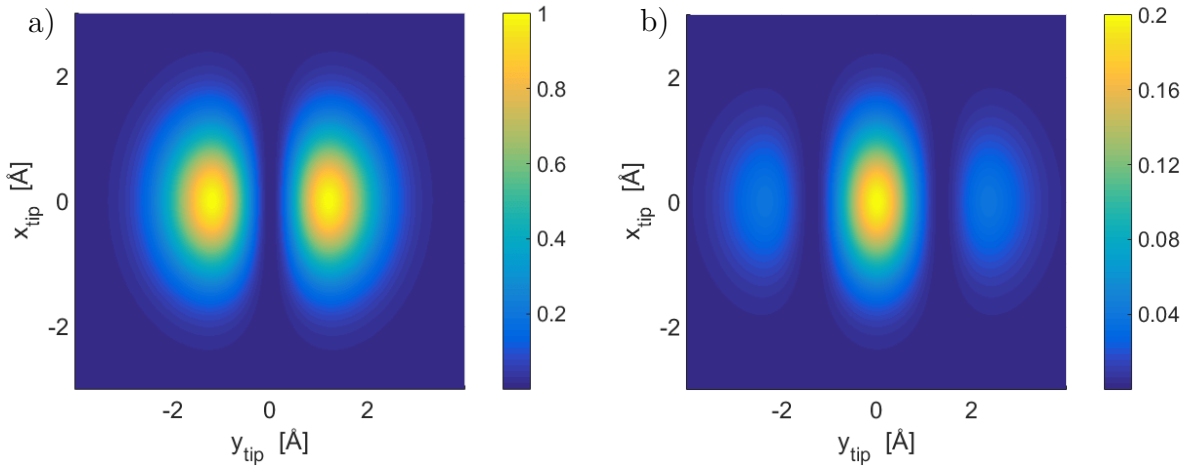

Figure 4.6: Constant height differential conductance images at a bias which corresponds to the onset of the elastic tunneling (a), and a bias which corresponds to the onset of the inelastic transition $|m_D = 0, m_S = 0\rangle \rightarrow |m'_D = 0, m'_S = 1\rangle$ (b). Both figures are given in units of the maximum of the differential conductance in (a). The parameters are as in Fig. 4.4, except for the temperature. It is as small as $T = 0.6$K in order to avoid an overlap of the $\mathrm{d}I/\mathrm{d}V$- peaks.

5

Numerical results obtained for the model with relaxation rate

In Sec. 3.4 a model of a molecule was introduced which consists of one spinless odd molecular orbital and one vibronic mode that moves the nodal plane of the orbital. Additionally, we included a relaxation rate which thermalizes the vibronic distribution of the molecule.

In the first part of this chapter, we verify part of the numerical implementation of this model with data from the literature. After that, we leave the particular situation where the chemical potential is near the CDP. We will see that there is a strong enhancement of the vibron-assisted tunneling effect for certain relaxation rates.

5.1 Verification of the numerical code with results from the literature

In this section, we verify part of our numerical code with numerical results obtained in [28]. The model chosen in [28] is similar to our simplified model introduced in Sec. 3.4, except that a spin-degenerate electronic state and two identical leads without position or deformation dependent tunneling matrix elements are considered. In order to compare the numerical results of the two models, we take two substrate rates (Sec. 3.3.1) for

the leads instead of one substrate and one tip rate. The only difference between the models is then the degeneracy of the electronic state. Therefore, the verification of the program without the implementation of the tip rate is possible, if we take into account the consequences of the spin-degeneracy on the transport.

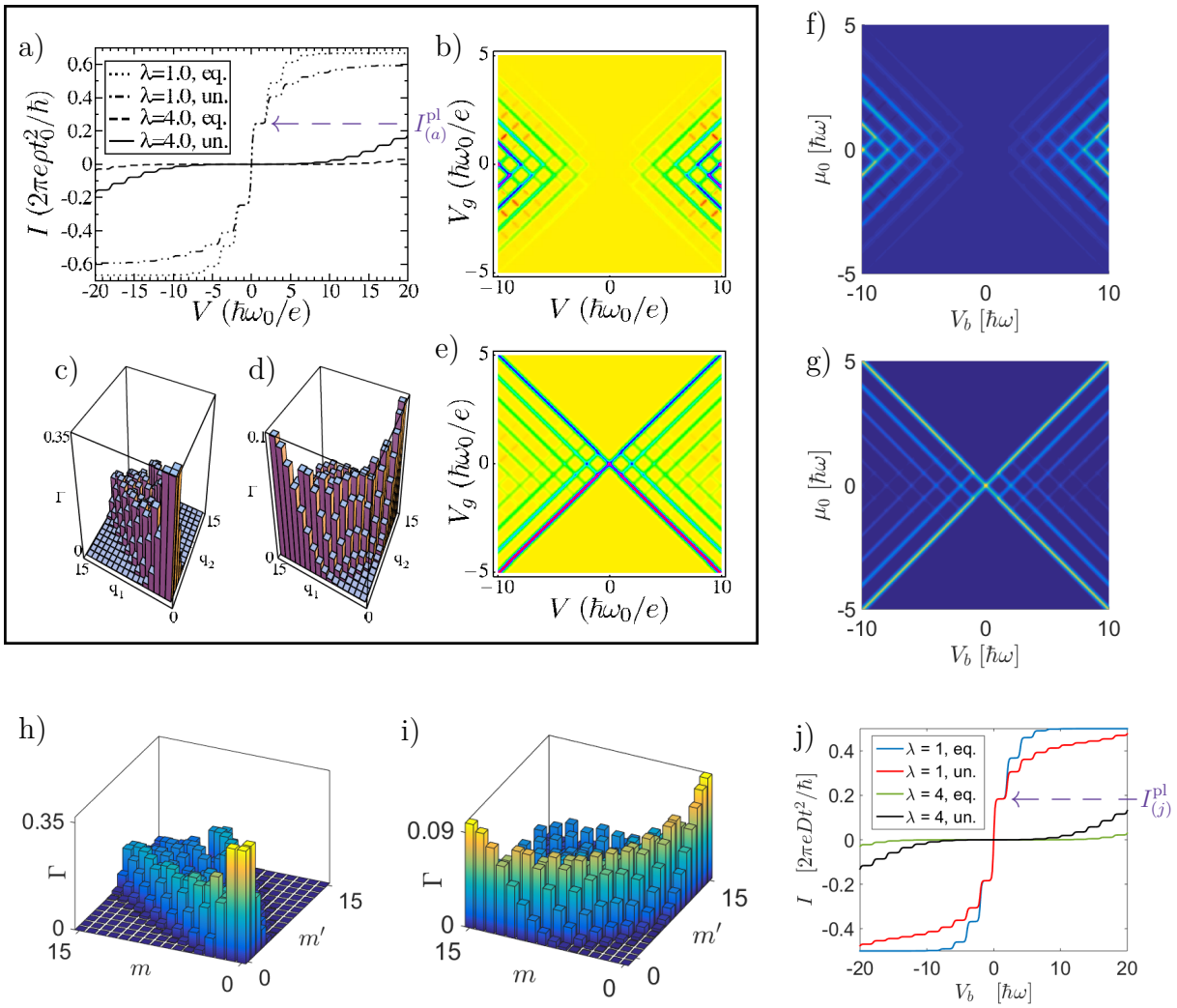

Figure 5.1: (a)-(e) are results taken from [28]. To verify the functionality of our program, we compare these results to our results (f)-(j). For all figures, the parameters are $\epsilon = 0$, $k_BT = 0.05\hbar\omega$ and $c = 0.5$. In (a) and (j), the current is plotted for intermediate and strong electron-vibron coupling and for equilibrated (eq.) and unequilibrated (un.) vibronic distributions. The gate voltage (in our case the zero-bias chemical potential) is set to zero. The rates in (c),(d) and (h),(i) are given in units of $2\pi Dt^2/\hbar$, where D is the density of states and t the tunneling matrix element (denoted by ρ and t_0 in [28]). The vibronic quantum numbers are m and m' in our notation, in (c) and (d) they are denoted by q_1 and q_2. (b),(f) and (e),(g) are stability diagrams for $\lambda = 4$ and $\lambda = 1$.

Fig. 5.1(a)-(e) show the numerical results from [28], which we compare to our results given in Fig. 5.1 (f)-(j). Figs. 5.1(c),(h) and (d),(i) are the rates for intermediate ($\lambda = 1$) and strong ($\lambda = 4$) electron-vibron coupling. Obviously, our rates match perfectly to those from [28].

The rates lead to current-voltage characteristics which are depicted in (a) and (j) for $\tau \to 0$ (equilibrated vibrons) and $\tau \to \infty$ (unequilibrated vibrons). Qualitatively, the results match again. One difference is the magnitude of the current, which is larger in (a). This is due to the spin-degeneracy of the electronic state in (a). To explain the difference between (a) and (j) quantitatively, we concentrate on the height of the current-plateaus $I^{\mathrm{pl}}_{(a)}$ and $I^{\mathrm{pl}}_{(j)}$ (indicated by the purple arrows) for bias voltages in the range $0 < V_b < 2\hbar\omega$. The corresponding free energy diagram is depicted in Fig. 5.2. The populations in Fig. 5.2(b) are simply $P_{n_\uparrow=0,n_\downarrow=0;m=0} = P_{n_\uparrow=1,n_\downarrow=0;m=0} = P_{n_\uparrow=0,n_\downarrow=1;m=0} = \frac{1}{3}$, which leads to a current on the plateau of $I^{\mathrm{pl}}_{(a)} = 2\Gamma P_0 = \frac{2}{3}\Gamma$. In the non-degenerate case (Fig. 5.2(a)), the populations are $P_{n=0;m=0} = P_{n=1;m=0} = \frac{1}{2}$, which leads to a current of $I^{\mathrm{pl}}_{(j)} = \Gamma P_0 = \frac{1}{2}\Gamma$. Therefore, the ratio between the currents is $I^{\mathrm{pl}}_{(j)}/I^{\mathrm{pl}}_{(a)} = \frac{3}{4}$, which is also the ratio between the plateau heights taken from figure (a) and (j) (the numbers are $0.1838/0.245 \approx \frac{3}{4}$). This simple analysis indicates, that the difference between the numerical results comes indeed only from the different degeneracies of the models.

Figs. 5.1(b)(f) and (e)(g) show the stability diagrams for $\lambda = 4$ and $\lambda = 1$, respectively. The gate voltage V_g in Figs. 5.1 (b) and (e) is equivalent to the zero-bias chemical potential μ_0 in Figs. 5.1 (f) and (g). For strong electron-vibron coupling, the FC blockade is clearly visible. Figs. 5.1 (f) and (g) are symmetric with respect to the bias-axis for $\mu_0 = 0$, whereas in Figs. 5.1 (b) and (e) there is an asymmetry. This asymmetry is due to the degeneracy of the electronic state.

Summarizing, we can say that we were able to verify the functionality of our program (without the position dependent tunneling matrix element) with results from the literature.

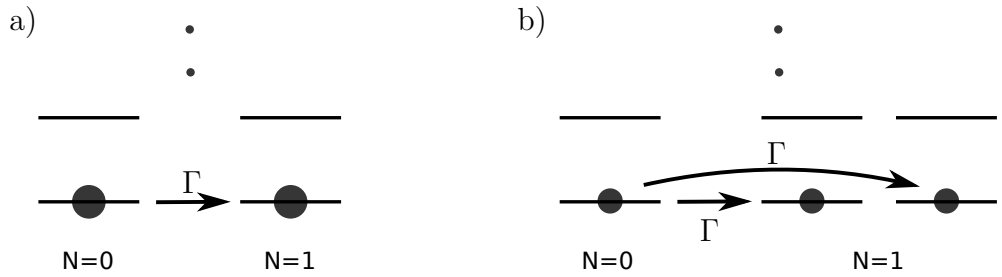

Figure 5.2: The free energy diagram at the CDP for low temperatures ($k_B T \ll \hbar\omega$) and bias voltages in the range $0 < V_b < 2\hbar\omega$ is shown for a degenerate (b) and a non-degenerate (a) electronic level. The filled circles visualize populations P and the arrows indicate the rates Γ from one of the leads to the system.

5.2 Shifted inelastic peaks

The aim of this section is to study the influence of huge differences in the magnitude of the rates on the $\mathrm{d}I/\mathrm{d}V_b$ - peak structure. We consider the model with two substrates as leads (as in the previous section) and the rates are denoted by Γ_{sub1} and Γ_{sub2}. The bias drop occurs entirely between substrate 2 and the molecule ($c = 1$) and the relaxation processes are turned off ($\frac{1}{\tau} \to 0$). We choose an electron-vibron coupling of $\lambda = 1$.

Figs. 5.3(a)-(c) show the $\mathrm{d}I/\mathrm{d}V_b$ - curves for three different ratios of $\Gamma_{\mathrm{sub2}}/\Gamma_{\mathrm{sub1}}$. For the ratio 10^{-5}, the positions of the inelastic peaks are at multiples of the vibronic energy. At these positions, the resonant conditions $n\hbar\omega - V_b - \mu_0 = 0$ with $n \in \mathbb{N}$ are fulfilled. For $\Gamma_{\mathrm{sub2}}/\Gamma_{\mathrm{sub1}} = 1$, the height of the inelastic peaks are smaller, and the peak positions are slightly shifted to larger bias. This slight shift becomes huge in the case of $\Gamma_{\mathrm{sub2}}/\Gamma_{\mathrm{sub1}} = 10^5$. Some of the inelastic peaks are shifted away from resonance by more than $\Delta V_b = \hbar\omega$.

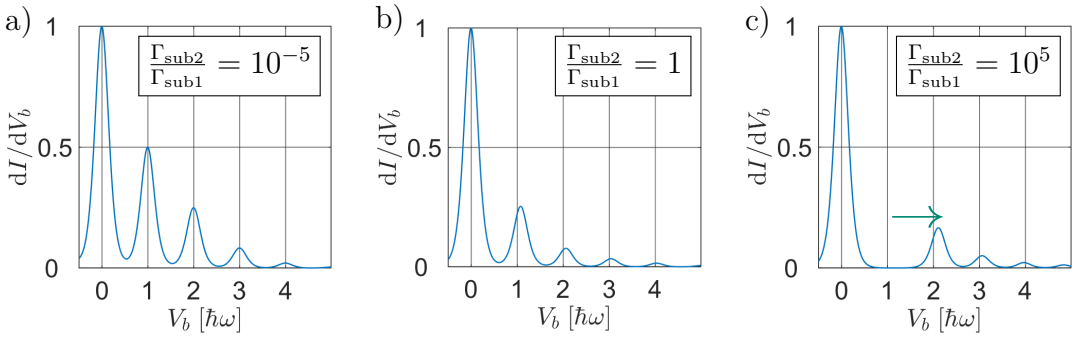

Figure 5.3: (a)-(c) show the differential conductance as a function of the bias voltage (given in units of $\hbar\omega$) for varying rate ratios and $k_BT = 0.1\hbar\omega$. Each graph is normalized to the maximum of its elastic peak. The onsite energy and the zero-bias chemical potential are set to zero.

The explanation for the shift is found by considering the differential conductance in terms of the Liouvillean and the populations of the stationary solution. According to Eq. 3.71, the differential conductance is given by

$$\frac{\mathrm{d}I}{\mathrm{d}V_b}\langle \hat{I}^{\mathrm{in}}_{\mathrm{tip}} \rangle = \sum_{\beta\beta'} N^{\beta}_{\mathrm{mol}} \left[\frac{\mathrm{d}\mathcal{L}^{\mathrm{tip}}_{\beta\beta'}}{\mathrm{d}V_b} P^{\mathrm{stat}}_{\beta'} + \mathcal{L}^{\mathrm{tip}}_{\beta\beta'} \frac{\mathrm{d}P^{\mathrm{stat}}_{\beta'}}{\mathrm{d}V_b} \right]. \tag{5.1}$$

Each entry of $\mathcal{L}$ consists of a sum of rates times the corresponding Fermi functions. Since the rates are independent of the bias, the terms $\mathrm{d}\mathcal{L}^{\mathrm{tip}}_{\beta\beta'}/\mathrm{d}V_b$ are given by a sum of derivatives of Fermi functions which are weighted by the rates. Therefore, the maxima of $\mathrm{d}\mathcal{L}^{\mathrm{tip}}_{\beta\beta'}/\mathrm{d}V_b$ are found at biases which fulfill the resonance conditions if the temperature

is not too large (the individual peaks should be recognizable). The term that shifts the peaks is $\mathrm{d}P^{\mathrm{stat}}_{\beta'}/\mathrm{d}V_b$. The populations of the stationary solution $\vec{P}^{\mathrm{stat}}$ are determined by $\mathcal{L}\vec{P} = 0$ and thus bias dependent. Their dependence on the Fermi functions can be very complicated, leading to maxima at biases which do not fulfill the resonance condition if $T > 0\mathrm{K}$. This is supported by Fig. 5.4, which shows the bias shift of the first inelastic peak ΔV_b as a function of $\Gamma_{\mathrm{sub2}}/\Gamma_{\mathrm{sub1}}$ for different thermal energies. The shift for large temperatures (blue curve) is huge, whereas the shift for small temperatures (green curve) is almost not visible. Particularly interesting is the fact that even for rate ratios equal to 1, there is a shift of the inelastic peak. Only in the limit $\Gamma_{\mathrm{sub2}}/\Gamma_{\mathrm{sub1}} \to 0$ or $T \to 0$ the position of the inelastic peak is exactly at the bias voltage which fulfills the resonance conditions.

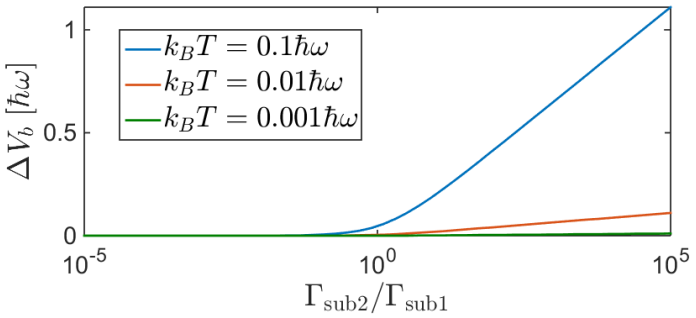

Figure 5.4: The bias shift ΔV_b of the first inelastic peak is shown as a function of the lead rate ratios $\Gamma_{\mathrm{sub2}}/\Gamma_{\mathrm{sub1}}$ for different temperatures. The horizontal axis is given in a logarithmic scale.

However, this effect can probably not be observed in STM experiments. The reason for this is that the bias drop occurs mainly between tip and molecule, which makes it difficult to observe substrate transition lines in the stability diagram. In the situation described above, all the peaks stem from transitions that correspond to the substrate 2. Thus, the limit $\Gamma_{\mathrm{sub2}}/\Gamma_{\mathrm{sub1}} \to 0$, where the effect is not visible, corresponds to the situation in STM.

5.3 Effect of the relaxation rate

In this section we study the effect of the relaxation rate on the transport characteristics. Unlike to the section before, one of the rates is now position and deformation dependent (Eq. 3.98). We choose the parameters such that a double bond between two carbon atoms (appearing for example in ethylene) is modelled. The values are $a = 1.34\text{Å}$ and $Z_{\mathrm{eff}} = 2.9629$ [31].

Moreover, we consider a zero-point fluctuation of $\Delta x_0 = \frac{a}{10}$, weak electron-vibron coupling ($\lambda = 10^{-3}$) and a tip-molecule distance of $z_{\mathrm{tip}} = 4\text{Å}$. We choose a rate ratio of $\Gamma^{\mathrm{max}}_{\mathrm{tip}}/\Gamma^{\mathrm{max}}_{\mathrm{sub}} = 10^{-5}$ and a totally asymmetric bias drop ($c = 1$). $\Gamma^{\mathrm{max}}_{\mathrm{tip}}$ is the largest

tip-molecule rate for $y_{\text{tip}} = y_{\max}$. $\Gamma_{\text{sub}}^{\max}$ is the largest substrate-molecule rate. In the last chapter, the zero-bias chemical potential μ_0 was always in the direct vicinity of the CDP. Now, we leave this particularly simple situation and choose $\mu_0 = -20\hbar\omega$. We emphasize that any other chemical potential, except for $|\mu_0| < \hbar\omega$, gives similar results, at least for small electron-vibron coupling. This is the case, because the substrate evokes the transition $m = 1 \to m' = 0$ with small but large enough probability (compared to the tip rate) to depopulate the excited states. However, the results do not change for arbitrary $|\mu_0| > \hbar\omega$ because all probabilities for the transitions $m \to m' = m - n$ with $n > 1$ are already much to small to contribute.

First, we consider the case with strong relaxation ($\tau \to 0$). This means that for low temperatures ($k_B T \ll \hbar\omega$) only the vibrational ground state is occupied, which is equivalent to the situation near the CDP where the substrate depopulates the excited states. Note that here the choice of μ_0 is completely arbitrary. As in Sec. 4.2, we are effectively probing the MFC factors by measuring the differential conductance. The peak structures for $\tau \to 0$ are shown in Fig. 5.5(a), where the blue curve corresponds to the tip position $y_{\text{tip}} = y_{\max}$ and the red curve to $y_{\text{tip}} = y_{\text{np}}$. Because of $\mu_0 = -20\hbar\omega$ and $c = 1$, the first peak is found at the bias $V_b = 20$ (in units of $\hbar\omega$) and can be assigned to the elastic transition. As expected, the inelastic contribution, which occurs due to vibron-assisted tunneling, is found at $V_b = 21$ for $y_{\text{tip}} = y_{\text{np}}$. The reason for the small height of the inelastic peak is the small MFC factor (Sec. 3.3.2).

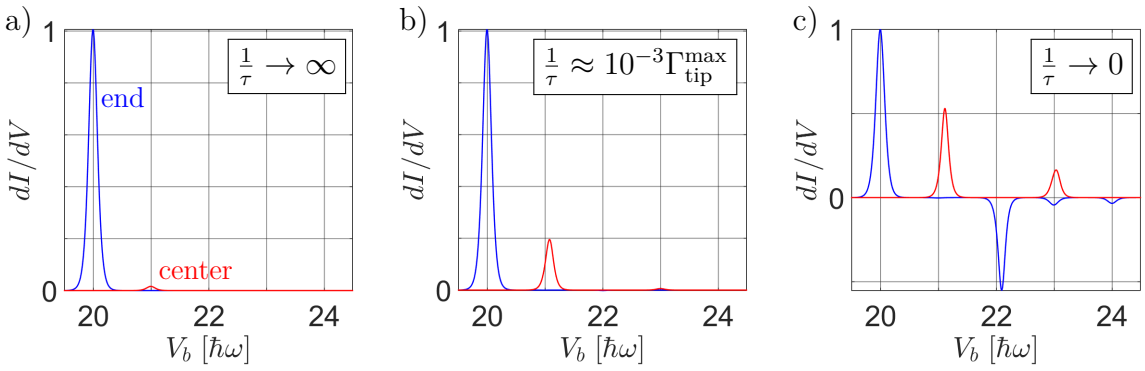

Figure 5.5: (a),(b) and (c) show the differential conductance for different relaxation rates for $k_B T = 0.05\hbar\omega$. They are normalized to the maximum value in (c).

Next, we consider the case without any relaxation processes, shown in Fig. 5.5(c). We already considered this situation with the model with two modes and two electronic orbitals (Ch. 4) but we did not leave the vicinity of the CDP. The most striking features are probably the strong enhancement of the inelastic peak for $y_{\text{tip}} = y_{\text{np}}$, which is on top shifted to larger energy, and the appearance of negative differential conductance (NDC)

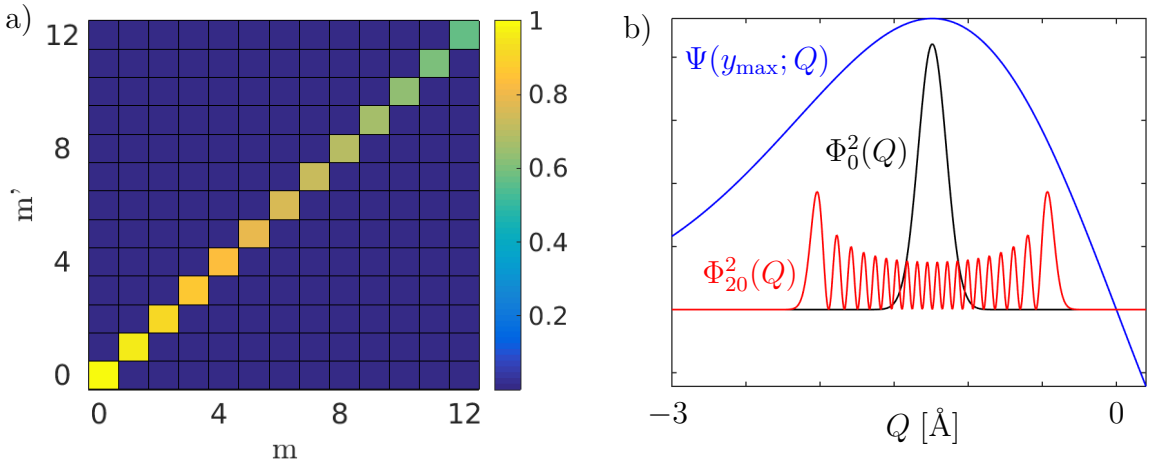

Figure 5.6: (a) shows the MFC factors for $y_{\text{tip}} = y_{\max}$ and parameters specified in the beginning of this section. They are given in units of the MFC factor which corresponds to the elastic transition. (b) visualizes the integrands from Eq. 5.2 for $m = m' = 0$ and $m = m' = 20$. For visualization purposes, the harmonic oscillator functions and the orbital wave function have different scales.

for $y_{\text{tip}} = y_{\max}$. To explain the latter qualitatively, we consider the corresponding MFC factors, which are proportional to

$$\left(\int_{-\infty}^{\infty} \mathrm{d}Q \; \Phi_m(Q) \Psi(y_{\max}; Q) \Phi_{m'}(Q) \right)^2 \tag{5.2}$$

and depicted in Fig. 5.6(a). The MFC parabola is almost diagonal and decreases with increasing $m = m'$. The latter is explained by considering Fig. 5.6(b). The elastic transition amplitude, determined by $\int \mathrm{d}Q \; \Phi_0^2(Q) \Psi(y_{\max}; Q)$, is larger than the amplitude for the transition $m = 20 \rightarrow m' = 20$, which corresponds to the integral $\int \mathrm{d}Q \; \Phi_{20}^2(Q) \Psi(y_{\max}; Q)$. The reason is that higher harmonic oscillator states extend more in space ($\propto \sqrt{m}$) and thus pick up parts of the orbital wave function which are smaller. NDC occurs because vibrationally excited states are populated and thus conducting channels which carry less current (because of the smaller rates) come into play [32]. Nevertheless, in the experiment which shows vibron-assisted tunneling [2], NDC is not observed. Thus, in reality there should be a finite relaxation time which prevents NDC.

This leads us to the case $\frac{1}{\tau} \approx 10^{-3} \Gamma_{\text{tip}}^{\max}$, which is depicted in Fig. 5.5(b). NDC is not occuring any more but the inelastic peak is still strongly enhanced and shifted to larger bias. The explanation for that is given in the next part.

Explanation of the enhancement of vibron-assisted tunneling

The experiments published in [2] suggest that the height of the inelastic peak occurring due to vibron-assisted tunneling is on the same order than the elastic one. However, for realistic zero-point fluctuations ($\frac{a}{100} < \Delta x_0 < \frac{a}{10}$) [27], the MFC factor for the inelastic peak for $y_{\mathrm{tip}} = y_{\mathrm{np}}$ is at least two orders of magnitude smaller than the MFC factor for the elastic peak for $y_{\mathrm{tip}} = y_{\mathrm{max}}$. This is discussed in detail in the next Section. Thus, the corresponding peak heights differ by at least two orders of magnitude for $\frac{1}{\tau} \to \infty$ (Fig. 5.5(a)). However, there can be a strong enhancement of the inelastic peak for certain relaxation rates (the enhancement factor in Fig. 5.5(b) is about 20). The explanation for the strong enhancement is shown in Fig. 5.7. Fig. 5.7 (a) shows the MFC factors for $y_{\mathrm{tip}} = y_{\mathrm{np}}$, which have an off-diagonal structure because of symmetry reasons (Sec. 3.3.2). As expected, the MFC factor for $m = 0, m' = 1$ is around 0.01, i.e. two orders of magnitude smaller than the elastic peak in Fig. 5.6(a). However, for larger m and $m' = m + 1$ the MFC factors increase strongly, which is visualized with an example in Fig. 5.7(b). It shows the integrands of Eq. 5.2 for $m = 0, m' = 1$ and $m = 19, m' = 20$. The harmonic oscillator functions for larger quantum numbers (e.g. $m = 19, m' = 20$) extend further in space than for small quantum numbers (e.g. $m = 0, m' = 1$). Hence, the integral 5.2 picks up larger values of the orbital wave function $\Psi(y_{\mathrm{np}}; Q)$ for larger m and $m' = m + 1$, which leads to increased MFC factors. Their contribution to the transport is visualized by the free energy diagram in Fig. 5.7(c). At the bias $V_b = \hbar\omega - \mu_0$, the tip-molecule transition $(0; 0) \to (1; 1)$ opens. Here, the first entry in the parenthesis is the number of electrons, and the second entry is the number of vibronic excitations. Because of the small electron-vibron coupling, the substrate induces the transition $(1; 1) \to (0; 1)$ with large probability. For small temperatures, the substrate cannot depopulate this state. Thus, for small relaxation rates, the population $P_{(0;1)}$ has a finite value, which can be seen in Fig. 5.7(d). Consequently, the transition $(0; 1) \to (1; 2)$ also contributes to the transport (still at $V_b = \hbar\omega - \mu_0$). This time, the substrate induces the transition $(1; 2) \to (0; 2)$, which leads to an increased population $P_{(0;2)}$. This process continues and opens channels between larger and larger vibronic quantum numbers. The key point is, that the rates that correspond to these channels increase with increasing m and $m' = m+1$ (because of the larger MFCs), leading to the strong enhancement of the vibron-assisted tunneling effect. In Fig. 5.7(c), the increasing rates are visualized by the increasing thickness of the arrows that correspond to the tip transitions. All these arguments are strongly supported by Fig. 5.7(d), which shows that many excited states contribute to the first inelastic $\mathrm{d}I/\mathrm{d}V$-peak. Note that the populations of the state $N = 1$ are six orders of magnitude smaller than the populations for $N = 0$ because of the huge substrate rate. Thus, they are negligible.

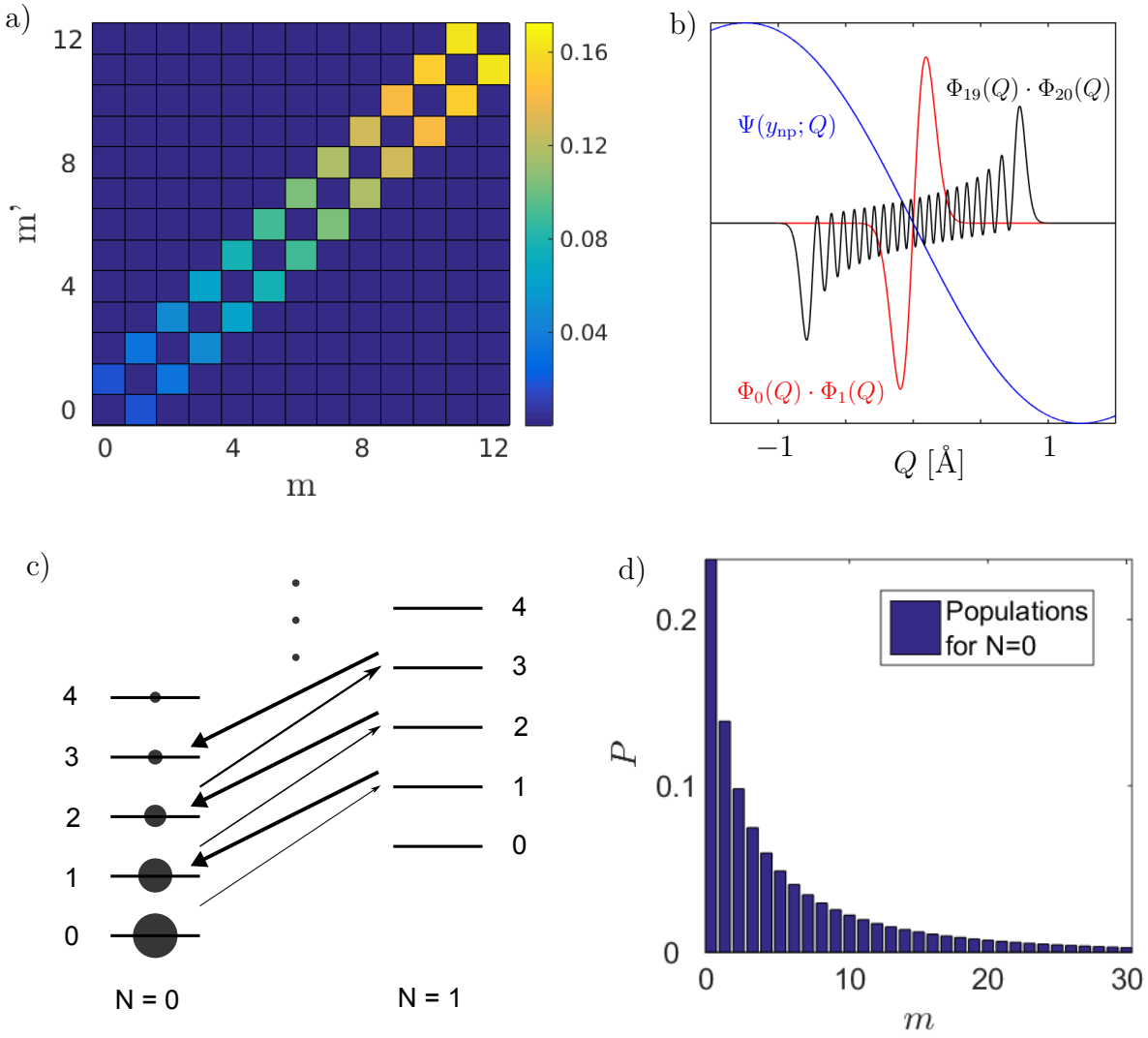

Figure 5.7: (a) shows the MFC factors for $y_{\rm tip} = y_{\rm np}$. They are given in units of the MFC factor which corresponds to the elastic transition for $y_{\rm tip} = y_{\rm max}$. (b) shows multiplied harmonic oscillator functions ($\Phi_0 \cdot \Phi_1$ and $\Phi_{19} \cdot \Phi_{20}$) and the orbital wave function with different scales. (c) is a free energy diagram where the important tip/substrate rates are indicated with thin/thick arrows (here, all substrate rates point from $N = 1$ to $N = 0$, all tip rates from $N = 0$ to $N = 1$). The populations are indicated with filled circles. For visualization purposes, the zero-bias chemical potential is in the interval $-\hbar\omega < \mu_0 < -2\hbar\omega$. (d) shows the populations for $y_{\rm tip} = y_{\rm np}$, $\frac{1}{\tau} \approx 10^{-3}\Gamma_{\rm tip}^{\rm max}$, and $V_b = 1.5\hbar\omega - \mu_0$ for the first 30 vibronic states. Obviously, in the enhancement regime of the vibron-assisted tunneling effect, a large number of vibrons have to be taken into account.

Within our results, the enhancement effect depends on the ratio between relaxation rate and tip rate, which can be seen in Fig. 5.8(a). For larger ratios the populations are redistributed towards lower vibronic excitations and thus the contribution of channels with smaller rates increases. Consequently, the peak heights decrease. However, experiments indicate that the strength of the vibron-assisted tunneling effect is independent from the tip rate within a certain range [33]. More precisely, changing the tip rate by one order of magnitude should not change the form of the peak structure. This experimental observation does not match to our numerical results.

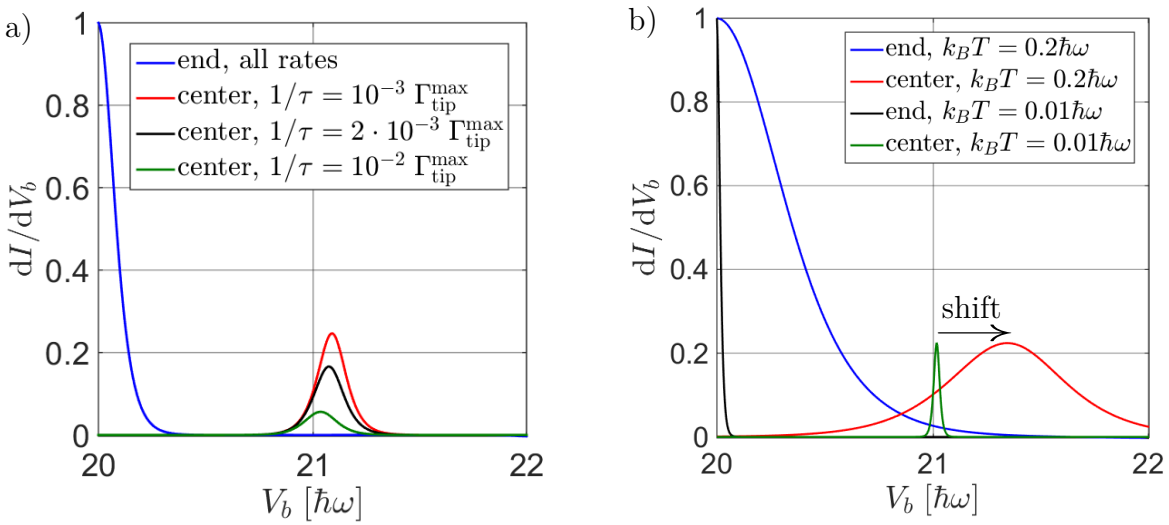

Figure 5.8: (a) The differential conductance as a function of bias voltage is shown for different relaxation rates and fixed tip rates. It is normalized to the elastic peak height for tip positions above the end of the molecule. This peak height is independent of the relaxation rate, thus only one curve (blue) is depicted for $y_{\mathrm{tip}} = y_{\mathrm{max}}$. (b) The differential conductance for different temperatures is depicted. Normalization is as in (a). The shift of the inelastic peak for $y_{\mathrm{tip}} = y_{\mathrm{np}}$ for $k_BT = 0.2\hbar\omega$ is indicated with an arrow. Without the shift, the inelastic peak position would be at $V_b = 21$.

As a last point, we want to address the shift of the inelastic peak in the enhancement regime. Fig. 5.8(b) shows that the magnitude of the shift is temperature dependent. For small temperatures there is almost no shift, whereas for large temperatures the shift to larger bias is clearly visible. This means that it is not possible to directly read of the vibronic energies from the positions of the peaks. The temperature behaviour is similar to the shifted inelastic peaks we have seen in Sec. 5.2. Nevertheless, the origin of the shift is still subject to further investigations.

5.4 Size of the vibron-assisted tunneling effect

In the last section we have seen a strong enhancement of vibron-assisted tunneling for certain relaxation rates. This enhancement happens because highly excited states connected via large MFC factors contribute to the transport. As mentioned several times in the course of this thesis, another effective way of changing the strength of the vibron-assisted tunneling is to change the zero-point fluctuation.

In the experiments showing the vibron-assisted tunneling effect [2], it is not possible to assign certain modes to the peaks in the $\mathrm{d}I/\mathrm{d}V$-spectra nor to extract the relaxation rate. Thus, we analyze the peak structures as a function of the the zero-point fluctuation and the relaxation rate. To be more precise, the aim is to study the peak ratio R between the inelastic $\mathrm{d}I/\mathrm{d}V$-peak at $y_{\mathrm{tip}} = y_{\mathrm{np}}$ and the elastic $\mathrm{d}I/\mathrm{d}V$-peak at $y_{\mathrm{tip}} = y_{\mathrm{max}}$.

Fig. 5.9(a) visualizes R. The blue and the red curve depict the differential conductance for $y_{\mathrm{tip}} = y_{\mathrm{max}}$ and $y_{\mathrm{tip}} = y_{\mathrm{np}}$, respectively. The peak of the blue curve can be assigned to the elastic tunneling contribution $|m = 0\rangle \rightarrow |m' = 0\rangle$ and its peak height is labeled by $C^{00}_{y_{\mathrm{max}}}$. The peak of the red curve corresponds to the inelastic transition $|m = 0\rangle \rightarrow |m' = 1\rangle$, hence its height is labeled by $C^{01}_{y_{\mathrm{np}}}$. The peak ratio R defined as $R \equiv C^{01}_{y_{\mathrm{np}}}/C^{00}_{y_{\mathrm{max}}}$ measures the relative size of the inelastic to the elastic peak and therefore quantifies the strength of the vibron-assisted tunneling effect.

Fig. 5.9(b) depicts R as a function of Δx_0 and the ratio between the tip and the relaxation rate $\Gamma^{\mathrm{max}}_{\mathrm{tip}} \cdot \tau$. The zero-point fluctuation is given in the range $\frac{a}{100} \leq \Delta x_0 \leq \frac{a}{10}$. As expected, R grows for increasing Δx_0 and $\Gamma^{\mathrm{max}}_{\mathrm{tip}} \cdot \tau$. The reason for this is that the relative size of the MFC factors are directly influenced by Δx_0, which is discussed at the end of this section. $\Gamma^{\mathrm{max}}_{\mathrm{tip}} \cdot \tau$ does not influence the relative size of the MFC factors, but affects the enhancement effect we introduced in the previous section. For larger $\Gamma^{\mathrm{max}}_{\mathrm{tip}} \cdot \tau$, the populations of highly excited states increase, leading to a larger height of the inelastic peak. If $\Gamma^{\mathrm{max}}_{\mathrm{tip}} \cdot \tau$ gets too large, NDC is occurring, which is indicated by the white region in Fig. 5.9(b).

As mentioned in the previous section, experiments indicate that the strength of the vibron-assisted tunneling effect is independent from the tip rate. However, in our model, R obviously depends on the tip rate. Yet, for small enough $\Gamma^{\mathrm{max}}_{\mathrm{tip}} \cdot \tau$, effectively only the ground state is populated and a change in $\Gamma^{\mathrm{max}}_{\mathrm{tip}} \cdot \tau$ even by a factor of ten cannot be observed in the differential conductance. In that case, we are close to the limit $\frac{1}{\tau} \rightarrow \infty$ and the enhancement effect vanishes. R is then just the ratio of the MFC factors which can be assigned to the elastic peak (for $y_{\mathrm{tip}} = y_{\mathrm{max}}$) and the inelastic peak (for $y_{\mathrm{tip}} = y_{\mathrm{np}}$). The explanation for that is the same as in Sec. 4.2, only there the depopulation of the excited states is due to the substrate instead of relaxation processes.

The question we want to answer is if it is possible to increase R significantly without

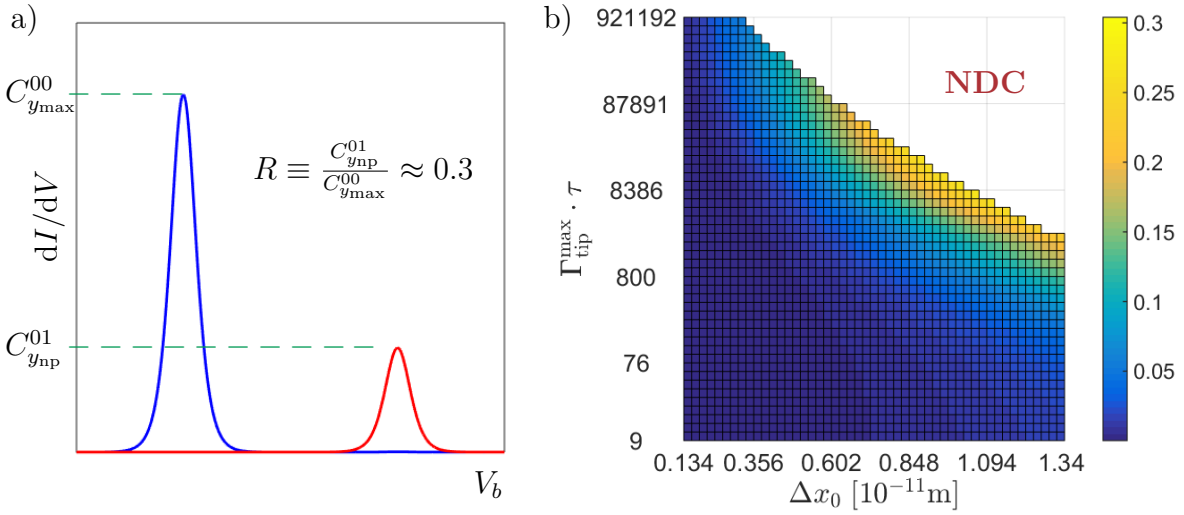

Figure 5.9: The purpose of (a) is to visualize the peak ratio R. The differential conductance is shown as a function of bias voltage for $y_{\rm tip} = y_{\max}$ (blue curve) and $y_{\rm tip} = y_{\rm np}$ (red curve). In the parameter range chosen here, the vibron-assisted tunneling effect leads to a height of the inelastic peak which is about one third of the elastic one. (b) shows R as a function of $\Gamma^{\max}_{\rm tip} \cdot \tau$ and Δx_0. $\Gamma^{\max}_{\rm tip} \cdot \tau$ is the ratio between the maximal tip rate (for $y_{\rm tip} = y_{\max}$) and the relaxation rate. For $\Gamma^{\max}_{\rm tip} \cdot \tau$, we have chosen a logarithmic scale. NDC occurs in the white region (cf. Fig. 5.5(c)).

the enhancement effect (i.e. without the contribution of highly excited states). Thus, we consider the parameters that have a direct influence on the MFC factors. These parameters are Δx_0, $Z_{\rm eff}$, a and $z_{\rm tip}$. Figs. 5.10(a)-(d) show R in the limit $\frac{1}{\tau} \to \infty$ as a function of one of these parameters, where the other three are fixed with default values given in the caption.

The effective atomic number $Z_{\rm eff}$ and the distance between the nuclei a change the form of the molecular orbital, which enters into the MFC via Eq. 5.2. According to Fig. 5.10(b) and (c), a small a and a large $Z_{\rm eff}$ lead to an increased R. Nevertheless, the effect is very limited, i.e. it is not possible to change R by orders of magnitude for realistic $Z_{\rm eff}$ and a. The reason for the small impact of a and $Z_{\rm eff}$ on R is the following: A large $Z_{\rm eff}$ decreases the height of the elastic peak because the orbital wave function decays faster. However, a large $Z_{\rm eff}$ also decreases the steepness of the orbital at the nodal plane, which leads to a decreased MFC factor for the inelastic peak. A small a decreases the amplitude of the orbital at $y_{\rm tip} = y_{\max}$, which decreases the height of the elastic peak. However, a small a also leads to a decreased steepness of the nodal plane (at least for the default value of $z_{\rm tip} = 4$Å we are considering) and thus to a small height of the inelastic peak. Hence, for each parameter there are two effects which partially cancel, which leads to the

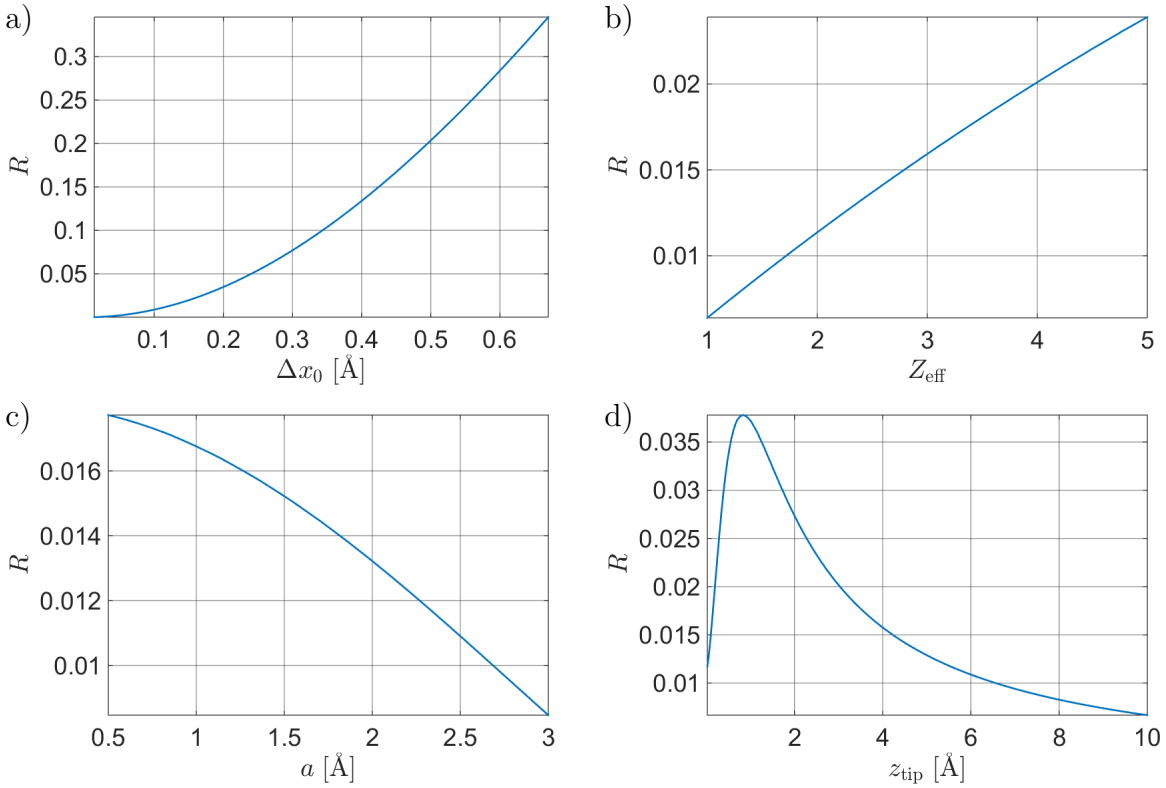

Figure 5.10: Ratio of the first inelastic MFC for $y_{\text{tip}} = y_{\text{np}}$ to the elastic one for $y_{\text{tip}} = y_{\max}$. In the limit $\frac{1}{\tau} \to \infty$ (which we consider here) this ratio equals R. The default parameters are: $a = 1.34$Å, $\Delta x_0 = 0.134$, $Z_{\text{eff}} = 2.9629$ and $z_{\text{tip}} = 4$Å.

net result seen in Fig. 5.10(b) and (c).

R as a function of z_{tip} is depicted in (d). It has a maximum at $z_{\text{tip}} = 0.83$Å with $R = 0.038$. Hence, it seems also not capable of increasing R by orders of magnitude.

The influence of Δx_0 on R is depicted in (a), where the range of Δx_0 is $\frac{a}{100}$ to $\frac{a}{2}$. Obviously, R strongly depends on Δx_0. From $\Delta x_0 = \frac{a}{100}$ to $\Delta x_0 = \frac{a}{2}$ it changes by a factor of $2 \cdot 10^3$. $R > 0.1$ is reached for $\Delta x_0 > 0.34$Å, which is around $\frac{a}{4}$. We can conclude that for large zero-point fluctuations, R can be on the order of 1 without the enhancement effect. Considering Eq. 5.2 together with Fig. 5.6(b) and 5.7(b) clarifies the strong dependence of R on Δx_0. Δx_0 is responsible for the spatial extension of the harmonic oscillator functions and thus determines the contributions of the orbital wave function to the integral 5.2. For example, let us consider a large Δx_0: For $y_{\text{tip}} = y_{\text{np}}$ ($y_{\text{tip}} = y_{\max}$) the contribution of the parts of the orbital with large (small) amplitude is increased. Thus the relative size of the first inelastic MFC factor at the center is increased compared to the elastic MFC factor at the end.

Fixing three of the parameters in $R(\Delta x_0, Z_{\text{eff}}, a, z_{\text{tip}})$ and plotting R as a function of

the remaining one is convenient for visualization purposes. However, in order to find the global maximum in a certain parameter range, we have to consider the entire function at once. The intervals we choose are $\Delta x_0 = [0.67\text{Å}, 0.0134\text{Å}]$, $Z_{\text{eff}} = [1, 5]$, $a = [0.5\text{Å}, 3\text{Å}]$ and $z_{\text{tip}} = [2\text{Å}, 8\text{Å}]$. As expected by the tendencies depicted in Fig. 5.10, the maximum of R lies at $\Delta x_0 = 0.67\text{Å}$, $Z_{\text{eff}} = 5$, $a = 0.5\text{Å}$ and $z_{\text{tip}} = 2\text{Å}$. With these values we get $R = 0.96$, i.e. the peak heights are almost identical.

Summarizing, we can say that in our model there are two ways to receive peak ratios comparable to the experiments [2]. One is to choose a zero-point fluctuation which is on the order of the atomic bond length, the other is to choose a ratio between the relaxation and tip rate such that highly excited vibronic states contribute. Both ways seem to match the classical intuitive picture where the amplitude of the vibration is large enough to move the orbital lobe under the tip. However, a zero-point fluctuation of an inherent vibrational mode of a molecule that is on the order of the atomic bond length seems rather unrealistic. Moreover, the contribution of highly excited vibrational states imply that the $\mathrm{d}I/\mathrm{d}V_b$ - peak structure depends on the tip rate, which is not supported by experimental observations [33].

6

Summary and Outlook

In this thesis, we analyzed the effect of a vibrational degree of freedom in the probed molecule on the transport characteristics of STM with an additional thin insulating layer between molecule and substrate. We described the quantum transport in this system with the Liouville equation approach and developed a minimal model that allows to perform spatially resolved vibronic spectroscopy calculations that reflect tip-molecule symmetry matching. We observed vibron-assisted tunneling for vibronic modes that shift the positions of the nodal planes of the molecule. In our model, the strength of the vibron-assisted tunneling is mainly determined by the zero-point fluctuation of the vibronic mode, and the ratio between the tip-molecule and relaxation rate. The former determines the size of the vibration per vibron, whereas the latter is responsible for the number of vibrons in one mode. In both cases, the classical intuitive picture seems to be correct. The size of the deformation of the molecule due to the vibration has to be large enough to move the orbital lobe near the position of the nodal plane. The apex of the tip has to "see" the orbital lobe in order to get a strength of vibron-assisted tunneling which is comparable to the experiment.

Nevertheless, open questions still remain. Experiments indicate that the strength of the vibron-assisted tunneling seen in [2] cannot be explained by highly excited vibronic states [33]. Thus, an unrealistically large zero-point fluctuation would be necessary to match the results quantitatively. This discrepancy is subject to further investigations.

There are several possibilities to extend our model. In the derivation of the rate equations, we applied the secular approximation, i.e. we neglected all the coherences of the reduced density matrix. These coherences could be included at the price of highly increasing computational costs. Moreover, one could go beyond the second order in the perturbative expansion in the tunneling Hamiltonian by including charge fluctuations at the substrate, which is done by the so-called *dressed second order* [34]. This would lead to an additional broadening of the excitation lines.

Experiments indicate that Chen's derivative rule should be extended in such a way, that not only one single point at the apex of the tip contributes to the transport, but also points in the vicinity of the apex [2, 33]. However, first calculations imply that this extension does not change the strength of the vibron-assisted tunneling. Nonetheless, it could explain the lack of spatial resolution for an s-symmetric tip.

Interesting results could also be obtained by studying certain quantities that are not available in the experiments, as for example the average vibronic energy in the molecule. Moreover, we did not treat the combination of a vibronic mode which moves the nodal plane and intermediate (or even strong) electron-vibron coupling to that mode. Nevertheless, preliminary calculations did not appear to improve the agreement between theory and experiment.

Finally, our minimal model could be generalized to realistic molecules with many different modes which extend in all three spatial dimensions.

A

Appendix

A.1 Size of the zero-point fluctuations

The kinetic part T and the potential part V of the system specified in Fig. 3.1 are given by

$$T = \frac{1}{2}m(\dot{q}_L^2 + \dot{q}_R^2) \quad \text{and} \quad V = \frac{1}{2}k_2(q_L^2 + q_R^2) + \frac{1}{2}k_1(q_R - q_L)^2. \tag{A.1}$$

A transformation into the center of mass and relative coordinates, given by $R = (q_L + q_R)/2$ and $r = q_R - q_L$, yields

$$T = \frac{1}{2}m_S\dot{R}^2 + \frac{1}{2}m_D\dot{r}^2 \quad \text{and} \quad V = \frac{1}{2}k_S R^2 + \frac{1}{2}k_D r^2, \tag{A.2}$$

where $m_D \equiv m/2$ is the reduced mass, $m_S \equiv 2m$, $k_D \equiv \frac{k_2}{2} + k_1$ and $k_S \equiv 2k_2$. The motion of the center of mass and of the relative coordinate are separated. Hence, Eq. A.2 describes two independent harmonic oscillators and we can directly read of the frequency for the center of mass coordinate $w_S = \sqrt{k_S/m_S} = \sqrt{k_2/m}$, and for the relative coordinate $w_D = \sqrt{k_D/m_D} = \sqrt{(2k_1 + k_2)/m}$. Eq. A.2 also allows to construct the

separated Schrödinger equations

$$\begin{aligned}\left[-\frac{\hbar^2}{2m_S}\frac{\partial^2}{\partial R^2}+\frac{1}{2}k_S R^2\right]\Psi(R)=E_S\Psi(R)\\ \left[-\frac{\hbar^2}{2m_D}\frac{\partial^2}{\partial r^2}+\frac{1}{2}k_D r^2\right]\Phi(r)=E_D\Phi(r).\end{aligned} \tag{A.3}$$

The usual quantization of the harmonic oscillator coordinate [35] yields the zero-point fluctuations $\Delta x_{0D}=\sqrt{\hbar/2m_D w_D}=\sqrt{\hbar/m\omega_D}$ and $\Delta x_{0S}=\sqrt{\hbar/2m_S\omega_S}=\sqrt{\hbar/4m\omega_S}$.

A.2 Factorization of the density operator

In this section, we present the proof of Eq. 3.54.
We assume that the molecule is totally decoupled from the lead at some time t_0. Then, one can factorize the density operator into a molecular and a lead part, which gives

$$\hat{\rho}(t_0)=\hat{\rho}_{mol}(t_0)\otimes\hat{\rho}_{res}. \tag{A.4}$$

The time evolution operator in the interaction picture is given by

$$\hat{U}^I(t,t_0)=T_{\leftarrow}\exp\left[-\frac{i}{\hbar}\int_{t_0}^{t}\mathrm{d}\tau\hat{H}_T^I(\tau)\right]=1-\frac{i}{\hbar}\int_{t_0}^{t}\mathrm{d}\tau\hat{H}_T^I(\tau)+\mathcal{O}((\hat{H}_T)^2), \tag{A.5}$$

where $T_{\leftarrow}$ is the time ordering operator. We perform the time evolution of Eq. A.4, which yields

$$\begin{aligned}\hat{\rho}^I(t)&=\hat{U}^I(t,t_0)\hat{\rho}_{mol}(t_0)\otimes\hat{\rho}_{res}(\hat{U}^I(t,t_0))^\dagger\\ &=\hat{\rho}_{mol}(t_0)\otimes\hat{\rho}_{res}-\frac{i}{\hbar}\int_{t_0}^{t}\mathrm{d}\tau\left[\hat{H}_T^I(\tau),\hat{\rho}_{mol}(t_0)\otimes\hat{\rho}_{res}\right]+\mathcal{O}((\hat{H}_T)^2).\end{aligned} \tag{A.6}$$

By taking the trace over the reservoirs and performing the tensor product with $\hat{\rho}_{res}$, one obtains

$$\hat{\rho}_{red}^I(t)\otimes\hat{\rho}_{res}=\hat{\rho}_{mol}(t_0)\otimes\hat{\rho}_{res}+\mathcal{O}((\hat{H}_T)^2). \tag{A.7}$$

We have used that $\mathrm{Tr}(\hat{\rho}_{res})=1$ and that $\hat{\rho}_{res}$ conserves the number of electrons in the reservoir which is not the case for $\hat{H}_T$. Equations A.6 and A.7 finally yield the desired result

$$\hat{\rho}^I(t)=\hat{\rho}_{red}^I(t)\otimes\hat{\rho}_{res}+\mathcal{O}(\hat{H}_T). \tag{A.8}$$

A.3 The Franck Condon factors

In this part, an analytical expression for the Franck Condon factors, given by

$$F(m,m',\lambda) \equiv \left|\langle m|e^{-\lambda(\hat{a}^\dagger-\hat{a})}|m'\rangle\right|^2 \tag{A.9}$$

is derived. Here, $\hat{a}$ is the annihilation operator of an harmonic oscillator. Using the Baker–Campbell–Hausdorff formula, one can rewrite Eq. A.9 into

$$F(m,m',\lambda) = \left|e^{\frac{-\lambda^2}{2}}\langle m|e^{-\lambda\hat{a}^\dagger}e^{\lambda\hat{a}}|m'\rangle\right|^2. \tag{A.10}$$

Expanding the exponentials, one gets

$$e^{\lambda\hat{a}}|m'\rangle = \sum_{l=0}^{\infty}\frac{\lambda^l}{l!}\hat{a}^l|m'\rangle = \sum_{l=0}^{m'}\frac{\lambda^l}{l!}\sqrt{\frac{m'!}{(m'-l!)}}|m'-l\rangle \tag{A.11}$$

and similarly

$$\langle m|e^{-\lambda a^\dagger} = \langle m-k|\sum_{k=0}^{m}\frac{(-\lambda)^k}{k!}\sqrt{\frac{m!}{(m-k)!}}. \tag{A.12}$$

Combining Eqs. A.12 and A.11 yields

$$F(m,m',\lambda) = \left|e^{\frac{-\lambda^2}{2}}\sum_{l=0}^{m'}\sum_{k=0}^{m}\frac{(-\lambda)^k}{k!}\frac{\lambda^l}{l!}\sqrt{\frac{m!}{(m-k)!}}\sqrt{\frac{m'!}{(m'-l!)}}\delta_{m-k,m'-l}\right|^2. \tag{A.13}$$

For the case $m' \geq m$, one can perform the sum over l, which gives

$$\begin{aligned} F(m,m',\lambda) &= \left|e^{\frac{-\lambda^2}{2}}\sum_{k=0}^{m}(-1)^k\frac{\lambda^{2k+m'-m}}{k!(m'-m+k)!}\frac{\sqrt{m!m'!}}{(m-k)!}\right|^2 \\ &= \left|e^{\frac{-\lambda^2}{2}}\sqrt{\frac{m!}{m'!}}\lambda^{m'-m}\sum_{k=0}^{m}(-\lambda^2)^k\frac{m'!}{k!(m'-m+k)!(m-k)!}\right|^2 \\ &= \left|e^{\frac{-\lambda^2}{2}}\sqrt{\frac{m!}{m'!}}\lambda^{m'-m}L_m^{m'-m}(\lambda^2)\right|^2, \end{aligned} \tag{A.14}$$

where $L_m^{m'-m}(\lambda^2)$ are the associated Laguerre polynomials, given by

$$L_m^{m'-m}(\lambda^2) = \sum_{k=0}^{m}(-\lambda^2)^k\frac{m'!}{k!(m'-m+k)!(m-k)!}. \tag{A.15}$$

The case $m' < m$ can be derived similarly by performing the sum over k in Eq. A.13. Combining the two cases, one gets the final result

$$\begin{aligned} F(m,m',\lambda) &= \left| e^{-\frac{1}{2}\lambda^2} [\mathrm{sgn}(m'-m)\lambda]^{|m'-m|} \left(\frac{m!}{m'!}\right)^{\frac{1}{2}\,\mathrm{sgn}(m'-m)} L^{|m'-m|}_{\min(m,m')}(\lambda^2) \right|^2 \\ &= e^{-\lambda^2} \lambda^{2|m'-m|} \left(\frac{m!}{m'!}\right)^{\mathrm{sgn}(m'-m)} \left[L^{|m'-m|}_{\min(m,m')}(\lambda^2)\right]^2 . \end{aligned} \tag{A.16}$$

A.4 The Polaron transformation of the tunnelling matrix element between tip and molecule

In this section, we want to obtain an expression for

$$\tilde{t}_i^{\,\mathrm{tip}}(\hat{Q}_D, \hat{Q}_S) = e^{\hat{S}} t_i^{\mathrm{tip}}(\hat{Q}_D, \hat{Q}_S) e^{-\hat{S}}. \tag{A.17}$$

To this end, we expand the tunnelling matrix element in $\hat{Q}_D$, which yields

$$\begin{aligned} \tilde{t}_i^{\,\mathrm{tip}}(\hat{Q}_D, \hat{Q}_S) =& e^{\hat{S}} \sum_{m=0}^{\infty} t_m(\hat{Q}_S) \hat{Q}_D^m \, e^{-\hat{S}} \\ =& \sum_{m=0}^{\infty} t_m(\hat{Q}_S) (e^{\hat{S}} \hat{Q}_D e^{-\hat{S}})^m. \end{aligned} \tag{A.18}$$

Here, we used the unitarity of the Lang Firsov transformation 3.21 and defined $t_m(\hat{Q}_S)$ as the coefficients of the expansion.
Next, we define the function $\mathrm{g}(\alpha) \equiv e^{\alpha \hat{S}} \hat{Q}_D e^{-\alpha \hat{S}}$ and take the derivative with respect to α. Using the commutation relations of the ladder operators of the harmonic oscillator yields

$$\frac{\mathrm{dg}(\alpha)}{\mathrm{d}\alpha} = -2\Delta x_0 \sum_{\sigma} \left[\lambda_e(\hat{n}_{e\sigma} - 1) + \lambda_o \hat{n}_{o\sigma}\right]. \tag{A.19}$$

Solving the differential equation A.19 with $g(0) = \hat{Q}_D$ gives

$$\mathrm{g}(\alpha) = \hat{Q}_D - 2\Delta x_0 \sum_{\sigma} \left[\lambda_e(\hat{n}_{e\sigma} - 1) + \lambda_o \hat{n}_{o\sigma}\right] \alpha. \tag{A.20}$$

Finally, we insert g(1) into the expansion A.18 and obtain the desired result

$$\begin{aligned}\tilde{t}_i^{\,\mathrm{tip}}(\hat{Q}_D,\hat{Q}_S) &= \sum_{m=0}^{\infty} t_m(\hat{Q}_S)\left\{e^{\hat{S}}\left[\hat{Q}_D - 2\Delta x_0 \sum_\sigma \left[\lambda_e(\hat{n}_{e\sigma}-1)+\lambda_o\hat{n}_{o\sigma}\right]\right]e^{-\hat{S}}\right\}^m \\ &= t_i^{\,\mathrm{tip}}\left(\hat{Q}_D - 2\Delta x_0 \sum_\sigma \left[\lambda_e(\hat{n}_{e\sigma}-1)+\lambda_o\hat{n}_{o\sigma}\right],\hat{Q}_S\right).\end{aligned} \tag{A.21}$$

Bibliography

[1] J. Repp and G. Meyer. "Molecules on Insulating Films: Scanning-Tunneling Microscopy Imaging of Individual Molecular Orbitals". In: *Physical Review Letters* 94 (2005), p. 026803.

[2] N. Pavliček et al. "Symmetry Dependence of Vibration-Assisted Tunneling". In: *Physical Review Letters* 110 (2013), p. 136101.

[3] J. Franck and E. G. Dymond. "Elementary processes of photochemical reactions". In: *Transactions of the Faraday Society* 21 (1926), p. 536.

[4] E. U. Condon. "A Theory of Intensity Distribution in Band Systems". In: *Physical Review* 28 (1926), p. 1182.

[5] E. U. Condon. "Nuclear Motions Associated with Electron Transitions in Diatomic Molecules". In: *Physical Review* 32 (1928), p. 858.

[6] G. Binnig et al. "Tunneling through a controllable vacuum gap". In: *Applied Physics Letters* 40 (1982), p. 178.

[7] D. M. Eigler and E. K. Schweizer. "Positioning Single Atoms with a Scanning Tunnelling Microscope". In: *Nature* 344 (1990), p. 524.

[8] G. Binnig et al. "Tunneling Spectroscopy and Inverse Photoemission: Image and Field States". In: *Physical Review Letters* 55 (1985), p. 991.

[9] C. J. Chen. "Origin of Atomic Resolution on Metal Surfaces in Scanning Tunneling Microscopy". In: *Physical Review Letters* 65 (1990), p. 448.

[10] C. J. Chen. "Tunneling matrix elements in three-dimensional space: The derivative rule and the sum rule". In: *Physical Review B* 42 (1990), p. 8841.

[11] P. Liljeroth, J. Repp, and G. Meyer. "Current-Induced Hydrogen Tautomerization and Conductance Switching of Naphthalocyanine Molecules". In: *Science* 317 (2007), p. 1203.

[12] L. Gross et al. "High-Resolution Molecular Orbital Imaging Using a p-Wave STM Tip". In: *Physical Review Letters* 107 (2011), p. 086101.

[13] K. Blum. *Density Matrix Theory and Application*. Plenum Press, 1996.

[14] S. Sobczyk, A. Donarini, and M. Grifoni. "Theory of STM junctions for π-conjugated molecules on thin insulating films". In: *Physical Review B* 85 (2012), p. 205408.

[15] A. Donarini et al. "Topographical fingerprints of many-body interference in STM junctions on thin insulating films". In: *Physical Review B* 86 (2012), p. 155451.

[16] J. Bardeen. "Tunnelling from a many-particle point of view". In: *Physical Review Letters* 6 (1961), p. 57.

[17] J. Tersoff and D. R. Hamann. "Theory of the scanning tunneling microscope". In: *Physical Review B* 31 (1985), p. 805.

[18] Rainer Härtle. "Vibrationally coupled electron transport through single-molecule junctions". Ph.D. Thesis. Friedrich-Alexander-Universität Erlangen-Nürnberg, 2012.

[19] T. Frederiksen et al. "Inelastic transport theory from first principles: Methodology and application to nanoscale devices". In: *Physical Review B* 75 (2007), p. 205413.

[20] M. Born and R. Oppenheimer. "Zur Quantentheorie der Molekeln". In: *Annalen der Physik* 389 (1927), p. 457.

[21] I. G. Lang and Yu. A. Firsov. "Kinetic theory of semiconductors with low mobility". In: *Soviet Physics Journal of Experimental and Theoretical Physics* 16 (1963), p. 1301.

[22] G. D. Mahan. *Many-Particle Physics*. Plenum Press, 1990.

[23] W. Gerlach and O. Stern. "Der experimentelle Nachweis der Richtungsquantelung im Magnetfeld". In: *Zeitschrift für Physik* 9 (1922), p. 349.

[24] W. Gerlach and O. Stern. "Das magnetische Moment des Silberatoms". In: *Zeitschrift für Physik* 9 (1922), p. 353.

[25] L. Mayrhofer and M. Grifoni. "Linear and nonlinear transport across carbon nanotube quantum dots". In: *The European Physical Journal B* 56 (2007), p. 107.

[26] S. Koller, L. Mayrhofer, and M. Grifoni. "Spin transport across carbon nanotube quantum dots". In: *New Journal of Physics* 9 (2007), p. 348.

[27] Personal communication with Andrea Donarini. Institute of Theoretical Physics, University of Regensburg, Germany.

[28] J. Koch and F. von Oppen. "Franck-Condon Blockade and Giant Fano Factors in Transport through Single Molecules". In: *Physical Review Letters* 94 (2005), p. 206804.

[29] J. Repp et al. “Scanning Tunneling Spectroscopy of Cl Vacancies in NaCl Films: Strong Electron-Phonon Coupling in Double-Barrier Tunneling Junctions”. In: *Physical Review Letters* 95 (2005), p. 225503.

[30] Niko Pavliček. “Scanning Probe Methods Applied to Molecular Electronics”. Ph.D. Thesis. Universität Regensburg, 2013.

[31] E. Clementi and D. L. Raimondi. “Atomic Screening Constants from SCF Functions”. In: *The Journal of Chemical Physics* 38 (1963), p. 2686.

[32] A. Yar et al. “Dynamical symmetry breaking in vibration-assisted transport through nanostructures”. In: *Physical Review B* 84 (2011), p. 115432.

[33] Personal communication with Jascha Repp. Institute of Experimental Physics, University of Regensburg, Germany.

[34] S. Sobczyk, A. Donarini, and M. Grifoni. “Transport across an Anderson quantum dot in the intermediate coupling regime”. In: *European Physical Journal B* 86 (2013), p. 384.

[35] J. J. Sakurai and J. Napolitano. *Modern Quantum Mechanics*. Pearson Education, 1994.

Acknowledgements

At this point I would like to thank the people who supported me during the coarse of this thesis.

First and foremost, I would like to express my deep gratitude to PD Dr. Andrea Donarini for the excellent supervision. He always had time to share his knowledge with me and to answer my questions in great detail and with a lot of patience. He provided a very productive working atmosphere and inspired me with his creative way of solving problems and with his enthusiasm for physics. All the exciting discussions we had provided a steep learning curve, and I believe that I will profit for a long time from the skills I achieved.

Moreover, I would like to give thanks to Prof. Milena Grifoni for inviting me into her wonderful research group and for giving valuable suggestions to my work. All the discussions in the group meetings helped a lot in analyzing and solving the problems that occurred during the coarse of this thesis.

I would also like to acknowledge the help of Benjamin Siegert. In particular, he supported me a lot concerning numerics, the theory of scanning-tunneling microscopy, and IT issues.

I am appreciating the invitation of Prof. Jascha Repp to give a talk in his research group and for his valuable input concerning this thesis.

Furthermore, I would like to thank Dr. Manohar Awasthi for simulating the vibrational modes of Pentacene.

I would like give thanks to my colleagues Michael Niklas, Korbinian Groh, Richard Gottschalk, and Lars Milz for the nice working atmosphere and the numerous exciting discussions we had.

Last but not least, I would like to thank my family for their strong support in every facet of my life.

Erklärung

Ich habe die Arbeit selbständig verfasst, keine anderen als die angegebenen Quellen und Hilfsmittel benutzt und bisher keiner anderen Prüfungsbehörde vorgelegt.

Pentling, 4. Mai 2015

Raphael Kozlovsky